© Copyright by Mark August Pfeifer, 2005

STRUCTURAL STUDIES OF LEAD NANOCRYSTALS USING COHERENT X-RAY DIFFRACTION

BY

MARK AUGUST PFEIFER

B.S., University of Notre Dame, 1998
M.S., University of Illinois at Urbana-Champaign, 2000

DISSERTATION

Submitted in partial fulfillment of the requirements
for the degree of Doctor of Philosophy in Physics
in the Graduate College of the
University of Illinois at Urbana-Champaign, 2005

Urbana, Illinois

Acknowledgments

I would like to thank my advisor, Ian K. Robinson, for his guidance for the past six years. I have learned a great deal from him in discussions, group meetings, attending a course he taught, and particularly in conducting experiments with him.

I would also like to thank fellow researchers at the University of Illinois, particularly Ivan Vartanyants, John Pitney, Sébastien Boutet, Tommy Angelini, Wei Zhang, Yang Da, Meng Liang, and Vasilica Crecea. I would particularly like to thank Garth Williams for innumerable discussions about both theory and experimental aspects of coherent X-ray diffraction.

I would like to thank members of UNICAT at the Advanced Photon Source, particularly Hawoong Hong for use of his vacuum chamber in initial experiments and discussions (and occasional loans of equipment) on our new vacuum chamber. Curt Benson was of great help in his tireless efforts to construct UNICAT's coherent X-ray beamline and assistance in commissioning experiments.

I owe great thanks to my wife Alex, for her support and understanding, especially as I have spent at least half of our wedding anniversaries at synchrotrons. I also thank her for spending so much effort raising our son Patrick while I have spent more time than I would like away from them. I would like to thank both our families for their considerable support.

This research would not have been possible without the financial support of the Department of Energy, Office of Basic Energy Research, and the National Science foundation. Experiments were performed at the Advanced Photon Source at Argonne National Laboratory, a Department of Energy facility. Supplementary measurements were made at the Center for Microanalysis of Materials at the Materials Research Laboratory, a Department of Energy Laboratory.

This research was supported by the NSF under grants DMR98-76610 and

DMR03-08660. The UNICAT facility at the Advanced Photon Source (APS) is supported by the University of Illinois at Urbana-Champaign, Materials Research Laboratory (U.S. DOE contract DEFG02-91ER45439, the State of Illinois-IBHE-HECA, and the NSF), the Oak Ridge National Laboratory (U.S. DOE under contract with UT-Battelle LLC), and the National Institute of Standards and Technology (U.S. Department of Commerce).

Table of Contents

List of Tables

List of Figures

Chapter 1

Introduction

Current technological efforts in material fabrication have focused on nanomaterials, such as Cu reinforced with 25nm diameter alumina fibers[38], microporous catalytic materials with pore sizes between 0.5nm and 50nm, and nanoparticle catalysts[13, 57], including equilibrium crystal shapes[37], which undergo changes of morphology and roughening transitions as their temperature is changed. The performance of all these materials is affected by the detailed structure of their shape and by the exact configuration of their surface. Surface reconstruction or surface induced strain may also affect their behavior.

Of particular interest is the structure of equilibrium crystal shapes. Understanding the temperature dependent morphology and surface structure of an equilibrium shape requires knowledge of the orientation dependence of the surface free energy of the crystal[66], the roughening transition of facets with low index orientations[20, 34], and surface melting[58, 55]. The melting of a surface below the bulk melting point has been presented as an explanation for the fact that a liquid can be supercooled but a solid can almost never be superheated. This is supported by the fact that extended surfaces of a non-surface melting orientation do in fact support overheating[16].

A variety of techniques are available to measure structures of sub-micron sized objects. Transmission electron microscopy produces a projection of the density of a sample with sub-nanometer resolution in the $x - y$ plane. By tilting the sample, different projections are visible, providing some degree of information in the z direction[17, 50]. This technique is limited to thin samples or samples which can be cut or ion milled to a thickness of tens of nanometers[35] without affecting the shape of the structure to be studied. It

is known that the equilibrium shapes taken by clusters of hundreds of atoms is greatly different from the shape obtained in the thermodynamic limit[68].

An alternative method which has been used successfully to study equilibrium crystal shapes is scanning electron microscopy[30]. This technique produces a single view of the surface of the sample. The work function of the surface can be studied with a scanning electron microscope, giving an indication of the beginning of surface melting for different orientations of a crystal[45]. This measurement is not sensitive to the depth of the quasi-liquid layer or its degree of crystallinity.

The technique of coherent X-ray diffraction allows an entire three dimensional structure to be imaged[64]. Because of the penetrating power of hard X-rays, samples with an extent of microns can be imaged. Because the measurement is made in diffraction geometry, it is sensitive to the crystallinity of the sample. This, in principle, will allow measurement of the degree of order of a quasi-liquid film as a function of depth and orientation. More specifically, the diffraction measurement is sensitive to order-disorder in the direction of the scattering vector, meaning that any directional anisotropy in the disorder of the quasi-liquid is, in theory resolvable.

An additional advantage of coherent X-ray diffraction is its sensitivity to the projection of strain onto the scattering vector. Although the sample preparation in Section 4.2.1 was designed to produce unstrained equilibrium shapes, strain is clearly visible in the objects recovered from some diffraction patterns. This strain sensitivity, which can detect a 0.01% shift of the local lattice from a reference ideal lattice, is potentially the greatest advantage of this tecnique.

This thesis is organized as follows. Chapter 2 describes the thermodynamics of equilibrium shapes, including their overall morphology, their melting temperature as a function of particle size, and the phenomenon of surface melting. Chapter 3 provides a summary the principles of coherent X-ray diffraction and the methods to recover the phases associated with measured diffraction patterns and the complex density of the diffracting object. Chapter 4 describes an experiment which measured coherent X-ray diffraction patterns from sub-micron Pb equilibrium crystal shapes at elevated temperatures, and the process for phasing those diffraction patterns. Chapter 5 describes analysis of the density recovered from phasing the patterns measured in Chapter 4, including correction for a geometric distortion

arising from the diffraction geometry, modeling of the recovered density to a thermodynamic model, and interpretation of the phase of the complex-valued density in real space. Chapter 6 provides a review of the results of this research and suggests improvements to the experiment to allow measurement of surface melting. Future directions for coherent X-ray diffraction are also discussed.

Chapter 2

Thermodynamics of Small Crystals

2.1 Equilibrium Shapes

The shape that would be taken by a crystal in equilibrium with its vapor or melt is a general problem that was given a proper formulation by Curie[15] in the late 1800's: given a crystal for which the surface free energy per unit area varies with orientation, what geometric shape minimizes the total surface free energy? Wulff[67] proposed a solution which lead to the Wulff plot, a graphical manner of determining a crystal shape from a free energy plot, also known as a γ plot. The proof that Wulff's solution was in fact a local minimum of the free energy was given by Hilton[33], Liebman[39] and von Laue[60]. It was not until 1953 that Herring[28, 27] proved that Wulff's construction led to an absolute minimum of the free energy for all possible free energy plots. An overview to equilibrium shapes can be found in Wortis[66]. The derivation in Section 2.1.1 is taken largely from the notes of Gert Ehrlich.

2.1.1 Curie Construction of Equilibrium Shapes

The Curie construction describes a particle which is bounded by planes of constant surface tension and in which overhangs are not allowed. Following this formulation, we define the total surface free energy L as

$$L = \sum_i \gamma_i A_i, \tag{2.1}$$

where γ_i is the surface tension, or free energy per unit area, and A_i is the area of the the i'th surface, which may be finite, infinitesimal, or zero in area. Because the equilibrium condition is a minimum of the free energy, we can write

$$dL = \sum \frac{\partial L}{\partial h_i} dh_i = 0, \tag{2.2}$$

where dh_i is the distance to the i'th surface. Because the crystal is equilibrium with its vapor, its volume V must be constant.We may therefore write

$$dV = \sum \frac{\partial V}{\partial h_i} dh_i = 0. \tag{2.3}$$

These conditions must be met simultaneously for a crystal to be in equilibrium. Combining (2.2) and (2.3) using a Legrange multiplier, we can write

$$\sum \left[\frac{\partial L}{\partial h_i} - \lambda \frac{\partial V}{\partial h_i} \right] dh_i = 0. \tag{2.4}$$

Because the differentials dh_i are independent, each term in the sum must be zero for the sum to be zero. Setting $\left[\frac{\partial L}{\partial h_i} - \lambda \frac{\partial V}{\partial h_i} \right]$ for one i and substituting in the definition of L (2.1), we have

$$\sum_k \gamma_k \frac{\partial A_k}{\partial h_i} - \lambda \frac{\partial V}{\partial h_i} = 0. \tag{2.5}$$

Using the solid angle Ω_i of a face of the crystal, the area of that face and its partial derivative can be written as

$$A_i = \Omega_i h_i^2 \tag{2.6}$$

$$\frac{\partial A_i}{\partial h_k} = \delta_{i,k} 2 \Omega_i h_i, \tag{2.7}$$

where the Kronecker-delta function is defined as

$$\delta_{i,k} = \begin{cases} 1 & \text{for} \quad i = j \\ 0 & \text{for} \quad i \neq j. \end{cases} \tag{2.8}$$

Since the area A_i only depends explicitly on the distance to that face, its partial derivatives with respect to distances to other faces is zero.

The volume of the crystal can be written as

$$V = \sum_i \int_0^{h_i} \Omega_i r^2 dr \tag{2.9}$$

$$= \sum_i \frac{1}{3} \Omega_i h_i^3. \tag{2.10}$$

As above, the derivative with respect a particular h_i, is limited to a single term

$$\frac{\partial V}{\partial h_i} = \Omega_i h_i^2 \tag{2.11}$$

Substituting Eqns. (2.7) and (2.11) into Eqn. (2.5)

$$2\gamma_i \Omega_i h_i - \lambda \Omega_i h_i^2 = 0 \tag{2.12}$$

$$\frac{\gamma_i}{h_i} = \frac{\lambda}{2}. \tag{2.13}$$

The distance to a given plane is proportional to the surface tension of that plane, agreeing with the expected result that lower energy planes are closer to the origin of the crystal, and therefore give larger facets. Depending on the form of the surface tension, Ω_i may be finite, infinitesimal, or zero for a given orientation. In the case of an isotropic γ, the distance to each 'face' is identical, leading to the expected result for bubbles and liquid droplets of a spherical shape.

The result in Eqn. 2.13 can expressed graphically by means of the Wulff plot, shown in Fig. 2.1. This plot begins with a radial plot of the surface tension of the crystal. Planes (or lines in the 2D case) are drawn through each point on the surface, perpendicular to the line connecting that point to the center of the crystal. The equilibrium shape, up to a volume scaling factor, is given by the area internal to all the planes. Low energy orientations will have facets, whereas higher energy orientations will only exist in planes that are tangent to the shape at a single point or will be missing entirely from the boundary of the crystal. Orientations that are not found on a crystal should strictly speaking not be included in the free energy plot, because the free energy of those orientations is not a measurable quantity at equilibrium. By convention all orientation are typically plotted for the Wulff plot of a theoretical model. Close packed planes tend to be low energy because the atoms on the surface have the most neighbors and fewest broken bonds.

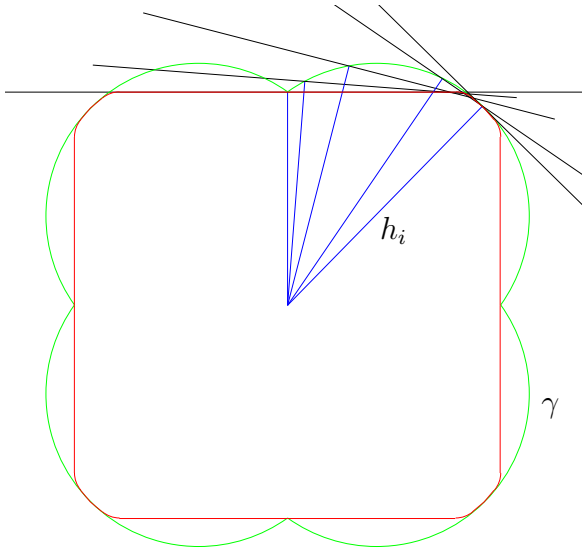

Figure 2.1: Wulff plot of equilibrium crystal shape. The free energy is plotted as a function of orientation in green. Select planes (lines) with given orientation are plotted at a distance from the center proportional to their surface tension. The volume (area) internal to all planes gives the equilibrium crystal shape, in red.

2.1.2 Crystalline Free Energy

If the shape of a crystal is determined by its free energy per unit area as a function of orientation, the next question to ask is; what are the origins of orientation dependence of the free energy, and how does it change with respect to temperature?

The simplest model where the only 'defects' permitted in the ideal infinite crystal are the truncation of the crystal at boundaries plus vacancies and roughened steps on the surface. This ignores internal vacancies, contaminants, and surface reconstructions, where the atoms on the surface (and potentially a few layers below) reorganize to form a lower energy than the surface structure resulting from a simple cleaving of a crystal. The only surface reconstructions observed on Pb is a decomposition of a {110} surface into elements with {111} and {100} orientations[8]. This reconstruction, therefore, is not an aspect of an equilibrium shape, but rather the beginning of roughening of a {110} surface.

The $T = 0$ energy for a facet of a given orientation can be calculated assuming knowledge of the energy of nearest neighbor interactions. Consider

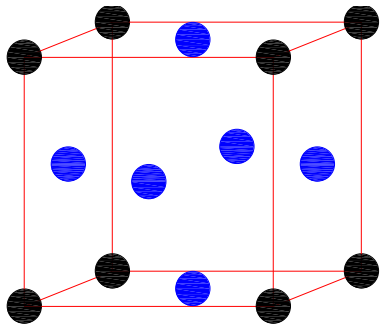

Figure 2.2: Face centered cubic (fcc) lattice

a face centered cubic (fcc) crystal which has a cubic lattice with atoms at the vertices and at the centers of each cube, as shown in Fig. 2.2. Each atom has 12 nearest neighbor bonds, $\mathbf{b} = a/2\{(1\ 1\ 0), (1\ 0\ 1), (1\ \text{-}1\ 0), (1\ 0\ \text{-}1), (\text{-}1\ 1\ 0), (\text{-}1\ 0\ 1), (\text{-}1\ \text{-}1\ 0), (\text{-}1\ 0\ \text{-}1), (0\ 1\ 1), (0\ 1\ \text{-}1), (0\ \text{-}1\ 1), (0\ \text{-}1\ \text{-}1)\}$, where a is the length of a side of the unit cell. The number of bonds of type $\mathbf{b}_i$ broken per unit area of a plane with a normal $\hat{\mathbf{n}}$ cleaving a large crystal is given by the number density of the atoms in the crystal $1/v_a$ times the absolute value of the dot product of the plane's normal and the vector describing the bond. To avoid double counting, only half of the bonds are considered– a set where none can be written as minus one times another vector. The surface tension for this nearest neighbor model can be written as

$$\gamma(\hat{\mathbf{n}}) = J_0 \frac{1}{v_a} \sum_{i=1}^{6} |\hat{\mathbf{n}} \cdot \hat{\mathbf{b}_i}| \tag{2.14}$$

$$= J_0 \frac{4}{a^3} \frac{a}{2} \{|\hat{\mathbf{n}} \cdot (110)| + |\hat{\mathbf{n}} \cdot (101)| + |\hat{\mathbf{n}} \cdot (011)| + \tag{2.15}$$

$$|\hat{\mathbf{n}} \cdot (1\bar{1}0)| + |\hat{\mathbf{n}} \cdot (10\bar{1})| + |\hat{\mathbf{n}} \cdot (01\bar{1})|\} \tag{2.16}$$

where $-J_0$ is the nearest neighbor energy of interaction. In this construction next nearest neighbor interactions can be easily added, using $-J_1$ as the next nearest neighbor interaction and bonds described by $\mathbf{c} = a\{(1\ 0\ 0), (0\ 1\ 0), (0\ 0\ 1)\}$.

$$\gamma(\hat{\mathbf{n}}) = J_0 \frac{1}{v_a} \sum_{i=1}^{6} |\hat{\mathbf{n}} \cdot \hat{\mathbf{b}_i}| + J_1 \frac{1}{v_a} \sum_{i=1}^{3} |\hat{\mathbf{n}} \cdot \hat{\mathbf{c}_i}| \tag{2.17}$$

While the $T = 0$ equilibrium shape follows straightforwardly from the bond energies and geometry of the lattice, higher temperature equilibrium

crystal shapes combine energetic and entropic considerations. It is useful to discuss the roughening temperature T_R for a given orientation. At any finite temperature, a surface will have some fraction of single atoms and islands on the surface in addition to holes exposing the next lower layer. Above the roughening temperature height fluctuations become unbounded for an infinite crystal. It is at T_R that a facet found at a low temperature equilibrium shape disappears[66, 20]. This transition is discontinuous; as the temperature increases, the size of a facet decreases, yet it remains finite up to T_R, at which the local curvature jumps from 0 to some finite value. Another way of defining T_R is that it is the temperature at which the free energy of the formation of a step edge goes to zero.

There are two contributions to entropy of a surface which preserve crystallinity, *i.e.* no atoms are displaced from lattice sites. The first, which applies to all surfaces, is vacancy-adatom formation, in which an atom is thermally excited out of its position in the top layer and is then free to move about the surface. The second is kink formation along step edges, which applies to vicinal directions– those which are near low index directions. The entropy of a low index plane will be higher than the vicinal planes because the energy to form a vacancy ϵ_v is much higher than the kink formation energy ϵ_k. If the energy to break a single bond is ϵ_b, then for a $\{111\}$ surface of an fcc material, $\epsilon_v = 9\epsilon_b - 3\epsilon_b = 6\epsilon_b$; nine bonds are broken removing the atom from the surface layer and three are formed depositing on top of the surface at some other point as seen in Fig. 2.3b. If an atom is removed from a step edge and placed somewhere else along the edge, seven bonds are broken and five new ones are formed, as shown in Fig. 2.3a. Any additional atoms adjacent to the hole in the step edge which are removed from their position and added to the new atom on the edge have no net loss of bonds. In this way four kinks are formed (one up and one down at the site of the new atoms on the edge, one down and one up where the atoms were removed) for a total cost of two bonds, therefore $\epsilon_k = \epsilon_b/2$. If an atom is removed from a step edge and remains free on the surface, its excitation energy is $4\epsilon_b$, higher than if it moves to another position on the step edge, but still less than the energy to excite a flat surface.

To understand the thermodynamics of a thermally excited surface, it is necessary to know both the energy of excitations and their degeneracy. For this purpose we consider the partition function, $Z = \sum_s e^{-\epsilon_s/\tau}$, which

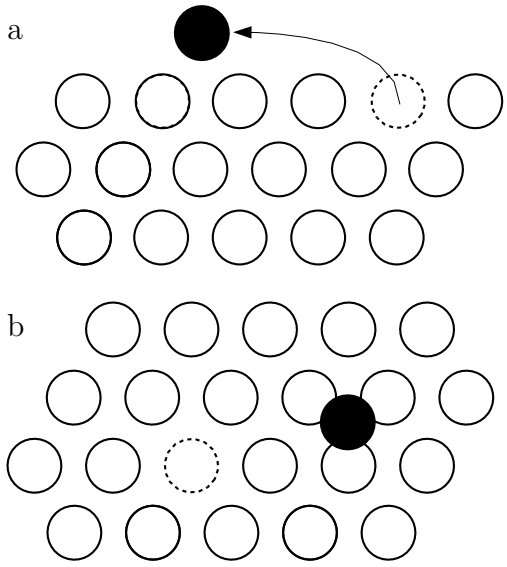

Figure 2.3: a) A step edge on a surface vicinal to {111}. When an atom is moved from the edge site (dashed) to a new position (solid) four in-plane bonds are broken and two new bonds are formed, in addition to the three bonds between the atom and the next layer down. This action creates four kinks. Additional atoms removed from sites adjacent to the vacancy and added to the new edge atom have no net effect on the energy. b) Vacancy (dashed) and adatom (solid) on flat surface. Six in plane bonds are broken and no new ones are formed when and atom is removed from the surface layer and deposited on top, giving a much higher energy than for kink formation.

gives the Helmholtz free energy $F = -\tau \log(Z)$, where $\tau = k_B T$[36]. A single step edge of length N atoms is a simple one dimensional three state system; the ground state (no kink) and two degenerate excited states (plus and minus kinks). Its partition function is therefore the product of the partition functions of each individual potential kink site

$$Z = (e^{-\epsilon_0/\tau} + e^{-(\epsilon_o+\epsilon_k)/\tau} + e^{-(\epsilon_o+\epsilon_k)/\tau})^N \tag{2.18}$$

$$Z = e^{N\epsilon_0/\tau}(1 + 2e^{-\epsilon_k/\tau})^N \tag{2.19}$$

where ϵ_0 is the energy of an atom on a straight step edge, relative to the bulk, which is $7\epsilon_b$ for an fcc surface. The free energy is therefore

$$F = -\tau \log(e^{-N\epsilon_0/\tau}(1 + 2e^{-\epsilon_k/\tau})^N) \tag{2.20}$$

$$= N\epsilon_0 - N\tau \log(1 + 2e^{-\epsilon_k/\tau}). \tag{2.21}$$

F is defined as $F = U - \tau\sigma$, where U is the energy of the system and σ is the entropy. We have the expected result that the energy is the energy per atom times the number of atoms in the straight step edge and the energy of the step edge is also proportional to the length of the edge.

A simplification to the entropy is typically applied in literature, assuming $\epsilon_k \ll \tau$.

$$\sigma = N \log(1 + e^{-\epsilon_k/\tau} + e^{-\epsilon_k/\tau}) \tag{2.22}$$

$$= \log\left(\frac{1}{1 - e^{-\epsilon_k/\tau}} + \frac{e^{-\epsilon_k/\tau} - e^{-2\epsilon_k/\tau}}{1 - e^{-\epsilon_k/\tau}}\right) \tag{2.23}$$

$$= N \log\left(\frac{e^{\epsilon_k/2\tau} + e^{-\epsilon_k/2\tau}}{e^{\epsilon_k/2\tau} - e^{-\epsilon_k/2\tau}}\right) \tag{2.24}$$

$$= N \log(\coth(-\epsilon_k/2\tau)) \tag{2.25}$$

This result has been used to create a theoretical framework to analyze facet radius data from STM as a function of temperature over a wide temperature range[12]. This method takes advantage of the fact that the ratio of the radius, $r(T_1)$, of a facet of an equilibrium shape to the free energy of the step circling that facet $F_s(T)$ is independent of temperature, *i.e* $r(T_1)/F_s(T_1) = r(T_2)/F_s(T_2)$[51]. It should be noted that the roughening temperature of a surface is typically greater than zero and potentially greater than the melting

temperature. The roughening temperature of a step edge, on the other hand, is necessarily zero[51]. This means that at any finite temperature the edges of a facet will be round.

There are a few limitations of this experimental technique. Mainly is the need for low temperature measurements, preferably as low as $0.3T_m$, where T_M is the melting temperature. While it is possible to carry out STM measurements on equilibrium shapes at this temperature, only very small crystals could be measured because of the slow equilibration at this temperature. The low temperature is needed because of the numerous approximations relying on $e^{-\epsilon_k/\tau} \ll 1$ and the iterative process of recovering the $T = 0$ free energy, which starts with $r(0) = r(t_{min})$, the facet radius at the lowest temperature measured. This technique is therefore not capable of determining the entropy of a high temperature equilibrium shape where the surface is highly excited.

2.1.3 Previous Equilibrium Shape Studies

The definitive studies of equilibrium shapes were carried out by Heyraud and Métois in the early 1980's[31, 30, 29]. They chose to study the systems of Au on graphite and Pb on graphite. The substrate was chosen because high quality, clean graphite surface could be obtained by cleavage under vacuum, and because graphite is stable in vacuum well over the melting point of gold. Gold was chosen first on the basis of it chemical passivity. Despite this, great care was taken to perform the entire experiment *in vacuo* with as low a base pressure as possible. Heyraud and Métois critique previous equilibrium shape experiments for using methods which allow the opportunity for contamination of their samples.

Sundquist[56] attempted to measure the anisotropy of the free energy as a function of direction of a range of metals (Au, Ag, Cu, Ni, α-Fe and γ-Fe) on BeO by studying their equilibrium shapes. In these experiments the substrate was cleaned by heating to over 1800°C in 10^{-6} Torr. A sample film was then vapor deposited at room temperature. The sample was then removed from vacuum so that it could be wrapped in a foil of the same metal as was deposited and then placed into a cell where it was annealed in either vacuum of an H_2 environment.

After annealing the sample was removed from the cell and a colloidon film was applied to the sample and then removed. The colloidon film then

had some particles embedded in it and had indentations from others. A thin graphite film was then deposited to trap the embedded particles and to decorate the inside of the holes. A TEM image then shows two sorts of images. The metal particles in the film completely block the beam incident on them, producing a sharp shadow. The graphite-decorated holes give projections of the walls of the holes. This technique produced clear shapes with large facets. Even though equilibration times as long as 100 hours were used, there was considerable variation in the shape of particles from an individual sample, indicating that they were not proper equilibrium shapes. The exact shapes may have been due to contamination or kinetics. Because of the greater chemical activity of rough sites on a surface, atoms in the vapor are more likely to attach to rounded regions, causing them to move outward and expand the area of flat faces.

Winterbottom[65] carried out similar experiments to those of Sundquist, but with the goal of measuring the particle-substrate interface energy. In this case Ag deposition was carried out on BeO in two different systems, one with considerable contamination from pump oil, the other with a pressure of 10^{-9} Torr. The films on the "dirty" samples broke up quickly and produced similar shapes whether annealing time was two days or six days at a temperature of 700°C. The film grown in clean conditions did not break up, even after 160 hours at 800°C.

Pilliar and Nutting[46] used sample preparation similar to Sundquist in experiments to measure the interface energy between a series of metals (Au, Ag, Cu, Ni, and α-Fe) on Al_2O_3. They used two different TEM-based measurements to get a ratio of distance from the origin of a particle to a particle-vacuum interface to the distance from the origin to the particle-substrate interface. By looking in the surface normal direction a few grains which had formed along edge of the substrate could be viewed in a profile giving the desired distances. For particles on the flat surface an indirect method was required. Au-Pd was deposited on the sample at an angle so that each particle produced a shadow with a length which was proportional to the height of that individual particle. A normal incidence SEM then saw the radius of the particle-vacuum interface and could infer the particle-substrate interface because the Au-Pd shadow was visible in the TEM. Using the measured radii and an assumed value for the substrate-vacuum free energy, the substrate-particle and particle-vacuum energies could be calculated. There are two

potential drawbacks of this experiment. First, as with the above experiments, the sample was exposed to air at two stages of the experiment; after the initial deposition and the measurement of particle shape. Secondly, the authors cooled the samples "slowly" so as to avoid deformation of the particle from strain. Unfortunately, if the sample is cooled slowly its shape should evolve as its temperature changes. It is no longer clear at what temperature the particle was equilibrated. Additionally, the vapor in the cell will deposit on surfaces upon cooling, contributing to growth shapes. For these reasons quenched samples, or more ideally samples at their equilibration temperatures, should be measured.

Heyraud and Métois developed a technique to carry out substrate preparation, deposition, and annealing all within a single vacuum system[29, 31, 30]. The substrate is prepared by soldering a single crystal of graphite between two pieces of molybdenum by thermocompression. After insertion in the vacuum system, the graphite is cleaved by application of a shearing force, producing a surface which has not been exposed to atmosphere. 3000Å of high purity Au[29, 31] or Pb[30] is evaporated onto the substrate at room temperature. In the case of Au, a molybdenum cover was placed over the sample while it was annealed at 1000°C, or $T_M - 64$°C. This cover was necessary to maintain the $\sim 5 \times 10^{-6}$ Torr of Au at 1000°C. Molybdenum was used because it is known that Au does not stick to molybdenum at 1000°C. Heyraud and Métois were initially concerned about leakage of Au from their molybdenum chamber since it was not sealed. They found that the size distribution and morphology of their crystals was the same after 5 days as it was after 10 hours, leading them to conclude that leakage was not a problem.

Even at T_m the vapor pressure of Pb is $\sim 1 \times 10^{-9}$ Torr[41], meaning that for practical purposes solid Pb can always be considered to be in equilibrium with its vapor even at UHV conditions. A cover was therefore not needed for the equilibration of Pb with its vapor. After deposition, the Pb samples were melted to break up the films, and then supercooled (high purity Pb will not solidify until it is far below its melting temperature) until they solidified. They were then brought up the their annealing temperatures, which were 200°C, 250°C, 275°C, and 300°C. The melting temperature of Pb is 327°C.

After annealing, their samples were brought to room temperature and removed from the vacuum chamber. The initial cooling rate was approximately 30° C/s for the Au samples. In the case of the Pb samples, the temperature

dropped from 350°C to 120°C in 30 seconds. Because none of the samples were extremely close to melting it can be argued that this was fast enough to freeze in the high temperature shape. Within a few degrees of melting it is likely that the shape could evolve considerably on a time scale of less than a second, so any shape observed after cooling would be some sort of evolution shape.

The samples were then studied in an SEM where surveys were done comparing the diameter of facets, Φ_i to the radius of the particle at the rounded regions, r. By simple geometry this gives the distance from the origin of the crystal to the facet $h_i^2 = r^2 - (\Phi_i/2)^2$, which by Eqn. 2.13 gives the ratio of surface free energies of the rough surface $\bar{\gamma}$ and the facet γ_i. For Au at 1000°C they found a maximum anisotropy of $\bar{\gamma}/\gamma_{(111)} = 1.034$, and an intermediate value for the (100) surface $\gamma_{(100)}/\gamma_{(111)} = 1.019$. Their studies of Pb showed a maximum anisotropy decreasing with increasing temperature from 1.06 at 200°C to 1.035 at 300°C. Even at the highest temperature studied there were cusps in the free energy for both {111} and {100} orientations indicated by finite facets of those orientations. Even at the lowest temperature the crystal shapes were sufficiently rounded that all orientations were present and a continuous surface free energy plot could be determined. Their anisotropy measurements varied by approximately 1% from crystal to crystal.

2.2 Size Dependent Melting

2.2.1 Boundary Effects on Phonon Modes

The Lindemann hypothesis of melting states that a crystalline solid melts when Φ, the ratio of the root mean squared vibrations of atoms in a crystal to the nearest neighbor distance, reaches a certain value (typically 10%), the entire crystal melts. In this model boundary effects and pressure should be analyzed to find how they modify the phonon modes of a crystal.

The vibrational amplitude of ions in a crystal is inversely proportional to the Debye temperature, Θ_D, and the nearest neighbor spacing c,

$$\Phi^2 \propto \frac{T}{(c\Theta_D)^2}. \tag{2.26}$$

Neglecting the mixing of longitudinal and transverse phonon modes from the

surface, Couchman[14] writes the ratio of the melting temperature for finite size crystal T_m to the bulk melting temperature T_m^0, of the same material as

$$\frac{T_m}{T_m^0} = \left(\frac{\Theta_D}{\Theta_D^0}\right)^2 = \left(\frac{1 + \frac{1}{8}\left(\frac{\pi}{6}\right)^{\frac{1}{3}} v^{\frac{1}{3}} \frac{S}{V}}{1 + \frac{1}{4}\left(\frac{\pi}{6}\right)^{\frac{1}{3}} v^{\frac{1}{3}} \frac{S}{V}}\right)^2, \tag{2.27}$$

where v is the volume per atom in the crystal, S is the surface area of the crystal, and V is total volume of the crystal. The superscript zero once again refers to a bulk value.

In the case of and extended rectangular crystallite of thickness t, the surface volume ratio is $S/V \approx 2/t$. The ratio of melting temperatures may then be written as

$$\frac{T_m}{T_m^0} = \left(\frac{1 + \frac{1}{4}\left(\frac{\pi}{6}\right)^{\frac{1}{3}} \frac{v^{\frac{1}{3}}}{V}}{1 + \frac{1}{2}\left(\frac{\pi}{6}\right)^{\frac{1}{3}} \frac{v^{\frac{1}{3}}}{V}}\right)^2. \tag{2.28}$$

Defining b as the spacing between planes of atoms and n as the number of atomic planes in a crystal, the thickness can be written as $t = nb$. If the nearest neighbor distance, c, is written as a fraction of the the plane spacing, $c = b/\alpha$, the atomic packing factor K can be written as $K = \frac{4}{3}\pi\left(\frac{c}{2}\right)^2 \frac{1}{v}$. The ratio of temperatures can be rewritten as

$$\frac{T_m}{T_m^0} = \left(\frac{1 + \frac{1}{4}\left(\frac{\pi}{6}\right)^{\frac{2}{3}} \frac{1}{K^{\frac{1}{3}}\alpha n}}{1 + \frac{1}{4}\left(\frac{\pi}{6}\right)^{\frac{2}{3}} \frac{1}{K^{\frac{1}{3}}\alpha n}}\right)^2. \tag{2.29}$$

For an fcc material Eqn. 2.29 can be rewritten as

$$\frac{T_m}{T_m^0} = \left(\frac{1 + 0.1795/\alpha n}{1 + 0.3590/\alpha n}\right)^2. \tag{2.30}$$

Consider the crystal of Pb, with a bulk melting temperature of 600K, which has its shortest dimension in a {111} direction. The lattice spacing is $a = 4.95\text{Å}$. The nearest neighbor spacing is therefore $c = 4.95\text{Å}/\sqrt{2}$ and the plane spacing is $b = 4.95\text{Å}/\sqrt{3}$. The melting temperature would therefore be suppressed by 1.2° for a 50nm particle, or a 0.15° for a 500nm particle.

2.2.2 Surface Melting

The phenomenon of surface melting refers to a quasi-liquid layer which can exist on a solid surface below the bulk melting point[58]. Atoms in this layer are not bound to any lattice site, but they are still affected by the presence of the nearby lattice, causing some degree of spacial ordering. Surface melting occurs when the free energy of the solid-vapor interface γ_{sv} is greater than the energy of the solid-liquid interface γ_{sl} plus the energy of the liquid vapor interface γ_{lv}, or

$$\gamma_{sv} > \gamma_{sl} + \gamma_{lv}. \tag{2.31}$$

It is therefore useful to define a relative interfacial energy change of forming liquid layer $\Delta\gamma \equiv \gamma_{sv} - \gamma_{sl} - \gamma_{lv}$.

The energy of a the interface between the quasi-liquid and vapor is taken to be a weighted average of the energies of the solid-vapor and liquid-vapor interfaces,

$$\gamma_{lv} = \gamma_{lv} + M(\gamma_{sv} - \gamma_{lv}), \tag{2.32}$$

where M is and order parameter normalized so that $M = 1$ for a perfect crystal and $M = 0$ for a true liquid. In a similar manner we can write the interfacial energy between the solid and the quasi-liquid layer as

$$\gamma_{sq} = (1 - M)\gamma_{sl}. \tag{2.33}$$

Assuming the order parameter decreases exponentially with film thickness l,

$$M = e^{-l/l_0} = e^{-N/N_0}, \tag{2.34}$$

where N is the number of disordered atoms in a region of the quasi-liquid layer and $N_0 = nl_0$ is a constant on the order if 10^{15} atoms/cm^2, and n is the atomic number density. Incorporating the latent heat of melting the crystal, $\mathcal{L}$, to account for the energy contribution from the supercooling of the atoms in the quasi-liquid layer, the energy of the layer can be written as

$$\gamma = \gamma_{sl} + \gamma_{lv} + \mathcal{L}N\left(1 - \frac{T}{T_m}\right) + \Delta\gamma e^{-N/N_0}. \tag{2.35}$$

The number of atoms in the quasi-liquid layer at equilibrium, N_{eq} is found

by minimizing γ with respect to N,

$$N_{eq} = N_0 log\left(\frac{T_m \Delta\gamma}{(T_m - T)\mathcal{L} N_0}\right). \tag{2.36}$$

Consider the case of Pb, where $n = 4/(4.95\text{Å})^3$ and $T_m/\Delta\gamma\mathcal{L} = 1673 \times 10^{18} K/m^2$[58]. To find the temperature at which approximately 10Åwill be melted, $N_{eq} = n \times 10\text{Å} = 3.3 \times 10^{15}\text{cm}^{-2}$. Substituting into Eqn. 2.36, we get $T_m - T = 12\text{K}$. Unfortunately the logarithmic dependence of the number of atoms in the quasi-liquid layer on the temperature relative to the melting temperature means that a 10nm would not occur until the temperature is within 6×10^{-9}K of melting.

The equilibrium shape of a particle partially wetted by a quasi-liquid layer appears to be modified by the presence liquid. This effect was discovered by Heyraud and Métois[32], who observed that the transition from {111} facet to rounded region on the surface of Pb was smooth below $T_m - 20\text{K}$ and sharp above that temperature. This observation was made in conjunction with the observation that above $T_m - 20\text{K}$ the {111} face *grew* with increasing temperature, opposite from the general trend of all facets decreasing at the expense of rounded regions as the temperature is increased.

Noziéres[44] proposed an explanation to the sharpening of the facet-rounded interface calling on the properties of the quasi-liquid layer. Near a low index plane, Noziéres described the surface free energy as

$$E(n) = \gamma_0 + \beta n + \phi n^3 + O(n^4) \tag{2.37}$$

where n is the linear density of steps (along the perpendicular to the step edge. β is then the energy of single step and $\phi(n)$ is the leading term in the interaction between steps. Because the crystallinity penetrates into the quasi-liquid, the energy of a step edge of on a wetted surface is less than the energy of a step edge on a non-wetted surface. This means that the energy of the non-wetted surface as a function of step density, $E_{sv}(n)$ has a greater slope (β) than the energy of the wetted surface, $E_{slv}(n)$. The condition $E_{sv}(0) < E_{slv}(0)$ is necessary for the existence of the non-wetting surface. The curves for $E_{sv}(n)$ and $E_{snv}(n)$ must therefor cross at some value n_m. In the vicinity of n_m the surface energy $E(n)$ given by the minimum of $E_{sv}(n)$ and $E_{snv}(n)$ at each n has downward convexity. A line may then

be drawn through the point $E_{sv}(n)$ and tangent to $E_{snv}(n)$ at the point $E_{snv}(n_c)$. In the range $0 < n < n_c$ the surface is unstable. This range of forbidden orientations produces an edge between the facet (n=0) and the rounded region of the crystal.

The argument of Noziéres depends on the assumption that the crystallinity of a surface varies solely with depth, not within a layer. Stewart[54, 55] argued that step melting melting diminished the effect of surface melting on the free energy curve enough that another explanation was necessary to describe the sharp edge in the facet-rough orientation transition observed by Heyraud and Métois. Assuming that the excess energy of a stepped surface is isolated about the steps, taking the form of an exponential with a decay length of one layer spacing centered about each step, Stewart writes down the position dependent surface free energy as

$$E(x, n, l, T) = E(n = 0, l, T) + \beta \sum_{j=-\infty}^{\infty} \frac{e^{-|(x-ja/|n|)|/l_0}}{2l_0}, \tag{2.38}$$

where a is the step height. The assumption has been made that the step edges are periodic, hence x is periodic with a spacing of $x - a/|n|$.

Minimization of the free energy in Eqn. 2.38 wields a surface which has narrow melting regions a few atoms wide in the vicinity of each step edge. Averaging over a continuous surface, this yields a continuously variable quasi-liquid layer thickness. This should eliminate sharp edge between the {111} facets and the roughened region.

Stewart presents a mechanism to lower the surface energy of flat surfaces to explain the sharp edge and the increasing area of the non-wetted facet near melting. Lone adatoms on the surface or vacancies within the surface should produce a localized melting effect similar to the step edge melting calculated above. Gert Ehrlich[61] has observed a decrease of the diffusion barrier of a Ir atoms on an Ir{111} surface towards a cluster of Ir atoms, resulting in a high probability of the cluster to capture and adatom in its general vicinity. This should yield a much lower density of adatoms on a surface with step edges than on a flat surface. By adding a term proportional to the density of adatoms on a surface to the free energy equation, Stewart[55] calculates a free energy as a function of orientation which once again include a downward convex region, shown in Fig. 2.4, giving rise to a sharp edge in the surface

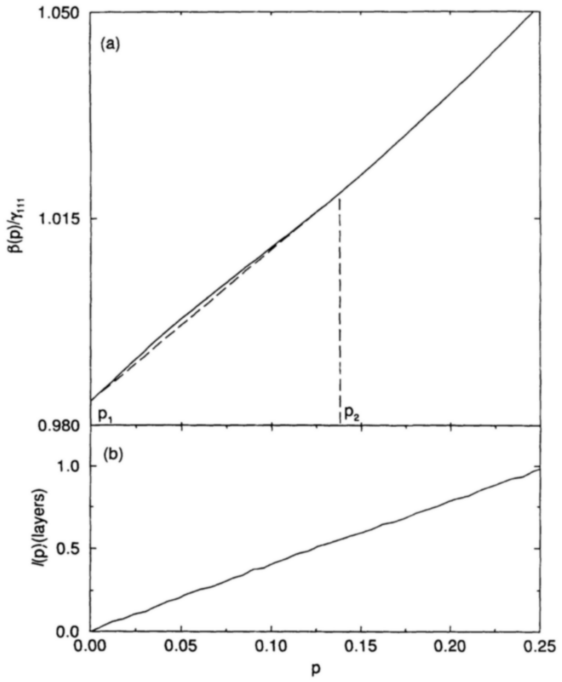

Figure 2.4: Free energy curve from Stewart [55]. β is the projection of the free energy on to a plan parallel to the facet, p is the slop of the surface, proportional to n in Eqn. 2.37.

between the non-wetted facet and the partially wetted orientations.

2.2.3 Experimental Evidence

The most extensive evidence of surface melting is from experiments by Frenken and van der Veen[23, 47] using a technique based on ion shadowing and blocking. In these experiments a collimated ion beam is incident on a crystalline surface and aligned with a major crystalline axis. The scattered ions are measured at a detector positioned so that the direction from the detector to the illuminated spot is also a crystallographic direction. In this geometry the only scattering contribution at the detector will be from surface atoms. All other atoms will be shadowed from the incident ion by the top layer and blocked from the view of the detector by the surface layer. If the surface becomes less ordered, some fraction of the ion bean can be scattered from internal portions of the crystal and be measured by the detector. This contribution is shifted downward in energy because of loss to the lattice.

For a 97.5keV proton beam incident on Pb, the stopping power of the lattice was calculated to be 13.7eV/Å. With an energy discriminating detector with a relative sensitivity of $\delta E/E = 4 \times 10^{-3}$, the depth to which ions incident along the $(\bar{1}01)$ of a Pb crystal with (110) orientation, a depth resolution of 7.1Å was possible[23]. Results of varying the sample temperature showed very little signal from layers beneath the surface until a temperature of 500K. The number of visible layers increased from three at 500K to six at 560K. From there the number of visible layers increase asymptotically as the temperature approached T_m.

Similar experiments were carried out on a cylindrically cut crystal of Pb[47]. By measuring translating the sample, different orientations of Pb were exposed to the ion beam. These measurements showed no visible disorder in the Pb(111) close packed face up to T_m. Other non-low index orientations showed more than $6 \times 10^{15}\text{cm}^{-2}$ disordered atoms at $T_m - 0.05K$.

Chapter 3

Scattering and CXD Theory

3.1 Kinematic Scattering

The portions of this introduction to X-ray scattering deriving the scattered wavefield from a single electron (Section 3.1.1) through scattering from a continuous charge density (Section 3.1.3) follow the texts of Warren[62] and Als-Nielsen[7]. Latter sections follow crystallographic conventions as found in Ashcroft and Mermin[9], but the derivation was carried out in a non-standard way, relying heavily on use of the convolution theorem to derive scattering from 1D and higher dimensional lattices, and then finite lattices with strain.

3.1.1 Scattering from One Electron

The origin of X-ray diffraction is dipole radiation from electrons accelerating under the influence of the incident electromagnetic wave. Assuming the electromagnetic wave is a perfectly polarized plane wave propagating in the z direction, we can write the wavefield in cgs and using complex notation as

$$\mathbf{E_0} = E_0 e^{i(\omega t - kz)} \hat{x} \tag{3.1}$$

$$\mathbf{B_0} = B_0 e^{i(\omega t - kz)} \hat{y}. \tag{3.2}$$

Under such an electric field, an electron is accelerated as

$$\mathbf{a} = \frac{e}{m_e}\mathbf{E_0} = \frac{e}{m_e} E_0 e^{i(\omega t - kz)} \hat{x}, \tag{3.3}$$

where e and m_e are the charge and mass of the electron. An accelerating electron produces an electric field

$$E_1 = \frac{ea\sin\alpha}{c^2 R}, \tag{3.4}$$

where R is the distance from the charge, c is the speed of light, and α is the angle between the direction of the acceleration and the vector connecting the charge and the point at which the field is measured. Any change in the electric field caused by a change in a must propagate with the speed of light, meaning that an electron under the influence of of electromagnetic field emits dipole radiation:

$$E_1 = \frac{e^2 E_o}{m_e c^2 R}\sin\alpha\, e^{i(\omega(t-R/c)-kz)} \tag{3.5}$$

$$= \frac{e^2 E_o}{m_e c^2 R}\sin\alpha\, e^{i(\omega t - kR - kz)}. \tag{3.6}$$

3.1.2 Scattering from Multiple Charges

The phase of an X-ray frequency electromagnetic wave is not directly measurable; it only is important if the wave interacts with another, in which case their relative phase determines how they interfere. It is now useful to define a few more variables, shown in Fig. 3.1: $\mathbf{r_n}$ is the vector from an origin within the charge distribution to a charge n, z_n is the difference in distance traveled by the incoming wave before reaching n relative to the origin, $\mathbf{r'_n}$ is the vector from charge n to a point $\mathbf{P}$, and$\mathbf{k_f}$ is the wavevector of the scattered radiation in the direction of $\mathbf{P}$. The distance to the measurement point $\mathbf{P}$ must be much larger than the range of $\mathbf{r_n}$'s. The optical path traveled by radiation scattered from n relative to the origin is

$$d_1 = (z_1 + r'_1)k \tag{3.7}$$

$$= \mathbf{k}_i \cdot \mathbf{r_1} + \mathbf{k}_f \cdot (\mathbf{P} - \mathbf{r_1}) \tag{3.8}$$

$$= (\mathbf{k}_i - \mathbf{k_f}) \cdot \mathbf{r_1} + Rk_f. \tag{3.9}$$

The R term can be dropped in writing the relative optical paths for different scatterers, since it is the same for all. The change of scattering vectors is typically written as $\mathbf{Q}$=$\mathbf{k}_f$-$\mathbf{k}_i$, allowing the instantaneous electric field scattered

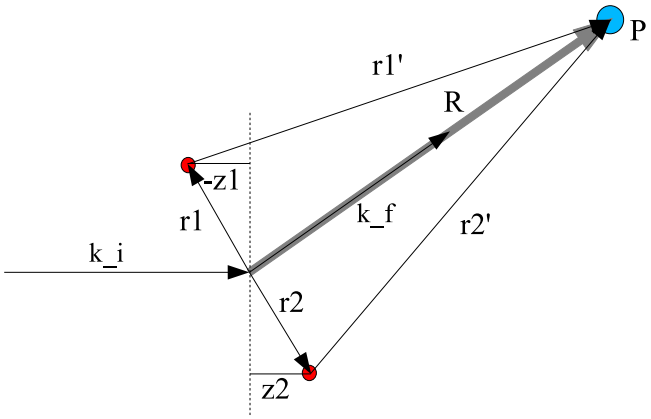

Figure 3.1: Geometry of a two electron scattering system, excited by incident EM wave with wave vector $\mathbf{k}_i$. Their radiation is measured at the point $\mathbf{P}$, which is much further from the origin than $\mathbf{r}_1$ or $\mathbf{r}_2$.

from a group of electric charges to be written as

$$E = \frac{e^2 E_o}{m_e c^2 R} \sin\alpha \sum e^{i(\omega t - (\mathbf{k_i} - \mathbf{k_f})\cdot \mathbf{r}_n - R k_f)} \tag{3.10}$$

$$= \frac{e^2 E_o}{m_e c^2 R} \sin\alpha \sum e^{i(\omega t + \mathbf{Q}\cdot \mathbf{r}_n - R k_f)}. \tag{3.11}$$

3.1.3 Scattering from Continuous Charge Distribution

From quantum mechanics we know that an electron in an atom is not confined to a single point but must be expressed as a charge density. Here we define a normalized electron density ρ_e such that the integral over all space $\int \rho_e(\mathbf{r}) d\mathbf{r} = 1$. The scattering from a quantum mechanical electron is then

$$E = \frac{e^2 E_o}{m_e c^2 R} e^{i\omega t} \sin\alpha \int \rho_e(\mathbf{r}) e^{i\mathbf{Q}\cdot\mathbf{r}} d\mathbf{r} \tag{3.12}$$

$$= \frac{e^2 E_o}{m_e c^2 R} e^{i\omega t} \sin\alpha \, f_e(\mathbf{Q}) \tag{3.13}$$

where $f_e(\mathbf{Q}) = \int \rho_e(\mathbf{r}) e^{i\mathbf{Q}\cdot\mathbf{r}} d\mathbf{r}$ is the ratio of scattered amplitude of a quantum mechanical electron to a classical one.

It is useful to express this last step in terms of the convolution theorem,

which will be used in the next section and is critical to the understanding of the Fourier transforms of functions. The convolution of two functions $f(\mathbf{r})$ and $g(\mathbf{r})$ is defined as

$$f(\mathbf{r}) \otimes g(\mathbf{r}) = \int f(\mathbf{r}')g(\mathbf{r}-\mathbf{r}')d\mathbf{r}'. \tag{3.14}$$

If $f(\mathbf{r})$ and $g(\mathbf{r})$ have Fourier transforms $F(\mathbf{Q})$=$\mathcal{F}\{f(\mathbf{r})\}$ and $G(\mathbf{Q})$=$\mathcal{F}\{g(\mathbf{r})\}$, then the convolution theorem states that the Fourier transform of their convolution is the product of their Fourier transforms,

$$\mathcal{F}\{f(\mathbf{r}) \otimes g(\mathbf{r})\} = \mathcal{F}\{f(\mathbf{r})\}\mathcal{F}\{g(\mathbf{r})\}. \tag{3.15}$$

Likewise, because the relationship of the Fourier transform and its inverse,

$$\mathcal{F}\{f(\mathbf{r})g(\mathbf{r})\} = \mathcal{F}\{f(\mathbf{r})\} \otimes \mathcal{F}\{f(\mathbf{r})\}. \tag{3.16}$$

Although extension from discrete scatterers in Eqn. (3.11) to a continuum in Eqn. (3.12) is intuitive, it can be justified by rewriting (3.11) as

$$\mathbf{E} = \frac{e^2 E_o}{m_e c^2 R} e^{i\omega t} \sin\alpha \sum \int \delta(\mathbf{r}' - \mathbf{r}_n) e^{i\mathbf{Q}\cdot\mathbf{r}'} d\mathbf{r}', \tag{3.17}$$

where the sum is now of complex phase factors evaluated at points which are the exact electron positions and the constant e^{-iRk_f} has been dropped. If we now consider a single electron which, instead of having a location classically described by Dirac delta function is more accurately described by a delta function specifying the location of the electron convolved with a function $\rho_e(\mathbf{r})$ giving the distribution of charge, then the scattering is given by

$$E = \frac{e^2 E_o}{m_e c^2 R} e^{i\omega t} \sin\alpha \int \delta(\mathbf{r} - \mathbf{r}_0) \otimes \rho_e(\mathbf{r}) e^{i\mathbf{Q}\cdot\mathbf{r}} d\mathbf{r} \tag{3.18}$$

$$= \frac{e^2 E_o}{m_e c^2 R} e^{i\omega t} \sin\alpha \, \mathcal{F}\{\delta(\mathbf{r} - \mathbf{r}_0)\}\mathcal{F}\{\rho_e(\mathbf{r})\} \tag{3.19}$$

$$= \frac{e^2 E_o}{m_e c^2 R} e^{i\omega t} \sin\alpha \, e^{i\mathbf{Q}\cdot\mathbf{r}_0} f_e(\mathbf{Q}). \tag{3.20}$$

If the origin is chosen such that $\mathbf{r}_0 = 0$ then this is identical to Eqn. (3.13).

3.1.4 Diffraction from an Infinite Lattice

A perfect crystal contains atoms arrayed on an infinite lattice. Each atom is made up of many electrons, usually in near-spherical symmetry (the outer shell may not be symmetric, but all closed shells are, so for most purposes the spherical approximation holds). In this case the scattering from a single atom,

$$E = \frac{e^2 E_o}{m_e c^2 R} e^{i\omega t} \sin\alpha \, e^{i\omega t} \int \rho_n(\mathbf{r}) e^{i\mathbf{Q}\cdot\mathbf{r}} d\mathbf{r} \tag{3.21}$$

where $\rho_n(\mathbf{r})$ is electron density of an atom, is independent of the direction of $\mathbf{Q}$, so the contribution of the atomic electron density to the scattering is a scale factor which decreases with increasing $|\mathbf{Q}|$.

The lattice of a crystal can be broken down into a unit cell, the base repeat unit, convolved with an infinite series of delta functions giving the spacing between the origins of unit cells. More explicitly,

$$\sum_{n}^{unitcell} \rho_n(\mathbf{r} - \mathbf{r}_n) \otimes \sum_{m_{1,2,3}=-\infty}^{\infty} \delta(\mathbf{r} - m_1\mathbf{a} - m_2\mathbf{b} - m_3\mathbf{c}) \tag{3.22}$$

where $\mathbf{a}$, $\mathbf{b}$, $\mathbf{c}$, describe the repeat of the unit cell, $\rho_n(\mathbf{r})$ is the electron density of the n'th atom in the unit cell, and $\mathbf{r}_n$ is the center of the n'th atom.

We know from the convolution theorem, Eqn. (3.15) that the diffraction from the density described in Eqn. (3.22) will be proportional to the product of the Fourier transforms of the unit cell and the lattice. To evaluate the Fourier transform of the infinite lattice it is convenient to consider first the one dimensional case, where $\rho_L(x) = \sum_{n=-\infty}^{\infty} \delta(x - na)$. Because this function repeats with a period of a, it can be expressed as a Fourier series

$$\rho_L(x) = \sum_{n=-\infty}^{\infty} \delta(x - na) = \sum_{m=-\infty}^{\infty} c_m e^{2\pi i m x/a}, \tag{3.23}$$

where

$$c_m = \frac{1}{a} \int_{-a/2}^{a/2} \delta(x) e^{-2\pi i m x/a} dx = \frac{1}{a}, \tag{3.24}$$

leading to

$$\rho_L(x) = \sum_{m=-\infty}^{\infty} \frac{1}{a} e^{2\pi i m x/a}. \tag{3.25}$$

The exponential can be rewritten as an integral over q using the "picking"

property of delta functions to sample other functions when multiplied by them and under integration:

$$\rho_L(x) = \sum_{m=-\infty}^{\infty} \frac{1}{a} \int \delta\left(q - \frac{2/\pi}{a} m\right) e^{2\pi i x q} dq \tag{3.26}$$

$$= 2\pi \mathcal{F}^{-1}\{ \sum_{m=-\infty}^{\infty} \delta\left(q - \frac{2/\pi}{a} m\right)\}. \tag{3.27}$$

The Fourier transform of an infinite series of delta functions with a spacing of a is an infinite series of delta functions with a spacing of $\frac{2\pi}{a}$.

The extension of this result to higher dimensions is fairly simple, and is demonstrated by Fig. 3.2. A multidimensional infinite lattice can be written as a convolution of one dimensional infinite lattices. The Fourier transform of each 1D lattice is a series of delta functions in one dimension, with the other dimensions being unconstrained, *i.e.*, a line in two dimensions and a plane in three dimensions. The Fourier transform the the multidimensional lattice is then the product of the Fourier transforms of individual one dimensional lattices, producing a reciprocal space lattice. The three dimensional result for the transform of a real space lattice describe by the vectors **a**, **b**, **c** is an infinite lattice described by vectors **a***, **b***, **c*** defined by

$$\mathbf{a}^* = 2\pi \frac{\mathbf{b} \times \mathbf{c}}{\mathbf{a} \cdot \mathbf{b} \times \mathbf{c}} \qquad \mathbf{b}^* = 2\pi \frac{\mathbf{c} \times \mathbf{a}}{\mathbf{a} \cdot \mathbf{b} \times \mathbf{c}} \qquad \mathbf{c}^* = 2\pi \frac{\mathbf{a} \times \mathbf{b}}{\mathbf{a} \cdot \mathbf{b} \times \mathbf{c}}. \tag{3.28}$$

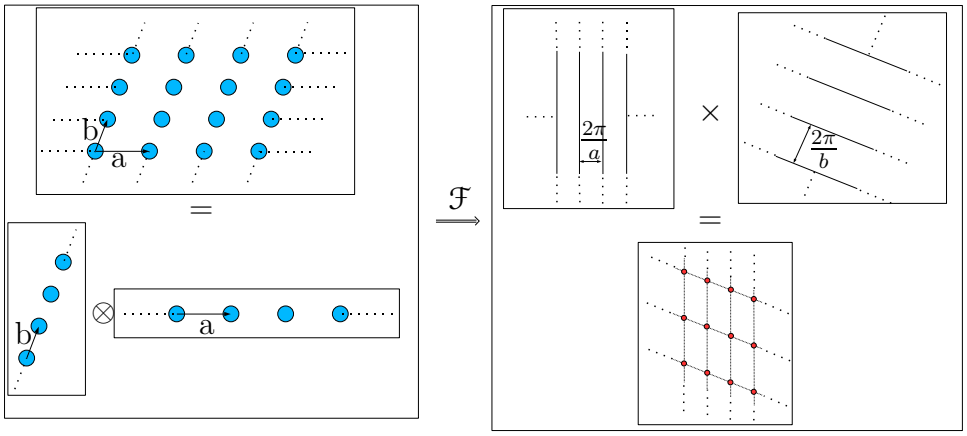

Figure 3.2: Two dimensional real and reciprocal space infinite lattices. The 2D real space lattice (top left) can be thought of as the convolution of two 1D lattices (bottom left). The Fourier transform then should be the product of the Fourier transforms of the two 1D lattices (top right), which are sets of lines. Their product is the lattice given by the intersection of the lines.

Combining Eqns. (3.21) and (3.22)

$$E = \frac{e^2 E_o}{m_e c^2 R} e^{i\omega t} \sin\alpha \int \sum_n^{unitcell} \rho_n(\mathbf{r} - \mathbf{r}_n)$$

$$\otimes \sum_{m_{1,2,3}=-\infty}^{\infty} \delta(\mathbf{r} - m_1\mathbf{a} - m_2\mathbf{b} - m_3\mathbf{c}) e^{i\mathbf{Q}\cdot\mathbf{r}} d\mathbf{r} \tag{3.29}$$

$$= \frac{e^2 E_o}{m_e c^2 R} e^{i\omega t} \sin\alpha \sum_n^{unitcell} \int \rho_n(\mathbf{r}) \otimes \delta(\mathbf{r} - \mathbf{r}_n) e^{i\mathbf{Q}\cdot\mathbf{r}} d\mathbf{r}$$

$$\times \mathcal{F}\{ \sum_{m_{1,2,3}=-\infty}^{\infty} \delta(\mathbf{r} - m_1\mathbf{a} - m_2\mathbf{b} - m_3\mathbf{c})\} \tag{3.30}$$

$$= \frac{e^2 E_o}{m_e c^2 R} e^{i\omega t} \sin\alpha \sum_n^{unitcell} f_n(\mathbf{Q}) e^{i\mathbf{Q}\cdot\mathbf{r}_n}$$

$$\times \sum_{m_{1,2,3}=-\infty}^{\infty} \delta(\mathbf{Q} - m_1\mathbf{a}^* - m_2\mathbf{b}^* - m_3\mathbf{c}^*) \tag{3.31}$$

$$= \frac{e^2 E_o}{m_e c^2 R} e^{i\omega t} \sin\alpha \; F(\mathbf{Q}) \sum_{m_{1,2,3}=-\infty}^{\infty} \delta(\mathbf{Q} - m_1\mathbf{a}^* - m_2\mathbf{b}^* - m_3\mathbf{c}^*). \tag{3.32}$$

The scattering is then in the form of a polarization factor times an infinite lattice in momentum space, modified by the structure factor $F(\mathbf{Q})$. The

points on this modified lattice are called Bragg peaks.

3.1.5 Coherent Diffraction from a Finite Crystal

The previous derivation is somewhat unphysical in that it assumes perfect coherence and an infinite lattice. Traditional X-ray diffraction from a large crystal involves either a partially coherent beam, in which case the Bragg peaks are broadened by convolution with the Fourier transform of the partial coherence function, or else there are domains smaller than the coherence length of the beam, with small angular or spacial offsets between lattices of different domains causing diffraction from individual domains to add up incoherently.

The diffraction of a coherent X-ray beam by a finite single crystal, in Eqn. (3.33) on the other hand, is analogous to the derivation above with the exception that the real space lattice is multiplied by a shape function $s(\mathbf{r})$, which is zero outside the crystal and for an unstrained, ideal crystal is unity inside. Again calling upon the convolution theorem, the Fourier transform of the shape function times the real space lattice is the the convolution of the Fourier transforms of the shape function and the real space lattice, as shown in Eqn. (3.34). This means that there will be a distribution of amplitude around each Bragg peak given by the Fourier transform of the shape of the object. If a crystal is hundreds of nanometers across, its shape function will be 1000 times the spacing of the real space lattice, so its Fourier transform will have a size scale 1/1000 of the reciprocal space lattice. Because of its size scale, $F(\mathbf{Q})$ and sinα can be considered constants over a single pattern, simply scaling it by their value at the Bragg peak. This means that surrounding each Bragg peak is a copy of the Fourier transform of the shape of the diffracting crystal.

$$E = \frac{e^2 E_o}{m_e c^2 R} e^{i\omega t} \sin\alpha \int \sum_{n}^{unitcell} \rho_n(\mathbf{r} - \mathbf{r}_n) \otimes s(\mathbf{r}) \sum_{m_{1,2,3}=-\infty}^{\infty} \delta(\mathbf{r} - m_1\mathbf{a} - m_2\mathbf{b} - m_3\mathbf{c}) e^{i\mathbf{Q}\cdot\mathbf{r}} d\mathbf{r} \tag{3.33}$$

$$= \frac{e^2 E_o}{m_e c^2 R} e^{i\omega t} \sin\alpha \; F(\mathbf{Q}) \left(\mathcal{F}\{s(\mathbf{r})\} \otimes \sum_{m_{1,2,3}=-\infty}^{\infty} \delta(\mathbf{Q} - m_1\mathbf{a}^* - m_2\mathbf{b}^* - m_3\mathbf{c}^*) \right) \tag{3.34}$$

The presence of strain in the crystal can be written as a $\mathbf{u}(\mathbf{r}_m)$, the displacement of the local lattice from an ideal reference lattice. Implementing the shorthand notation of a single 3 dimensional index m and $\mathbf{r}_m = m_1\mathbf{a} + m_2\mathbf{b} + m_3\mathbf{c}$, and replacing the prefactor with a constant $C = \frac{e^2 E_o}{m_e c^2 R} e^{i\omega t} \sin\alpha$, we can then write the X-ray scattering from this crystal as,

$$E = C \int \sum_{n}^{unitcell} \rho_n(\mathbf{r} - \mathbf{r}_n) \otimes s(\mathbf{r}) \sum_{m=-\infty}^{\infty} \delta(\mathbf{r} - \mathbf{r}_m - \mathbf{u}(\mathbf{r}_m)) e^{i\mathbf{Q}\cdot\mathbf{r}} d\mathbf{r} \tag{3.35}$$

$$\simeq C F(\mathbf{Q}) \sum_{m=-\infty}^{\infty} s(\mathbf{r}_m + \mathbf{u}(\mathbf{r}_m)) e^{i\mathbf{Q}\cdot(\mathbf{r}_m + \mathbf{u}(\mathbf{r}_m))} \tag{3.36}$$

$$\simeq C F(\mathbf{Q}) \sum_{m=-\infty}^{\infty} s(\mathbf{r}_m) e^{i\mathbf{Q}\cdot\mathbf{u}(\mathbf{r}_m)} e^{i\mathbf{Q}\cdot\mathbf{r}_m} \tag{3.37}$$

$$\simeq C\, F(\mathbf{Q}) \int \sum_{m=-\infty}^{\infty} s(\mathbf{r}) e^{i\mathbf{Q}\cdot\mathbf{u}(\mathbf{r})} \delta(\mathbf{r} - \mathbf{r}_m) e^{i\mathbf{Q}\cdot\mathbf{r}} d\mathbf{r} \tag{3.38}$$

$$\simeq C\, F(\mathbf{Q}) \int s(\mathbf{r}) e^{i\mathbf{Q}\cdot\mathbf{u}(\mathbf{r})} d\mathbf{r} \otimes \sum_{m=-\infty}^{\infty} \delta(\mathbf{Q} - \mathbf{G}_m). \tag{3.39}$$

Between Eqn. (3.36) and Eqn. (3.37) the assumption was made that $\mathbf{u}(\mathbf{r}_m) \ll \mathbf{r}_m$, simply stating that local distortions in the variation in the lattice spacing is much less than the lattice spacing. Here the points on the reciprocal lattice are written as $\mathbf{G}_m$. If the maximum value of $\mathbf{u}(\mathbf{r})$ is small enough that $\mathbf{q} \cdot \mathbf{u}(\mathbf{r}) \ll \pi$, where $\mathbf{q} = Q - \mathbf{G}_m$, then in the vicinity of a single Bragg

peak, the diffracted wave field can be written as

$$E = \frac{e^2 E_o}{m_e c^2 R} e^{i\omega t} \sin\alpha \, F(\mathbf{G}_m) \int s(\mathbf{r}) e^{\mathbf{G}_m \cdot \mathbf{u}(\mathbf{r})} e^{i\mathbf{q}\cdot\mathbf{r}} d\mathbf{r}. \tag{3.40}$$

The diffraction in the vicinity of a Bragg peak from a strained crystal coherently illuminated is proportional to the Fourier transform of a complex shape function, where the phase factor is the strain projected onto the reciprocal lattice vector of the Bragg peak.

3.2 Phase Retrieval

If the amplitude of the diffracted wave field could be directly measured, it could be inverted via Fourier transform to recover the diffracting charge distribution. Because of the frequencies of X-rays, it is impossible to directly measure their phase. Fortunately for a band-limited signal, such as diffraction from a finite object, that phase information is encoded in an intensity measurement which is sampled at a sufficiently fine interval.

3.2.1 Oversampling

Shannon's theorem states that to record all the information in a signal for which the maximum frequency present is known to be f_0, the signal must be sampled at a frequency of $2f_0$. Sayre[53] observed that this implied that if square modulus of the signal is to be measured, it must be sampled at $4f_0$, or oversampled by a factor of two. This is a result of the fact that if the original signal $A(q)$ can be written as the Fourier transform of $\rho(r)$,

$$A(q) = \mathcal{F}\{\rho(r)\} \tag{3.41}$$

then its square modulus $I(q) = A^*(q)A(q)$, where $A^*(q)$ is the complex conjugate of $A(q)$ then $I(q)$ can be written as the Fourier transform of the autocorrelation function

$$I(q) = \mathcal{F}\{(\rho(r) \otimes \rho(r)\}. \tag{3.42}$$

Because the maximum possible extent of the autocorrelation of a discrete function is twice the size of the extent of the original function, the band

limit of $I(q)$ is twice that of $A(q)$.

3.2.2 Iterative Phase Retrieval Algorithms

Gerchberg and Saxton[24, 25] applied the first iterative technique involving real space and reciprocal space techniques to recover phase information. Knowing the density of a thin sample from electron transmission experiments plus a diffraction from the same sample, the modification of the phase of the electron beam by the sample was recovered by iteratively applying the known amplitudes in real and reciprocal space.

Fienup[21] showed that this iterative technique could be extended to the case of amplitude measurements used as the reciprocal space constraint of the algorithm and finite extent and zero phase as real space constraint. This finite extent constraint is applied in practice by defining a region in real space called the support in which the amplitude may be non-zero. Inside the support any points with a negative real part are set to zero. If the real part is positive then any complex part of the value of the point is set to zero. With these constraints the algorithm is mathematically equivalent to an error reduction, or ER, algorithms. It therefore suffers from the same problems with stagnation inherent in any method of steepest descents calculation. Once a local minimum is reached in parameter space the algorithm remains there. For any function $\rho(r)$ which produces a signal $I(q)$, its dual $\rho^*(-r)$ produces the same signal $I(q)$. Because of this degeneracy, real space solutions which are a combination of $\rho(r)$ and $\rho^*(-r)$ are typically local minima and therefore stagnation points of the algorithm.

Fienup[21] proposed a hybrid input-output algorithm, or HIO, which has the property of avoiding local minima and approaching the vicinity of the global minimum. Defining the iterative value of $\rho(r)$ and $A(q)$ during iteration k as $\rho_k(r)$ and $A_k(q)$, and $\rho'_k(r) = \mathcal{F}^{-1}\{A_k(q)\}$ and $A'_k(q) = \mathcal{F}\{\rho_k(r)\}$, HIO set the next real space iterate as

$$\rho_{k+1}(r) = \begin{cases} \rho'_k(r), & \rho'_k(r) \in S \\ \rho_k(r) - \beta\rho'_k(r), & \rho'_k(r) \notin S. \end{cases} \tag{3.43}$$

The reciprocal space constraint is applied in the same manner as in ER; $A_k(q) = \sqrt{I(q)}e^{i\phi_k(q)}$, where $A'_k(q) = |A'_k(q)|e^{i\phi_k(q)}$. If a given point in the

current real space iterate meets the real space constraint S, *i.e* it has zero amplitude if outside the support region and it meets the phase constraint (which may be positivity, zero phase, or no constraint) then the value for that point is not changed before the function is Fourier transformed to get the next 'guess' for A(q). If the real space iterate does not meet the constraints then its value is driven away from its current iterate, using the mixing parameter β, which can range between 0.5 and 1. This means that although for each iteration of ER the current iterate in both real in reciprocal space are the best guesses for the final values of the functions to be required, this is not necessarily true of HIO. A strong advantage of HIO is it is far less susceptible to stagnation about local minima in the free energy.

Millane[43] proposed a version of HIO in which a tolerance parameter ϵ is used to determine whether a real space iterate is "close enough" to meeting the constraints that it is unaltered by the routine. Defining $c_k(r)$ as the constrained version of $\rho'_k(r)$, Millane's algorithm is described by

$$\rho_{k+1}(r) = \begin{cases} \rho'_k(r), & |\rho'_k(r) - c_k(r)| \leq \epsilon \\ \rho_k(r) + \beta(c_k(r) - \rho'_k(r)), & \|\rho'_k(r) - c_k(r)| > \epsilon \end{cases} \tag{3.44}$$

in real space. The same reciprocal space constraint, the known Fourier modulus, is applied.

Recently Elser[19] has proposed a much more general phasing algorithm. Elser describes the application of real and reciprocal space constraints in terms of projection operators, π, which act vectors ρ in an N dimensional space. The finite support projection operator π_S is defined as

$$\pi_s\rho(r) = \begin{cases} \rho(r), & r \in S \\ 0, & r \notin S \end{cases} \tag{3.45}$$

The Fourier modulus projection operator, π_M acts by Fourier transforming ρ, then setting the magnitude of the amplitudes to the square root of the measured intensities, and applying a back Fourier transform. This is identical to one half of the ER and HIO algorithms, but it is restated as a real space operator.

Using Elser's terminology, the ER algorithm can be rewritten as

$$\rho_{k+1} = \pi_s \pi_+ \pi_M \rho_k \tag{3.46}$$

where π_+ is the positivity projection operator. Elser describes a "difference map" algorithm which iteratively applies the operator

$$D = 1 + \beta\Delta \tag{3.47}$$

where β is a real non-zero number and Δ is defined as

$$\Delta = \pi_1 f_2 - \pi_2 f_1. \tag{3.48}$$

The 'maps' f_i are operators defined as

$$f_i = (1 + \gamma_i)\pi_i - \gamma_i \tag{3.49}$$

where γ_i is a real number. This generalized algorithm reproduces Fienup's HIO algorithm when $\gamma = -1$ and $\gamma = 1/\beta$. Because of the greater flexibility of Elser's difference map, the algorithms behavior with different sets of parameters is still being investigated, including studies of simulated noisy diffraction patterns from a discrete, continuous object by Williams[63] *et al.*

3.2.3 Alternative Methods

An alternative approach is to call on Bayesean statistics to describe the probability of the truth of a model based on multiple conditions, the maximum entropy method[52] attempts to maximize $exp(S/\alpha - \chi^2/2)$, where the 'entropy' $S = \alpha \log\Omega$, Ω being the number of ways a distribution may have come about and α is a constant. S is a real space measurement of the probability that a measurement is physically correct. Here χ^2 is an error metric comparing experimental and measured diffraction amplitudes, normalized by the estimated error in the measurement. Application of this powerful technique requires *a priori* knowledge of the probability of the electron density to take a particular configuration.

Direct phasing of the diffraction pattern, or holography, can be accomplished if a reference wave is present. In this case autocorrelation function

of the sample, given by the Fourier transform of the measured intensity, includes convolution of the sample with the image of the source of the reference wave. This technique requires preparation of a sample with a reference source separated from the diffracting object of interest by greater than the extent of the diffracting object, yet the distance from the reference source to the furthest point on the diffracting object must be less than a coherence length of the radiation used for the measurement. The advantage of this technique is that the image is obtained directly by Fourier transforming the intensity of the diffraction pattern without the iterative phasing step. This technique has been used by Eisebitt[18] *et al.* using soft X-rays and a patterned mask which included a pinhole for the reference wave and a support region which contained the magnetic material to be studied, and by Spence[26] *et al.* using 50 nm gold balls as the reference source and imaged objects. This method produces an image with a resolution given by the size of the source of the reference wave, which may then be used as support or starting point for an iterative phasing algorithm.

3.2.4 Uniqueness of Solution

Bates[11] demonstrated that for a localized image the solution to the phase retrieval problem is nearly always unique, disregarding trivial ambiguities which are necessarily present. These ambiguities are the shifting of the diffracting object, since $|\mathcal{F}\{\rho(x)\}|^2 = |\mathcal{F}\{\rho(x - x_0)\}|^2$. An additional ambiguity is that the dual of an object produces the same Fourier modulus, $|\mathcal{F}\{\rho(x)\}|^2 = |\mathcal{F}\{\rho^*(-x)\}|^2$, where $\rho^*(r)$ is the complex conjugate of $\rho(r)$. Barakat and Newsam[10] proved that in dimensions greater than one, non-uniqueness is pathologically rare for the case of a perfect measurement. Non-uniqueness occurs whenever the amplitude of the diffracted wavefield is factorizable.

Consider a solution pair $A_1(q) = \mathcal{F}\{\rho_1(x)\}$, where $A_1(q)$ is factorizable into $A_1(q) = F(q)G(q)$, where $F(q) = \mathcal{F}\{f(x)\}$ and $G(q) = \mathcal{F}\{g(x)\}$. The real space solution can be written as $\rho_1(x) = f(x) \otimes g(x)$. It can be easily shown that $F^*(q) = \mathcal{F}\{f^*(-x)\}$. The solution $A_2(q) = F^*(q)G(q)$ will therefore share the same Fourier modulus as $A_1(q)$,

$$|A_1^*(q)A_1(q)| = \sqrt{F(q)G^*(q)F^*(q)G(q)} = |A_2^*(q)A_2(q)| \tag{3.50}$$

yet typically correspond to a different real space object,

$$\mathcal{F}^{-1}\{A_2(q)\} = f^*(-x) \otimes g(x) \neq f(x) \otimes g(x) \tag{3.51}$$

These functions are only equivalent if $f(x) = f^*(-x)$ or $g(x) = g^*(-x)$. Barakat and Newsam demonstrate that this is the only source of non-uniqueness and that in dimensions higher than one for perfect data the situation is extremely rare.

Examples of iterative algorithms applied to oversampled X-ray data include experiments by Robinson *et al.* to phase 1D X-ray reflectivity patterns[59, 48] from a Si sample during oxide formation to recover the sample's height profile. This has been extended to recover a 2D projection of a nanocrystal from a single slice through the center of a diffraction pattern by Robinson[49] *et al.*, and 3D using a transmission based technique by Miao[42] *et al.* and using diffraction by Robinson[64] *et al.*.

A series of **2dmultifit** were written by J. Pitney to apply various phase retrieval algorithms to 2D measured diffraction patterns. **3dmultifit2** was written by Garth Williams and modified by myself to implement phase iterative phase retrieval algorithms to 3D data. This program caries out a user specified number of fits to the amplitude data it reads in, each fit starting with random initial conditions. A single fit in **3dmultifit2** is typically made up of multiple cycles of a number of iterations of a specified modes. These modes, listed in 3.1, include ER, Fienup HIO with ϵ, Millane HIO. The Fienup HIO includes the ϵ factor associated with Millane HIO, but it only applies the positivity and finite support constraints in real space, as is standard for Fienup HIO. With $\epsilon = 0$ it is exactly equal to Fienup's original algorithm. The Millane HIO implemented in **3dmultifit2** includes the constraint that the real space phase must be zero. Additional modes were written specifically to phase the data presented in this thesis. These include modes which strictly enforce the constraints, as with ER. Their constraints are finite support only, a fixed amplitude constraint, and a fixed phase constraint. These last two were intended to work as a pair alternating between a few iterations of each. The support only constraint was used extensively in this work.

mode	description
4	Millane HIO
5	Error Reduction
17	Fienup HIO
18	ER with finite support only
19	ER, fixed amplitude (free phase)
20	ER, fixed phase (free amplitude)

Table 3.1: **3dmultifit2** modes.

3.3 Sampling

Because a full 3D coherent X-ray diffraction pattern from a sub-micron sample takes many ($\sim$ 10) hours to record, it is prudent to examine whether useful shape information can be recovered from a single 3D slice through a 3D pattern. To define a single slice of a diffraction pattern we express the Fourier transform $A(\mathbf{q})$ in coordinates parallel (q_x and q_y) and perpendicular (q_z) to a hypothetical detector plane,

$$A(q_x, q_y, q_z) = \int\int\int \rho(x, y, z) e^{i(q_x x + q_y y + q_z z)} dx dy dz. \tag{3.52}$$

Taking a slice through the center of the diffraction pattern is equivalent to setting one of the q's equal to zero,

$$A(q_x, q_y, 0) = \int\int\int \rho(x, y, z) dz e^{i(q_x x + q_y y)} dx dy. \tag{3.53}$$

There is no longer any phase factor associated with the variable z, so integrating with respect to z simply projects the crystal density on the $x - y$ plane. Defining $\rho'(x, y)$ as that projection,

$$A(q_x, q_y, 0) = \int\int \rho'(x, y) e^{i(q_x x + q_y y)} dx dy. \tag{3.54}$$

The central slice through a 3D diffraction pattern is the square modulus of the Fourier transform of a projection of the crystal's density, which should be recoverable using a phase retrieval algorithm.

It is necessary to ask how precisely does this diffraction pattern need to pass through the center of the 3D pattern, since the θ motor of the diffractometer used for much of this experiment was only accurate to approximately

0.01°. Consider a 2D diffraction pattern a small distance of $q_z = \delta q$ away from passing through the center of the pattern. Eqn. (3.54) becomes

$$A(q_x, q_y, \delta q) = \int\int\int \rho(x, y, z) e^{i\delta q_z z} dz e^{i(q_x x + q_y y)} dx dy. \tag{3.55}$$

Instead of measuring the Fourier transform of a projection of the density, we are measuring the transform of a projection of a complex value. If we examine a sphere as a test crystal shape, the projected density in the center is decreased more than at the edges since the crystal is thicker in the center, resulting in a wider variance of the phase. This is problematic if we wish to examine the change in a crystal's shape and density profile as it approaches its melting point, since the relative density at the center and near the edges is expected to be an important factor.

I carried out simulation of diffraction patterns from spherical crystals of diameter 9 pixels in a $50 \times 50 \times 50$ array. To simulate misalignment of the pattern I applied a linear phase gradient to the real space simulations before Fourier transforming them and removing phase information. I then performed phase retrieval calculations using ER on just the centermost slice as described in Eqn. (3.55) and on the whole 3D array. The normalized error metric, χ^2, of the 2D fits was a constant (1×10^{-10}) for numerous offsets between 0 and 1 slice as expected for an object with a mirror plane. For a measured or simulated intensity $I(i)$ and a calculated amplitude $A(i)$ returned by the fitting routine, both with values over N pixels, the error metric is defined as,

$$\chi^2 = \frac{\sum_{i=1}^{N} I(i) - |A(i)|^2}{\sum_{i=1}^{N} I(i)}. \tag{3.56}$$

χ^2=0 denotes perfect agreement of the solution with the constraints, *i.e.* a solution which agrees perfectly with both the real space and reciprocal space constraints was found. The only differences in the fits were the relative intensities of the center and edges of the reconstructed crystal, with less intensity near the center for the larger phase offsets. Carrying out the same calculations on 3D crystals led to a much greater change in the error metric, as shown in Fig. 3.3.

A more physically meaningful simulation would be a sphere truncated by a plane, similar to a high temperature equilibrium shape sitting on a substrate. Calculations identical to those described above were carried out

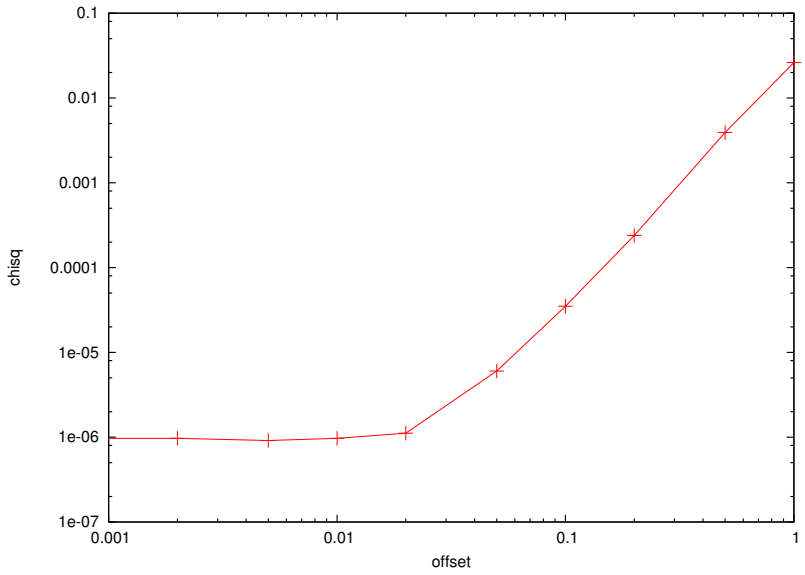

Figure 3.3: Error metric of fits versus misalignment of simulated diffraction patterns using ER.

on a sphere of radius 15 truncated by a plane 10 pixels away from the center of a sphere. The plane is oriented parallel to the y axis, and forming 45° to both the x and z axes. To determine how well the phase retrieval algorithm reproduces the original simulated crystal shape, a fidelity ξ_0^1 is defined as,

$$\xi_0^1 = \frac{\sum_{i=1}^{N} |\rho_0(i)|^2 - |\rho_1(i)|^2}{\sum_{i=1}^{N} |\rho_0(i)|^2}, \tag{3.57}$$

where the known crystal shape is $\rho_0(i)$ and the shape returned by the fitting algorithm is $\rho_1(i)$. ξ_0^1=0 denotes perfect agreement between the known shape in a simulation and the recovered shape.

As shown in the fidelity numbers below, 2D fits to data simulated using a real space gradient differ from the simulated real space shape. This applies equally well to fitting in which the phase was allowed to vary, denoted ER(so) for Error Reduction with support only, and standard ER. However, the error metric does not increase with offsets up to two slices when the fitting procedure allows a real space phase, meaning that the algorithm was able to find a solution to the constraints, but not the correct solution. This is indicated in the constantly increasing fidelity with increasing offset.

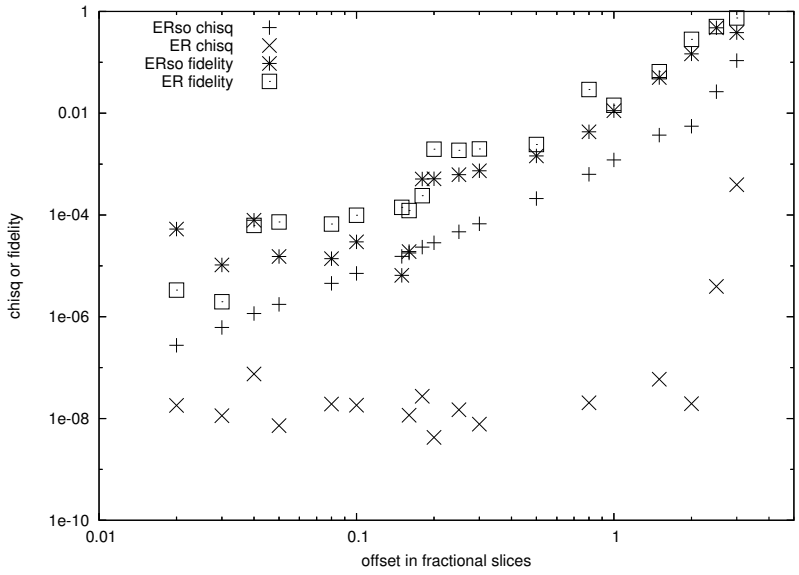

Figure 3.4: Error metric (χ^2) and fidelity (ξ_0^1) of fits to simulated patterns from a truncated sphere using the standard Error Reduction algorithm or Error Reduction with support only.

Chapter 4

Experiment

4.1 Equipment

Experiments to measure coherent X-ray diffraction patterns from equilibrium crystal shapes of Pb were carried out at the CXD experimental station of the Sector 34 insertion device beamline (34-ID)of the Advanced Photon Source at Argonne National Laboratory. Section 4.1.1 will give an introduction to insertion device beamlines at synchrotron light sources and describe some of the important components of the 34-ID beamline at the APS. Sections 4.1.2 through 4.1.4 describe the equipment used in these experiments.

4.1.1 X-ray Source

Experiments were performed in the CXD hutch at Sector 34 ID at the Advanced Photon Source (APS) at Argonne National Laboratory. The APS is a synchrotron which operates with a current of 100mA e^- at an energy of 7GeV. Sector 34 ID uses X-rays produced by an APS undulator A[1]. The beam entering Sector 34 is split by a liquid nitrogen cooled mirror so that two end stations can operate simultaneously. The mirror has the effect of filtering out higher harmonics in the X-ray beam produced by the undulator. This is referred to as a 'pink' beam, as opposed to the original 'white' beam. The X-rays used in the CXD hutch pass through a double crystal Si monochromator, which selects out a narrow frequency range.

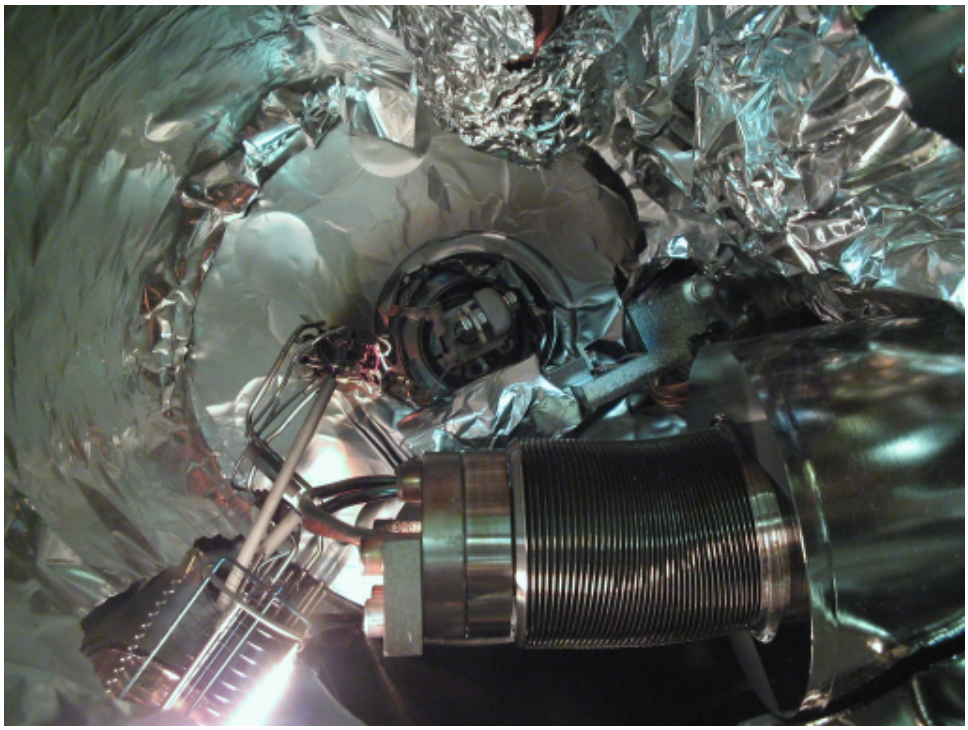

Figure 4.1: Downward view from inside vacuum chamber. The sample is in the middle, the bellows rotating the vertical slits are near the bottom of the image. A quartz effusion cell protrudes far into the chamber, close to the sample. An ion gauge filament is visible at the lower left corner.

4.1.2 Chamber

The CXD hutch on 34-ID contains a cylindrical ultra-high vacuum (UHV) chamber 8" in diameter with the cylindrical axis in the vertical direction. A gate valve can be used to isolate the chamber from the incoming X-ray flight path when the chamber is opened to atmosphere.

When the gate valve is open the chamber is pumped by a 400 l/s ion pump surrounding the flightpath just upstream of the chamber through a 6" pipe. For pump-out, the chamber can be connected through an all-metal valve to a turbopump. The sample mounts on a flange that passes the external rotations inside the chamber. A pair of rotatable seals are separated by a space pumped on by a turbopump, so that leakage through one seal during rotation should not effect the pressure in the chamber. An ion gauge is used to monitor the pressure in the chamber.

While the X-ray beam enters the chamber from the UHV flight path, it

exits though a Be window which covers one quarter of the circumference of the chamber. This window is one of the more sensitive components of the beamline, since Be is brittle and toxic, and great care must be taken to avoid touching the window while working on the chamber. Be is used because of its low atomic number (Z=4) makes it a very weak scatterer. A shield can be placed over the window when one is working on the chamber to avoid accidental contact. If the detector flight path (described in Section 4.1.3) is placed close enough to the chamber a suitable upper limit must be placed on the upwards motion of the detector arm to prevent a collision while moving the diffractometer angles.

An additional precaution must be taken to prevent damage to the Be window where the direct beam exits the chamber. When using pink beam, the direct beam produces enough ozone to rapidly damage a Be window through which it passes into air, causing visible damage in a period of days. Although the monochromatic beam has considerably less flux, it is still wise to prevent the case of the direct beam passing through the window into air. This is accomplished by a small nozzle (1cm diameter) with dense foam which is pressed against the Be window on one side and a Kapton window on the other side. A constant He flow through the nozzle prevents the creation of ozone near the Be window. This He flow is monitored and connected to an interlock which forces the X-ray shutter before the CXD hutch to be in the closed state. Damage to the Kapton on the nozzle is easily repaired by removing the Kapton and fastening new sheet using epoxy. The only inconvenience of this arrangement is ensuring that there is sufficient He flow and that the He tank will not run out during a long ($\sim$10hr) scan.

The illumination of a sample in the chamber is controlled by a pair of roller blade slits. Each slit is a pair of polished Mo rollers, ground from 3/8" rods and separated by 200μm shims, shown schematically in Figs. 4.2 and 4.3. These shims determine the maximum aperture produced by the slits. This aperture is closed by rotating the slits about the axis exactly half-way between the axis of each cylinder. This is achieved by careful construction of a bracket to hold the cylinders which is connected to a rotatable, tapped flange which is connected to a bellows which protrudes into the vacuum system. On the air side of the flange is an arm which pivots about a flexpivot, positioned inside the bellows, with an axis of rotation the same as the line halfway between the axes of the roller blades. The bottom of the arm is pushed on

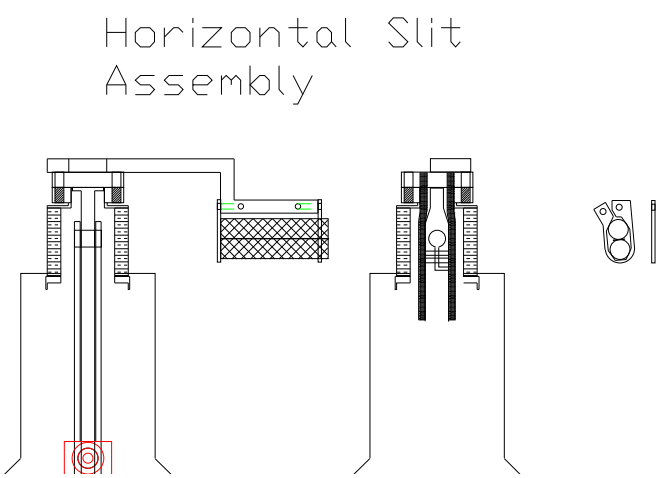

Figure 4.2: Horizontal slit assembly, showing a tube protruding into the vacuum chamber, bellows, the slit manipulator arm and the roller blade slits. To the right is shown the bracket which holds the rollers.

by a motorized micrometer perpendicular to the arm to control the rotation of the slits. This whole assembly is pulled inward by vacuum loading (17lb) and pulled outward by another motorized micrometer and a Pb weight. Both slits may be moved entirely out of the beam for alignment. The geometry dictates that for small slit openings, a 0.042mm movement of the micrometer controlling the horizontal gap changes the horizontal aperture changes by 1μm. Similarly, a 0.028mm movement on the micrometer controlling the vertical gap changes the vertical aperture by 1μm. The zeroes of the gaps must be recalibrated at the beginning of each experiment.

A quartz effusion cell was installed in the chamber for Pb deposition. This was a simple 'T' shaped cell composed of cylindrical segments with 1cm inner diameter. 99.995% pure Pb pellets were inserted into one of the cross pieces of the 'T'. A thermocouple (type K, chromel-alumel) was inserted into the long portion of the 'T'. A Ta wire was wrapped around the entire cell for heating purposes. Because of the position of the vertical slits and because of the desire to place the cell near the sample due to the lack of columation, a stiff metal arm had to extend in from a flange on the chamber and make two right angles to properly locate the cell. This arrangement required spot welded connections on the heater arm while it was in the vacuum chamber. Refilling the effusion cell was carried out in between experiments by removing the top flange on the chamber and using a pair of drinking straws taped together to

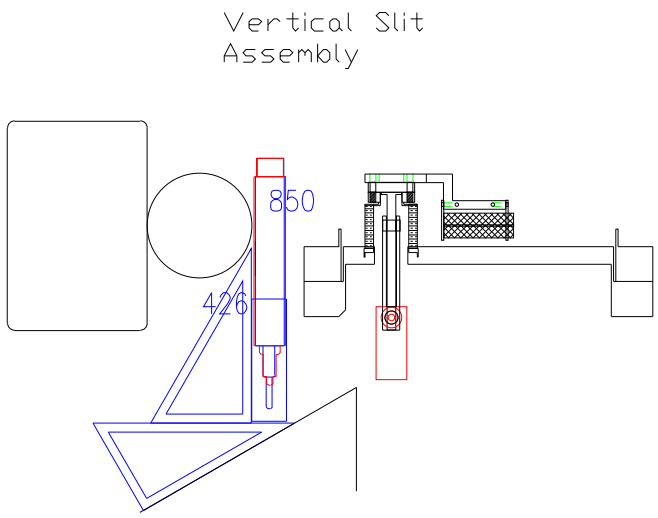

Figure 4.3: Vertical slit assembly, showing bellows connected to the base flange of the chamber. To the left are the flightpath for the X-ray beam which passes through the CXD chamber and a support for the flightpath.

feed pellets into the cell.

4.1.3 Diffractometer

A very large Newport diffractometer is used to control the scattering geometry of the experiment. The size is necessary for two reasons– the motors which manipulate the sample must be able to endure 31lb of vacuum loading and the detector arm must be able to support a 15lb camera at 2.5m from the axis of the arm. In the configuration used for our experiment there were six angles on the diffractometer, although only three were used in lining up on diffraction pattern or taking 3D images. The remainder were used for alignment or not at all. Figs. 4.4 and 4.5 show the important diffractometer angles, as well as the directions on the detector.

The θ axis, shown near the bottom of Fig. 4.6, is always vertical and defines the center of the sample. Physically it is a turntable with precision (double) bearings to minimize wobble. It has a continuous range of motion and can support the required vacuum load. It is the motion of this motor which is transmitted through the differentially pumped seal. The θ motion is highly reproducible once a sizable ($> 1°$) backlash is taken into account. This is the motor which was scanned to acquire a full 3D diffraction pattern,

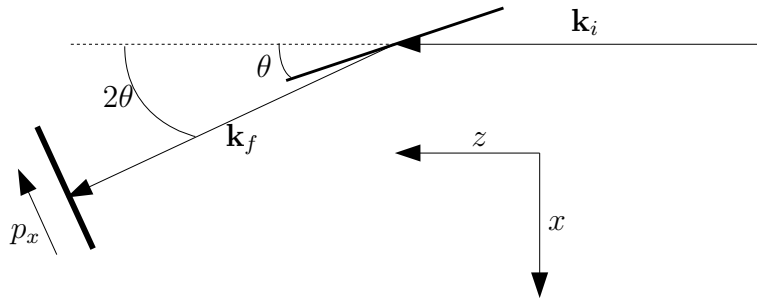

Figure 4.4: Schematic of the top view of the diffractometer in the CXD hutch of APS 34-ID.

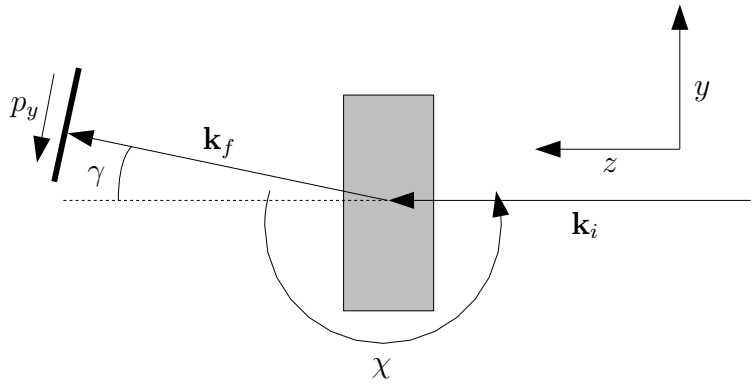

Figure 4.5: Schematic of the side view of the diffractometer in the CXD hutch of APS 34-ID.

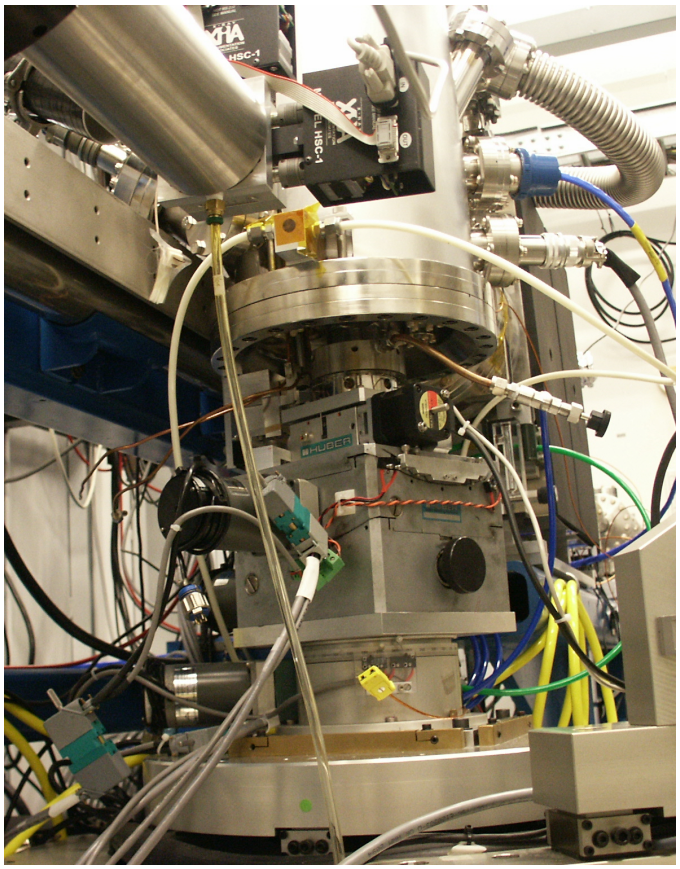

Figure 4.6: View from below the vacuum chamber, showing the 2θ, χ, ϕ, and z rotation/translation stages. The nozzle which protects the Be window from ozone is also visible.

as explained in Section 4.2.5.

Mounted on top of the θ motor are two perpendicular arcs, the boxy portion of the stack of motors in Fig. 4.6. χ rotates the sample about its surface normal. ϕ tilts the sample so that at $\theta = 0°$ the top of the sample moves in the positive x direction and the bottom moves in the $-x$ direction. χ has a range of motion of $\pm 10°$. The range of ϕ is $\pm 20°$. Their motion is permitted by a bellows protruding downward through the bottom flange of the chamber. The sample mount which connects through these bellows is shown in Fig. 4.8b. ϕ was used to assure that the sample was mounted straight, afterwards it was not used. χ was not used in this experiment.

The movement of the detector arm is controlled by two Newport motors 2θ and γ, as shown in Fig. 4.7. The axis of 2θ is always vertical. The zero position of 2θ and γ is the forward direction (no scattering). Increasing 2θ

moves the detector away from the ring, in the 'outboard' direction. θ and 2θ are independent motions, but which γ=0, the condition $2\theta = 2 \times \theta$ defines the specular reflection geometry. Increasing γ moves the detector upward on an arc in a plane perpendicular to the horizontal plane. This plane differs from the vertical plane containing the straight through beam by 2θ.

The actual detector arm is slightly less than 2m in length. It is designed to hold various lengths of flight path which are chosen for an individual experiment based on the desired resolution and field of view. A platform can be mounted after or between sections of flight path to hold either a scintillating detector or a CCD. The detector arm has two circular clamps holding the flight path leaving three ranges of detector positions, before the first clamp (0.3m-.5m), between the clamps (1.0m-1.3m), and beyond the clamps (2.0m-2.5m). The ranges here are approximate. The experiment described in this chapter were carried out with the detector 1.36m from the sample.

Because of the weight of the detector arm and detector, counterweights are necessary to protect the motors and allow proper operation. A large, permanent Pb counterweight hangs off the opposite side of the γ axis from the detector arm. Smaller weights (2.5kg and 5.0kg) can be positioned along a rail on top of the detector arm. These allow the arm to be 'tuned'. If there is insufficient weight (torque) on the detector arm it will bounce up and down while being raised. Too much weight on the arm results in bouncing when it is lowered.

A flaw in the control system can cause improper behavior in the 2θ motor. While conducting commissioning experiments on the beamline designed to study X-ray photon correlation spectroscopy, a periodic, discontinuous motion of a speckle pattern was observed. The pattern remained stationary for 45s, quickly moved 2 pixels on the detector at 1m, remained stationary for 15s, and then moved back. An autocollimator was used to check that the motion could be attributed to the movement of the detector arm. It appears that the controller, which continually monitors the position of the detector arm, integrates the error over time, and when the error is over a certain value it moves the arm in the opposite direction as the error. Since it can only move in finite steps there is an error associated with the new position, after some time it returns to the first position. The solution seems to be switching the motor off when not in use, which can be accomplished through the

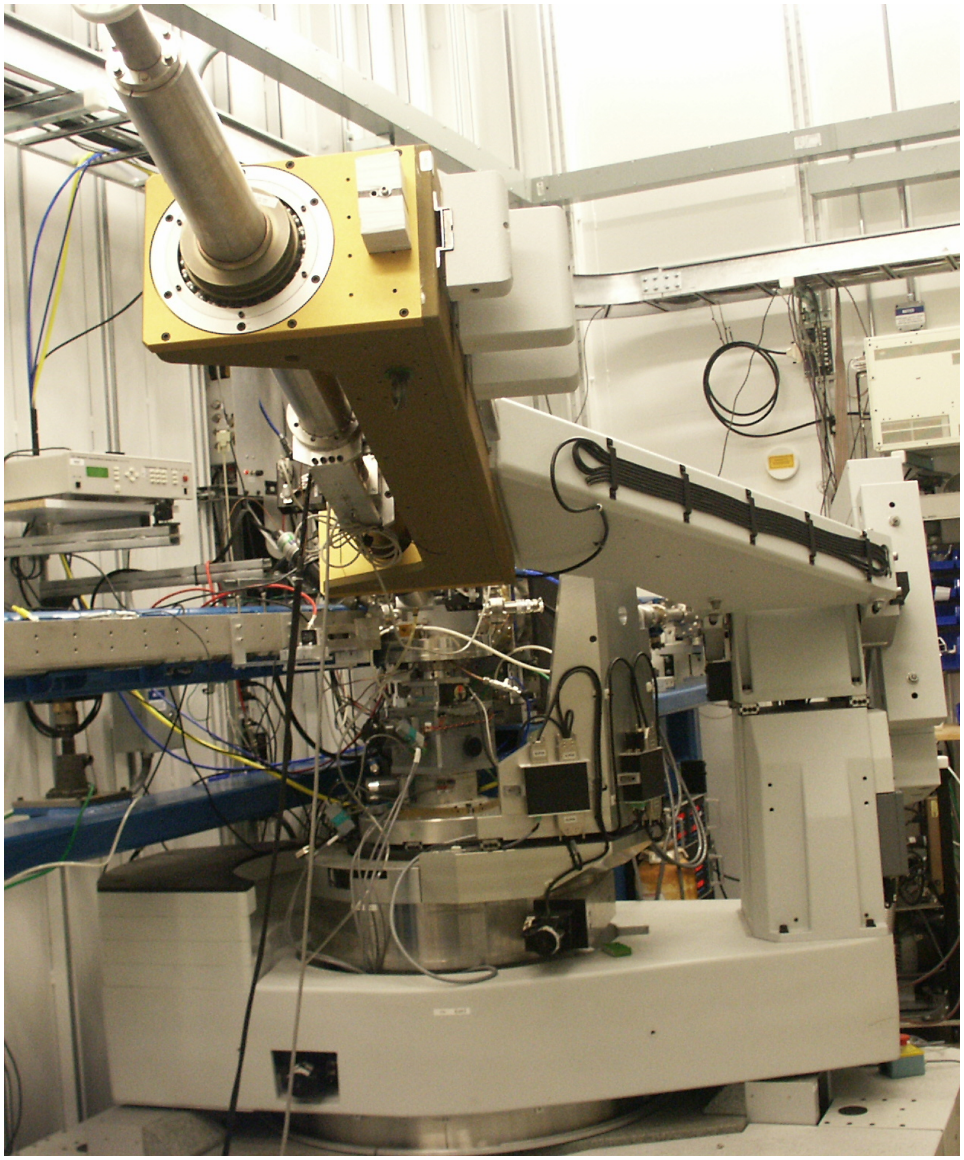

Figure 4.7: The diffractometer arm, at a small 2θ angle and large γ angle. A scintillating detector is on the platform in the central portion of the arm. To the left of the diffractometer is a support and flightpath for an X-ray off which our beam is split. This arrangement allows two experiments to be conducted in tandem.

computer interface to the diffractometer controller.

The only other diffractometer motion used throughout the experiment was the 'z' motor, in the very middle of Fig. 4.6, unfortunately named since it is a vertical translation and the coordinate convention is that x is outboard, y is upward, and z is downstream, as indicated in .Figs 4.4 and 4.5. This motion could be used to study different portions of the sample, which was mounted vertically.

The diffractometer also contains a ν motor, which rotates the flightpath along its cylindrical axis. This motion was not used in our experiment. Additionally, slits can be mounted on the detector arm, both at the beginning of the arm and immediately before the camera. Because of the diffraction geometry of this experiment the detector was never positioned near the direct beam, making these slits unnecessary. The detector slits obstruct use of portions of the CCD, so they were removed for this experiment.

The chamber permits the mounting of samples either vertically or horizontally. The sample must be mounted on a holder which connects to a stainless steel rod, which is bolted onto a specialized 2.75" diameter flange with a tapped inner face and six feedthroughs which are brazed into the piece, as seen in Fig 4.8b. In our case two of these feedthroughs are connected to a boron nitride heater. The other two are connected thermocouple wires, which can barely been seen connected to a clip near the bottom of the sample in Fig. 4.8a. The mounting of the sample in our experiment is described in Section 4.2.1.

4.1.4 CCD

A Roper Scientific 1340×1300 pixel direct read charge coupled device (CCD) camera was mounted on the detector arm to record high resolution CCD patterns. This camera features $20\mu\text{m} \times 20\mu\text{m}$ pixels. The camera's efficiency is best over the range of 5keV to 9keV. The CCD interface is 1MHz line drivers, which are read out to a PC through a "TAXI" interface card. A program provided by Roper Scientific called WinView is used to control the camera and store data in a format called SPE, the format for which is made public allowing the data to be handled by user developed programs. The CCD chip is cooled by a Peltier thermoelectric cooler which is in turn cooled by a flow of chilled water. This produces a chip temperature of -50°C, which

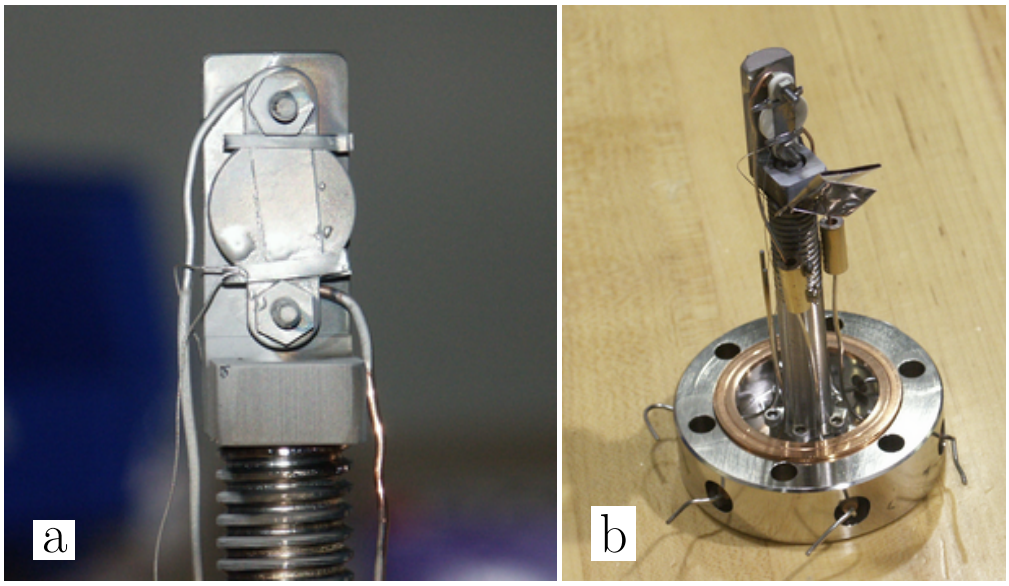

Figure 4.8: The sample and mounting. a) shows a sample after mounted to a boron nitride heater, supported by a ceramic block. b) shows the whole mounting assembly, including a shield (bent down) to partially collimate the Pb.

suppresses the background signal. Aspects of the background signal from the CCD are discussed in Section 4.3.2.

4.2 Measurement

4.2.1 Sample Preparation

Two choices of substrate were used in experiments to measure equilibrium shapes of Pb. Graphite was chosen because Pb is known to a low wetting angle with graphite and because the system was studied in the experiments of Heyraud and Métois[29, 31, 30]. Silicon with native oxide intact was chosen because it is an amorphous surface and therefore can not cause and epitaxial film. In order to study equilibrium shapes it is necessary to minimize interaction with the substrate which may lead to strain and distortion of the shape.

The substrate needed to be cut to approximately 1cm by 4cm. The pyrolitic graphite sample was cut by repeated scoring with a clean razor blade. A silicon wafer with {111} orientation was cut by scoring once with a

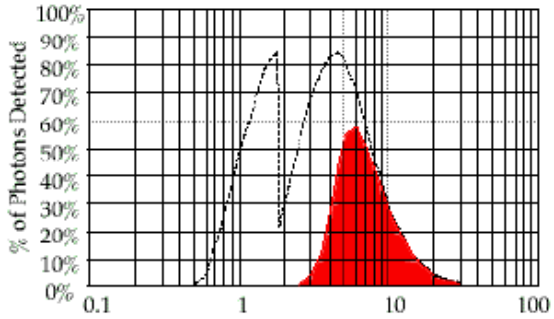

Figure 4.9: CCD efficiency versus energy with (shaded area) and without (dotted) a Be window[2]. The CCD at the 34-ID CXD hutch has a Be window.

diamond scribe and breaking. The silicon was then rinsed in methanol. The graphite samples were not rinsed since there was concern of liquid becoming trapped between the layers of the graphite.

The substrate was then placed on a boron nitride heater and partially fastened by a pair of Ta clips bent over the substrate and around a heater. A type K thermocouple connection was then spot welded on one of the clips. The heater, which has holes at either end, was fed over a pair of threaded rods with are fixed to a machinable ceramic block. This assembly is shown in Fig. 4.8. The order of pieces on the threaded rod is as follows: nut, ceramic block, nut, copper wire to power heater, washer, graphite washer, heater, bolt. The last bolt actually tightens against the Ta clip, which then presses down on the sample. Care must be taken not to overly tighten this nut since the heater is not perfectly flat, so too much pressure on either end can result in breaking the substrate. The graphite washer sits partially inside the back face of the heater, coming into electrical contact with a graphite surface which is a terminal of the heater. In preparation for one run, after overtightening the nut and breaking the silicon substrate, the nut was undertightened, causing a connection between graphite washer and graphite heater terminal which was good at room temperature but failed at higher temperature. This case will be dealt with in Section 4.2.4.

In order to protect the vacuum chamber from contamination, the bottom surface and most of the vertical wall of the chamber was lined with aluminum foil. Great care was taken to protect the Be window from Pb, which would act as a scatterer and attenuator on the window. The vertical roller blade

Figure 4.10: Side view of sample mount, showing shield (folded), the back of the heater, the ceramic block, the thermocouple wires, and wires to power the heater.

slits were also wrapped in a sheet of aluminum foil.

4.2.2 Chamber Bakeout

In order to achieve UHV conditions the chamber was 'baked out' after exposure to atmosphere during sample insertion. After closing the chamber and tightening all bolts holding flanges on the chamber, it is pumped by a scroll in-line with a turbopump. After the pressure in the chamber has dropped to 10^{-2}Torr the turbopump is started. During this time heater tapes are wrapped around the base flange, top flange, and portions of the chamber wall away from the Be window, which is covered by a steel shield. The chamber is then wrapped in aluminum foil for insulation. If the pressure has continued to drop steadily power to the heater tapes can be set to 50% on variac variable transformers. Once the pressure is in the range of 10^{-5}Torr the gate valve to the ion pump can be opened and the valve to the turbopump closed. Within a few minutes the pressure drops to the range of 10^{-7}Torr. The variacs can then be set to full power, watching that the pressure does not increase above 10^{-6}Torr. This power leads to a maximum chamber temperature of 75°C, as measure by a thermocouple mounted on

the base flange and read by a Love thermocouple reader. The bakeout should continue for $>$ 24 hours. For the run during October of 2003 the chamber was baked out for two days. All subsequent descriptions of the experiment, unless otherwise noted, will deal with this experimental run.

Before the chamber bakeout is ended the Si sample and effusion cell were outgassed. 9.2V×2.8A passed to the effusion cell during bakeout led to an effusion cell temperature of 197°C. 5.84V×0.4A passed to the sample heater during bakeout led to a sample temperature of 254°C. After bakeout a base pressure of 3.4×10^{-9}Torr was achieved.

4.2.3 Alignment

The undulator and monochromator were set to 9.0keV. The undulator and diffractometer are controlled through graphical interfaces or **super**[22] diffractometer control software which interfaces with EPICS[3], a control system developed by the Advanced Photon Source. The monochromator and slits were controlled through a separate computer running the diffractometer control software **super**[22]. Flux in the chamber was maximized by peaking up EN, a pseudomotor in the **super** which controls the energy selected by the monochromator, and TWE and $CH2$, which control the relative angles of the monochromator crystals. The peak was found to be at EN=8.925(keV), consistent with the typical result that the peak energy of an undulator is 50-100eV below the ideal peak energy due to imperfections in the undulator. The wavelength is therefore taken to be $\lambda = hc/(8925eV \times e) = 1.39^{-10}m =$ 1.39Å.

The θ angle was lined up using a specular diffraction peak from the Si(111) measured in a scintillating detector. Si has diamond structure with a lattice spacing of 5.43Å, meaning that it has $\{111\}$ planes with a spacing of $d_{\{111\}} = 5.43\text{Å}/\sqrt{3}$=3.14[9]. According to Bragg's Law[62, 9], the specular (111) Bragg peak should be at $2\theta = 2 \times \theta$ and

$$2\sin\theta = \frac{\lambda}{d_{\{111\}}}, \tag{4.1}$$

or $\theta = 12.7°$. The measured value of $\theta = 12.5°$ was off by 0.2°, which was used as an offset to correct θ.

4.2.4 Deposition

Because of the shape of the shield and the location of the effusion cell it was not possible to measure diffraction from the sample during deposition. Additionally, the sample had to be raised 70mm using the 'z' translation stage. The power to the effusion cell was increased in stages over a six minute period to 18.25V×4.5A, at which time the chamber pressure was 1.1×10^{-8}Torr, the heating cell temperature was 300°C, and the sample temperature was 118°C, as discussed below. After five minutes the effusion cell peaked at 339°C, the pressure and sample temperature climbed steadily. 27 minutes after the final power was set the pressure was 1.7×10^{-8}Torr, the heating cell temperature was 313°C,and the sample temperature was 168°C.

The heating of the sample during deposition was due to radiative heating of the sample from the heating wire around the effusion cell. In previous runs using a graphite substrate and no shield we found that the sample was heated by the effusion cell to 248°C during deposition. It is possible that the temperature measured by the thermocouple on the clip was considerably lower than the actual temperature of the surface. This is suggested by the fact that weak scattering from Pb on the surface was measured during deposition, but disappeared as soon as deposition stopped. The scattering was at the correct location for liquid Pb or the {111} powder ring. The disappearance after deposition ended suggests that the temperature on the surface of the sample was high enough that the Pb was constantly being deposited on and was evaporating from the surface. This result led us to install the shield and switch to a Si(111) wafer with native oxide.

Sample heating was carried out by passing current directly though the Si wafer, even though it was mounted on a boron nitride heater. During our first attempt at heating using a power supply set to constant voltage mode, the current spontaneously dropped from 0.3A to 0.01A. After two hours of running 19.5V×0.02A through the heater, the sample temperature was 99°. After switching off the power to the heater, a digital multimeter read 2kΩ across the feedthoughs on the chamber which were connected to the the heater. After the sample and heater cooled off the resistance was measured as 260Ω. During the previous run of the experiment in July 2003 the resistance was 4Ω. After current the experiment it was determined that the nuts on the sample mount pressing one of the graphite washers into the heater were

not tightened sufficiently. This meant that the washer shifted upon heating, and after thermal expansion of the rod the electrical connection was broken.

By using a higher voltage power supply it was possible to heat the sample sufficiently that the Si conducted. This required ramping the voltage up to 25V, at which time the resistance fell and we were passing 1A at 5V. The first film prepared was melted quickly, at power of $6\text{V}\times 1A$ with a sample temperature, T_s between 264°and 335°C. Melting the original polycrystalline film causes it to break into individual droplets, which form single nanocrystals or microcrystals when they are frozen.

This sample produced extremely asymmetric diffraction patterns, indicative of large strain. There was likely too much Pb on the surface, because the effusion cell had been used to try to heat the sample before we were able to borrow a sufficiently high voltage power supply to carry out direct heating. An Oxford scintillating detector was placed on the detector arm to measure $\sim$ 1/200th of the powder ring. By heating the sample to T_s=450° using 1.5A of current the vacuum pressure rose to 6.8×10^{-8}Torr and immediately turning the heater power off we evaporated much of the Pb from the sample. The counts on the Oxford detector dropped from 410k/s to 48k/s. Putting the CCD back on the detector arm we saw a powder ring which was not evenly distributed. There appeared to be groups of grain that were physically near each other, as evidenced by numerous peaks in a single segment of the powder ring which appeared to be mutually coherently illuminated. While interesting, this sample preparation yielded patterns which appeared far to complicated to phase.

The first film was evaporated by heating the substrate, after which a new film was grown. After melting and resolidification of the Pb, highly symmetric diffraction patterns were observed. In switching from a short detector flight path which put the detector at 1.07m from the sample to a longer one which placed it at 1.36m the valve for the pumping on the rotatable seal was closed in the mistaken belief that it was connected to the same pump as the flightpath. With the differential pumping interrupted, the chamber pressure rose in a matter of minutes to 10^{-8}Torr. After the longer arm was installed and the differential pumping was resumed, the diffraction patterns appeared much weaker and had many fewer flares. It appears in a matter of half and hour the Pb partially oxidized leaving less pure Pb, which was surrounded by oxide and highly strained. The Pb was then evaporated

and a new film was grown.

This final deposition produced large enough grains that they were discernible in the powder pattern before melting the sample. The heater power was ramped up to 4.70V×0.76A, causing a sample temperature of T_s=289.6°C. Over four minutes the temperature climbed to T_s=289.9°C, where it remained constant for a minute. The heater power was increased to 4.71V×0.77A, which drove the temperature to T_s=290.1°C, where it appeared the sample was solid. A minute later the temperature was T_s=290.2°C and the sample was melted, as indicated by a drastic decrease in the intensity and increase in the width of the powder ring. This temperature reading was in contrast with the known melting point of bulk Pb, T_m=327.5°C. The melting point of 500nm particles is 0.15°below that of bulk Pb. The known melting temperature is therefore taken to be the high temperature calibration for the thermocouple. The thermocouple is then used to measure changes in temperature relative to the melting temperature. The sample temperature T_s in the remainder of the thesis will refer to the thermocouple reading, but will also be compared with the measured melting temperature.

After reducing the heater power and allowing the temperature to drop to 145°C to allow solidification of the droplets, the temperature was increased so that the sample could be studied near melting.

4.2.5 Measurement of Patterns

At T_s=289.0°=T_m-1.2°, the diffraction pattern from a single grain was measured at 2θ=5.49 and gmm=12.61. The roller blade slits were used to isolate the diffraction from an individual grain, which amounted to decreasing the illuminated area until no other grains with an orientation close to the grain of interest were illuminated. There settings were $hg \times vg = 1.00 \times 0.40 = 23\mu\text{m} \times 14\mu\text{m}$. The X-ray beam was incident on the sample at an angle of 12.61°, causing an elongation of the of the illuminated area in the horizontal direction. The footprint of the beam was therefore $105\mu\text{m} \times 14\mu\text{m}$. A series of 50 frames were recorded by synchronizing **super** which ran an 'mscan', or motor scan to scan θ with the camera control software. The **super** command was "mscan 1 th 13.47 0.01 50 -101," which scanned 1 motor, θ, starting at a position of 13.47°, in 0.01° steps, 50 steps, waiting 101 camera shutter pulses before changing frames. The conversion between a series of frames

measured at different θ angles and a pattern in Cartesian coordinates in reciprocal space is derived in Section 5.1. The camera acquired 50 frames, each 1.5 seconds and 101 accumulations. The short exposure was necessary to prevent saturation of the detector, which occurred below 18,000 ADU, or 60 photons, for a given pixel. At the end of the 10 hour scan the sample temperature was still T_s=2890.0°. This was scan was number 296, which will be referred to as Pb1003-296, and is shown in Fig 4.11

A diffraction pattern from a different grain was measured at the same temperature, T_s=289.0°=T_m-1.2°. The diffraction was much weaker, indicative of a smaller grain. It was more difficult to isolate diffraction by this grain, so the the slits were closed to $hg \times vg = 0.35 \times 0.30$, which produces and illuminated area of $36\mu\text{m} \times 11\mu\text{m}$. Closing the slits further produced changes in the diffraction pattern from the grain of interest, suggesting that we were at the limit of illuminating the grain with a uniform wavefield. This series of frames were measured over 60 steps of 0.01° in θ, starting at $\theta = 12.81°$. The camera acquired 60 frames, each 10 seconds and 48 accumulations. At the end of the scan the temperature was T_s=289.1°=T_m-1.1°. Scan number 307, or Pb1003-307, is shown in Fig. 4.12.

The heater power supply was turned down by 0.01V, and the temperature decreased to T_s=286.7°=T_m-3.5°. A 3D diffraction pattern from the same crystal as above in Pb1003-307 was measured at this new temperature, using the same slit settings. 40 frames were measured with a spacing of 0.008°. starting at θ=12.98°. The camera measured 40 frames. each 22 seconds and 37 accumulations. The scan Pb1003-310 is shown in Fig. 4.13.

4.2.6 Scanning Electron Microscopy

After an experimental run at the Advanced Photon Source, we brought the samples back to the University of Illinois and characterized the distribution of grains using a scanning electron microscope. SEM measurements were made at the Center for Microanalysis of Materials at the Frederick Seitz Materials Research Laboratory at the University of Illinois. They typically showed a distribution of grains, ranging in size from 100nm to 600nm. On some samples there were straight rows of much smaller grains, typically 10nm to 20nm running from one large grain to another. These may have been present on all samples, but were near the resolution limit of the microscope.

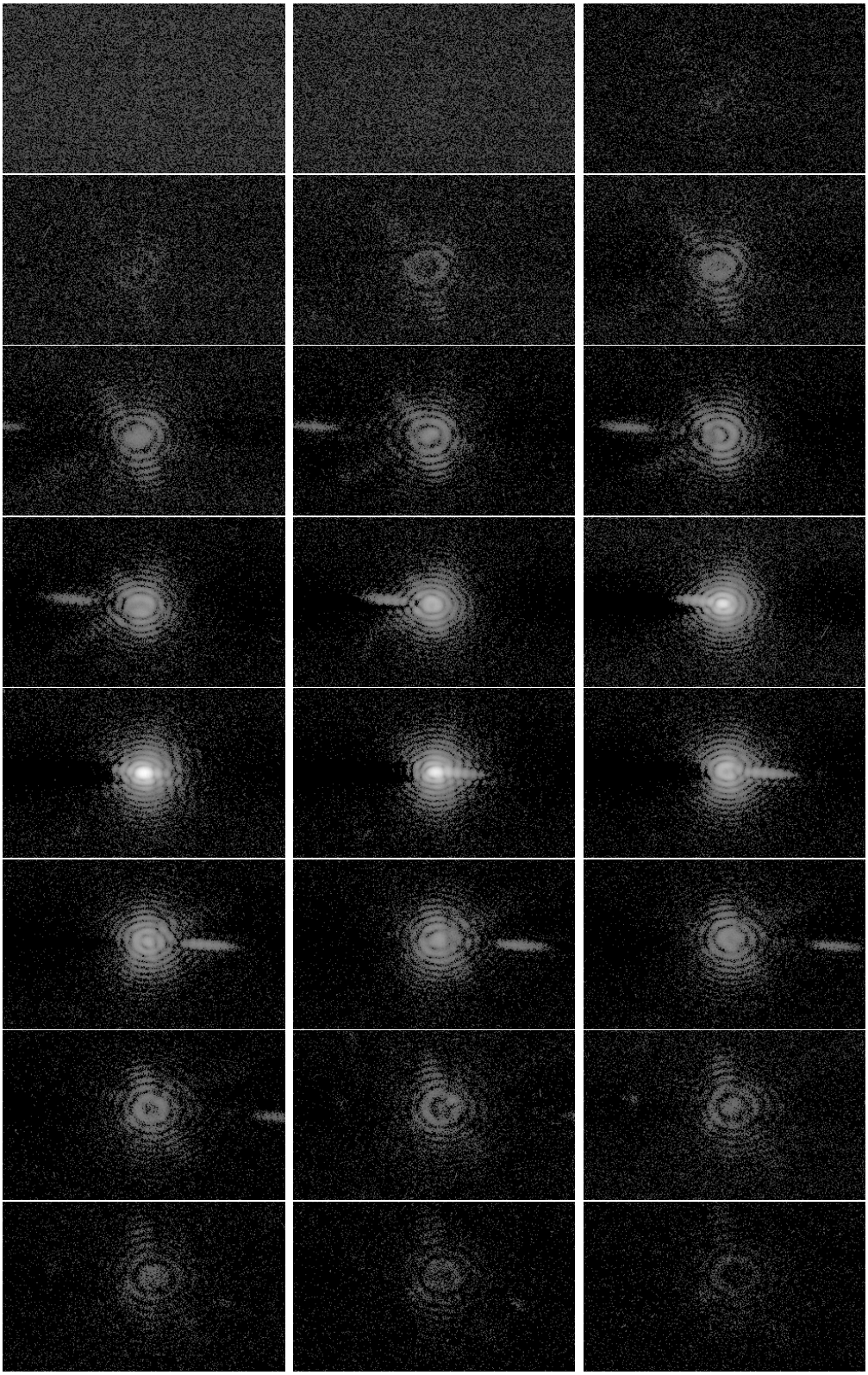

Figure 4.11: Every other frame Pb1003-296.

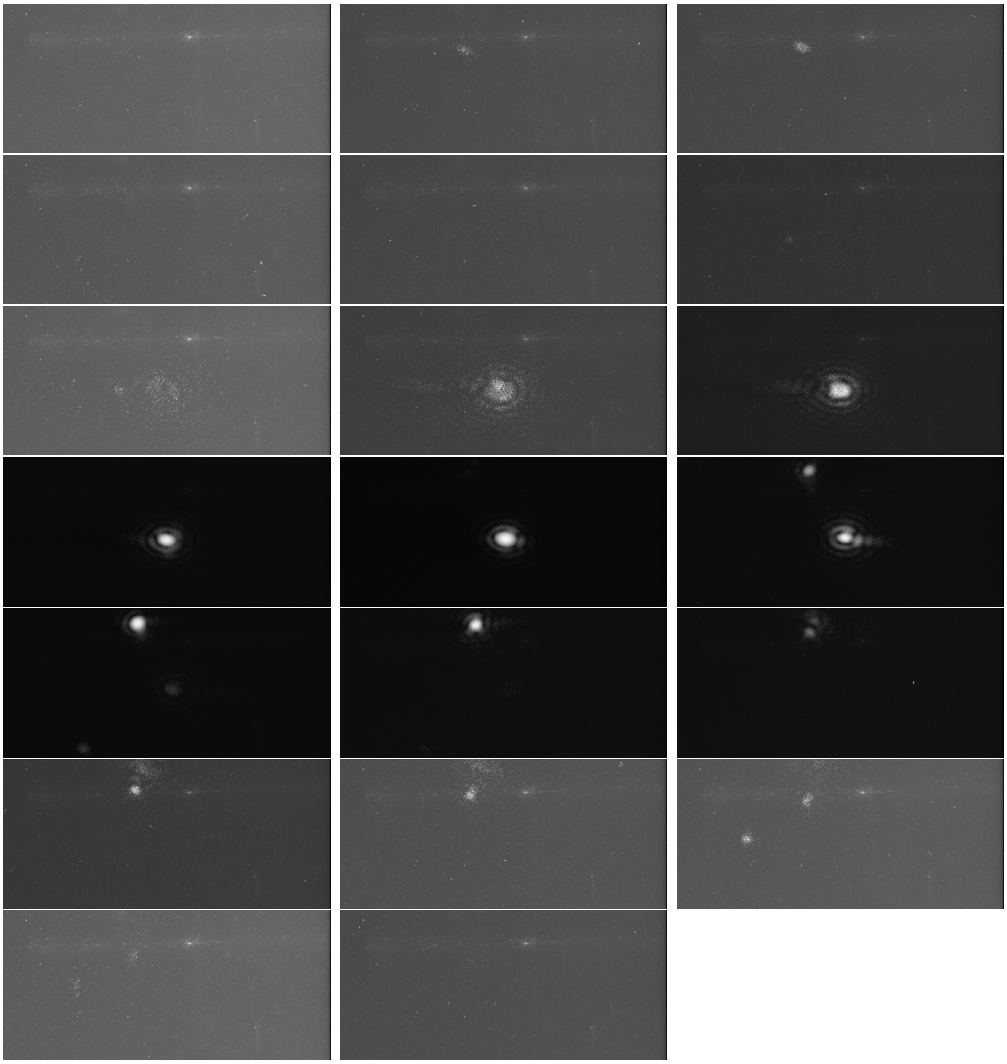

Figure 4.12: Every third frame Pb1003-307.

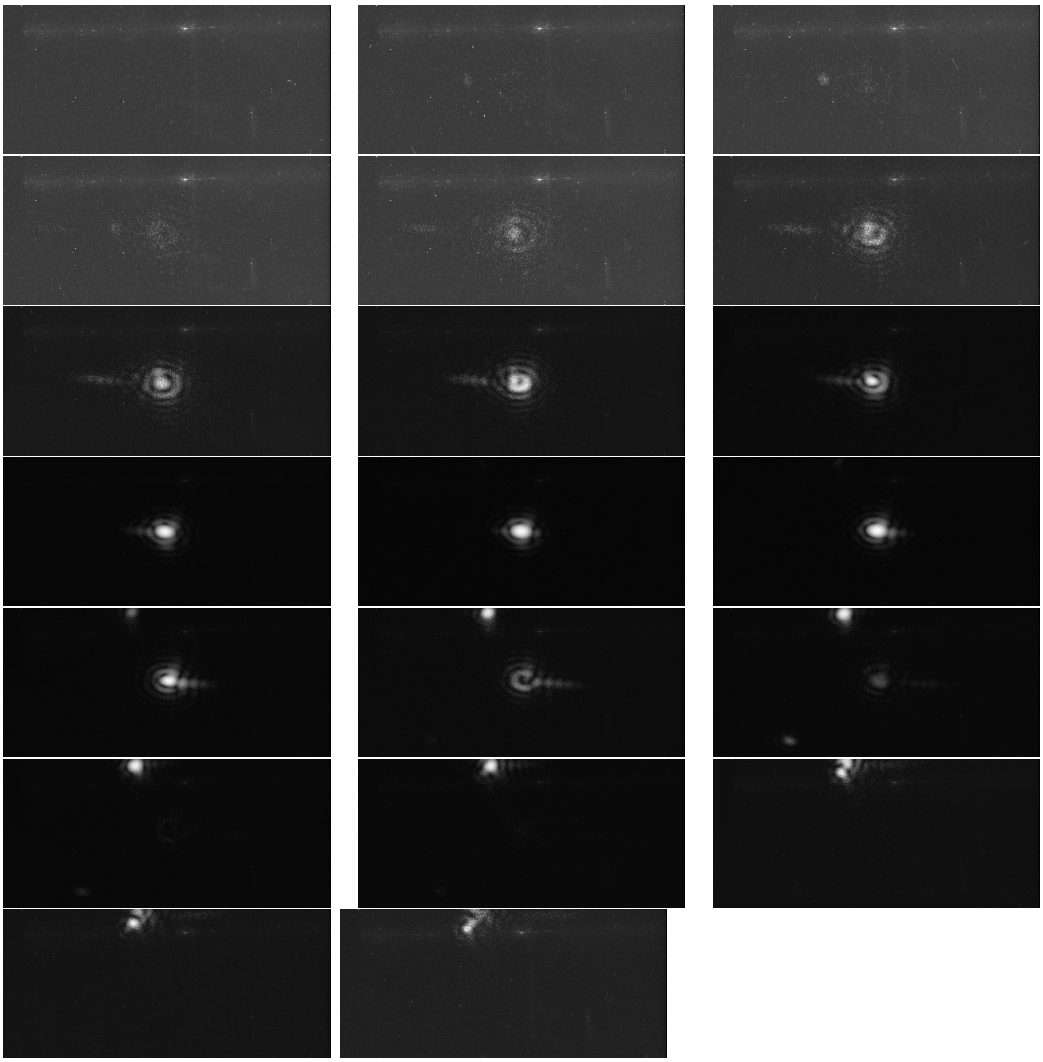

Figure 4.13: Every other frame Pb1003-310.

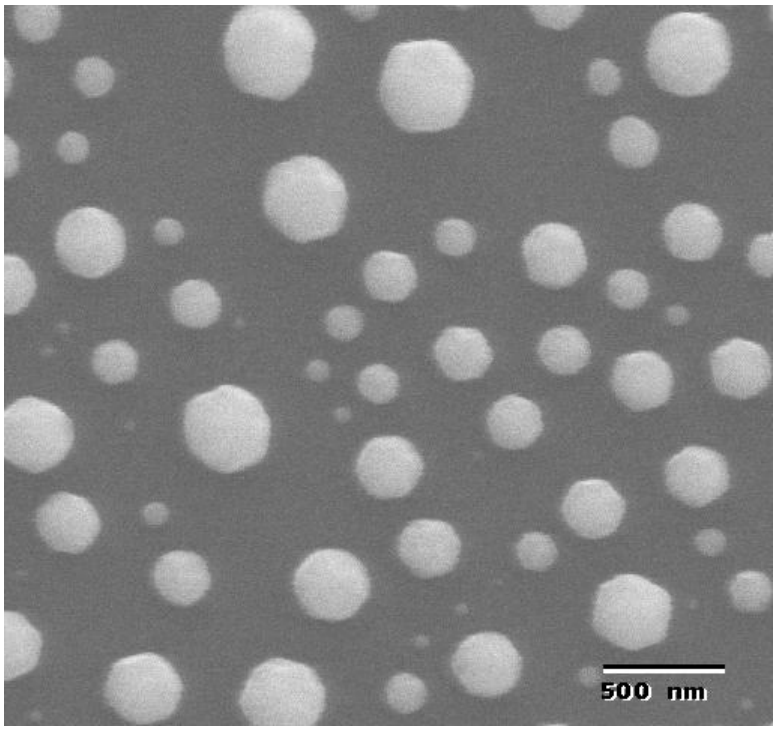

Figure 4.14: SEM of Pb sample measured at the Center for Microanalysis of Materials at the Frederick Seitz Materials Research Laboratory. A range of particle sizes are present, yet the shapes are fairly uniform.

4.3 Fitting Procedure

The process of fitting the phase of measured diffraction patterns requires numerous steps. Some of these are to address experimental issues such as artifacts associated with the detector, or contamination of the diffraction pattern with scattering from other grains. Others are more inherent to the fitting procedure and are necessary even with ideal data.

4.3.1 Format Conversion and Cropping

First, the data is converted from the long integer SPE format written out by Roper Scientific software into a double sp4 format used within the lab group using the program **3dspetosp4**. A three dimensional data set is then sliced into two dimensional files using **3dslice**.

The next step is to crop the diffraction pattern. This is done for two reasons; to center the diffraction pattern in the array and to remove artifacts along one edge of the array which arise from the handling of the data in the camera controller. If the slow analog to digital converter (ADC) of the controller was used, the first few rows of data have a lower background level than the rest of the data. If the fast ADC was used, the second row is the only one with a constant offset level; the rest have zero background. To find the center of the pattern I plotted as a ppm the logarithm of the intensity of the center few slices from the pattern using **logscale** and **2dplot**. There was usually one slice which was more nearly centrosymmetric than the rest– this was determined to be the center, as in **c** of Fig. 4.15.

The approximate in-plane center could then be read from an image manipulation program. Using the approximate center position and the size of array (known from calling **readheader**), the array can be cropped using **2dcrop**. Next, the cropped pattern is made into a complex array with **realtocomplex**, which copies the amplitude from a real array to the real part of the complex arrays and sets the imaginary part to zero. The data is then reordered to suit the FFT using **2dinvert** and then FFT'd using **dofft** to produce the autocorrelation function of the the center slice of the diffraction pattern. If the pattern was centered correctly, the phase of the autocorrelation function will be flat in the region with appreciable intensity. If it is misaligned, there will be a linear phase gradient, as seen in Fig. 4.16. A final decision about

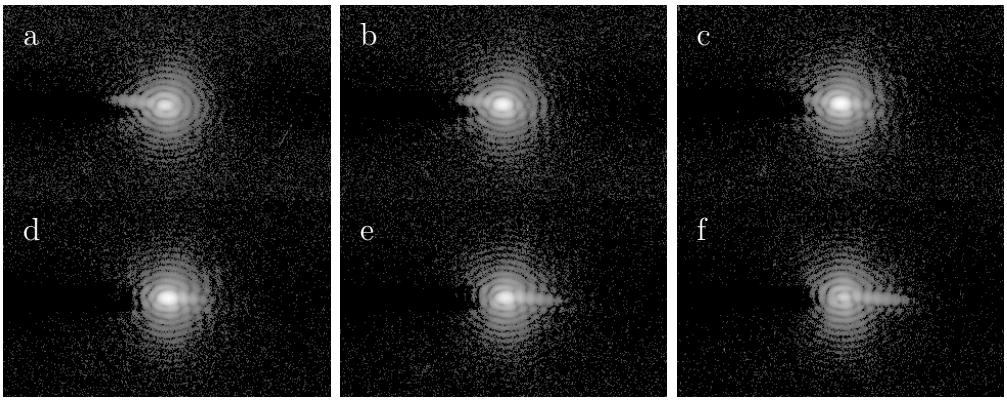

Figure 4.15: Center slices from 3D CXD pattern from Pb sample, on a log scale. Data file 296 from 10/03.

the cropping has to be made considering the center position, the location of defects, and the preferred dimension of the array. It may be useful to crop the array symmetrically in q_x and q_y so that the real space reconstruction has identical resolution in x and y.

4.3.2 Background Subtraction

When using the slow ADC, background subtraction was necessary. This could be accomplished in two ways. First, a separate background, if available, could be subtracted off using **flatten**. An appropriate background is a data file from the same region of interest on the chip and with the same time per accumulation, although not necessarily the same number of accumulations per frame. This method picks up any background features of the chip which might contaminate the data, but also frequently includes cosmic rays, which

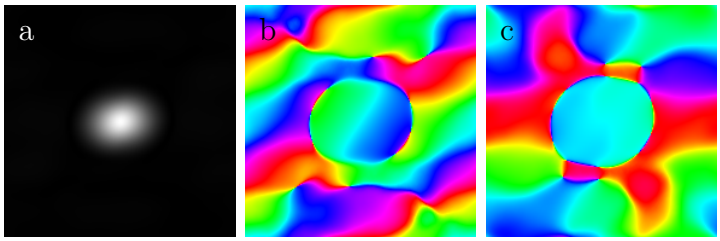

Figure 4.16: Amplitude (a) and phase of autocorrelation function obtained by Fourier transforming a diffraction pattern which is off center by 2 and 1 pixels in q_x and q_y (**b**), and properly centered (c).

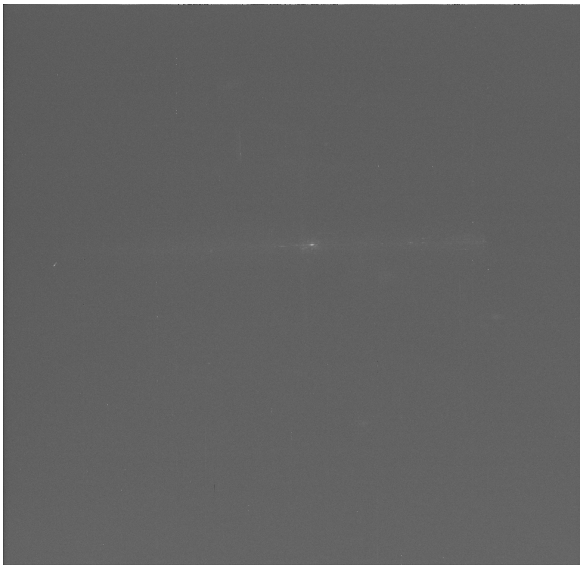

Figure 4.17: Detector background at -50°C. The horizontal streak is related to damage caused by saturation of the detector in a different experiment.

can be considered one time random defects in the data. Subtracting off such a background from the measured diffraction pattern yields artificially low counts for those pixels where the background contains cosmic rays.

A more reliable background involves the comparison of multiple frames with the program **makeback**. With this method a set of frames (typically four) is compared pixel-by-pixel. For each pixel, the minimum value is found, and the values from that pixel in different frames which vary from that pixel's minimum by less than a threshold value are averaged together. The threshold is typically set at half the number of counts produced by a single photon on the detector. In this way a 'clean' background can be obtained in the presence of cosmic rays. This method can even produce a background using a data set including a diffraction pattern, by using a few frames early and late in a 3D scan, assuming the scan extends far enough and diffraction patterns from other crystals do not appear in the same region of the array at both the beginning and end of a scan.

Background subtraction is not performed on data acquired with the fast ADC because the background in the data is zero. Although it seems ideal to have zero background, it is likely that there is a similar background voltage on pixels of the chip, but it is too low to be converted to a digital count by the fast ADC. This does not necessarily mean that the background can not

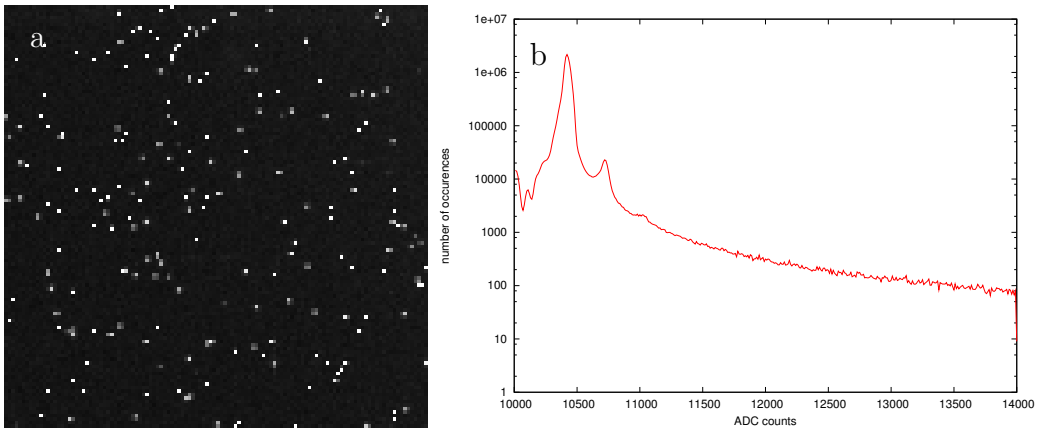

Figure 4.18: a) Example of individual photons contributing to counts in multiple pixels, taken from diffuse scattering from molten Pb. b) Histogram showing the number of times any pixel in the detector received a certain number of ADC counts during the course of 50 frames of a full CXD pattern. The background peak is at 10420, one photon peak at 10720, and two photon peak at 11030.

cause an offset in the number of counts read off from a single pixel when it is actually measuring a photon. Ideally this could all be avoided by if the data could be taken in a manner that the exact number of photons detected by a pixel could be known. A combination of two factors prevented this. First, there was a 'sharing' of charge between adjacent pixels, so that although a single photon typically produced ∼300 ADU's, those counts could be divided among as many as four pixels, as shown in (a) of Fig. 4.18. This means that if the number of counts is much over 300 above background it is difficult to say the exact number of photons causing those counts. Equivalently, (b) from Fig. 4.18 is a histogram of counts per photon, showing a strong background peak at 10420 and significant one photon peak at 10720, but the two photon peak is difficult to discern at 11030 over a background caused by this charge 'sharing' and the third peak is not distinguishable. Even if there were no pixels with more that three photons, there would be many pixels where it would be very difficult to tell whether there were two or three photons.

This problem could be avoided by acquiring an extremely large number of short accumulations for which even the brightest part of the pattern had only one or two photons per pixels [40]. This was precluded by the lifespan of the camera's shutter. The final run of this experiment was actually limited

by the operation of the shutter.

4.3.3 3D Array Setup

Once the data has been cropped and background corrected it is stacked to form a 3D array using **2dto3d**. The slices used must be chosen so that there are an even number (some programs for handling the data require all dimensions to be even) and if there are N_z slices the center slice of the pattern must be the $N_z/2+1$ slice in the new array. The next step is to reorder the array for the Fourier transform using **3dinvert**. This centers the array about the first pixel, so that if $N = N_x \times N_y \times N_z$, the $N/2+1$ pixel (the center pixel in the $N_z/2+1$ slice) is the first pixel in the reordered array. If we consider the diffraction pattern to be the power spectrum of the diffracting crystal, the center of the pattern is now the zero frequency component in the spectrum.

The measured pattern is the square modulus of the wave field which we wish to phase, thereby recovering the shape of the diffracting crystal. The square root of the diffraction pattern must therefore be taken using **dosqrt**, and the data file is then made into a complex array with **realtocomplex**.

4.3.4 Flagging

The final step to preparing the data before fitting is the most subjective. It was always difficult, if not impossible, to obtain a full 3D CXD pattern from a single grain without contamination caused by scattering from other grains. The goal when carrying out the experiment was then to limit contamination of the pattern to the edges of the array, far from the most important parts of the data. Portions of the pattern could then be flagged to indicate to the fitting program that the data values there are unknown. This flagging must be carried out by hand, meaning that a choice has to be made about what is good and bad data. The logarithm of the amplitude of each slice is plotted out using **logscale**, **3dslice**, and **2dplot**. Selecting the region to be flagged is done by opening an image in the graphics manipulation program GIMP[4], adding a "transparent layer" on top of the image, and drawing over the contaminated region using the "Draw in ink" tool. The new layer is then copied to a blank image and saved as a ppm format file, which can

then be converted to an sp4 with **2dppmtosp4**. Once this is carried out for each slice they can be stacked by **2dto3d** to form a 3D masking array. **2dflagmask** takes the data array and replaces the amplitude with the flag -1 in any point in which the mask array has a zero, leaving all other points unaffected. **3dmultifit2** treats any point in the reciprocal space input array with a negative amplitude as unknown.

4.3.5 Support Determination

The data that have just been prepared serves as the reciprocal space constraint in the fitting algorithm; a real space constraint must also be provided, as described in Section 3.2. There are two typical ways to make a suitable support. The first involves measuring the spacing of fringes in the q_x, q_y, and q_z directions. If the spacing in $q_x$is n_x and the extent of the array in q_x is N_x, the real space reconstruction should extend about N_x/n_x pixels. Once the approximate extent of the real space reconstruction is known, two dimensional slices of a support can be made using **2dpoly** and then stacked using **2dto3d**. The exact shape and size of the support is not critical because the support can be updated and improved by using the real space results from a fit.

3dmultifit2 requires a configuration file which specifies the input real and reciprocal space data files, and details the number of fits to perform, the number of cycles per fit, and the number of iterations, mode type, and parameters for that mode for each cycle. The mode numbers used for this project are listed in Table 3.1. The first three modes are standard algorithms described in Section 3.2.4. The last three were necessary to fit data sets where standard ER did not allow sufficient freedom. ER with finite support only (mode 18) sets the real space density to zero outside the supper but does not affect the portion of the array inside the support region. This differs from standard ER, which does not allow imaginary or negative densities. Modes 19 and 20 are used together, with alternating cycles of a small number ($\sim$20) of each. Mode 19 fixes the amplitude at what it had been at the end of the previous cycle, and allows the phase to vary, while mode 20 fixes the phase at the value that from the end of the previous cycle and allows the amplitude to vary.

4.3.6 Phasing Pb1003-296

Data set 296 from October 2003, to be subsequently referred to as Pb1003-296, was collected with detector angles of 2θ=25.49°, γ=12.61° and with θ between 13.47° and 13.96°. It is composed of 50 frames, each 101 accumulations of 1.5 seconds, resulting in an accumulation time of 151.5 seconds per frame. Including a 5.6 second transfer time per accumulation, the total acquisition time was approximately 10 hours. The original data set was $672 \times 436 \times 50$ pixels.

First the data was converted from SPE to SP4 format and sliced to 50 individual 672×436 arrays for handling and plotting using **2dspetosp4**. Next, the data was cropped to 656×436 pixels arrays by removing the last 16 columns of data using **2dcrop**. These data are artificially low because of the readout of the CCD. Next a background was composed of two slices from a multiframe background image taken immediately after the acquisition of Pb1003-296. Of 5 slices 1.5 seconds only two were not contaminated by stray photons. The preparation of this data set was completed before **makeback** was written.

The data was then cropped to 648×384 to center the array, as determined by examining the phase of the Fourier transform of the slice which contains the center of the diffraction pattern, in this case the 25th slice. The data was then binned to 324×192 to improve the speed of the FFT. Slices 1-48 were stacked using **2dto3d** to form a 3D array with slice 25 at the center, defined as the N/2+1 slice where N is the number of slices. After this the 3D array is inverted with **2dinvert** so that the center of the pattern is at the origin of the FFT. As stated earlier, this is necessary so that the real space image can be without a phase gradient. The square root was taken with **dosqrt** and the array was made complex using **realtocomplex**.

The autocorrelation function was approximately 70×64, so an initial support function of $42 \times 36 \times 24$ was used for fitting. This first fit using only one cycle or ER, gave and error metric of χ^2=0.046, as shown in Fig. 4.19. This resulted in a rounded shape with one sharp flat which was at the border of the support, as shown in Fig. 4.20. While the density varies greatly within the boundary of the shape, it does appear to be a distorted droplet shape truncated by the substrate on the right side. The distortion, due in part to irregularly shaped array in the Fourier transform, is dealt with in detail in

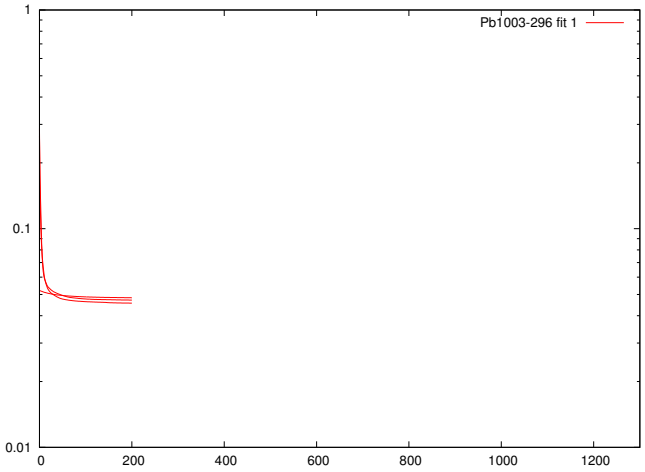

Figure 4.19: χ^2 error metric from initial fit to Pb1003-296.

Section 5.1.

Next, a fit was carried out with 100 iterations of ER with a support of $32 \times 24 \times 18$, much closer to the actual size of the particle than the initial support, and then continuing with a series of ER and mHIO with the initial support. This was done to force the reconstruction to be in the center of the support. This resulted in a nearly identical error metric χ^2=0.045, as shown in Fig. 4.21, and an image which seemed clearly mixed with its own dual, as shown in Fig. 4.22. Fit 3 was nearly identical with fit 2, with the difference being in a change of **3dmultifit2**. The fitting program attempted to align the phases of the real space fits, but introduced errors into the phase. Since a constant offset of the phase has no meaning, this portion of the program could be removed. This produced an error of χ^2=0.044 as shown in Fig. 4.23. While the error metric is the same, it is clear that the continuation of the fit after 80 iterations of ER with the tight support has a lower initial value than the same point in the fitting of fit 2. Fit 4 was also carried out in two stages. In this case unbinned data was used. First a fit was carried out using a $40 \times 26 \times 24$ support region. Next, a tight support was created using **3dslice**, **2dsp4tocon**, and **2dto3d**. The subsequent fit was carried out using ER and fHIO. The error metric was χ^2=0.037, as shown in Fig. 4.25, and the density and phase are shown in Fig. 4.24.

While fit 4 gave a reasonable idea of the crystal shape it clearly was unsuitable for quantitative analysis. The density inside the crystal varied

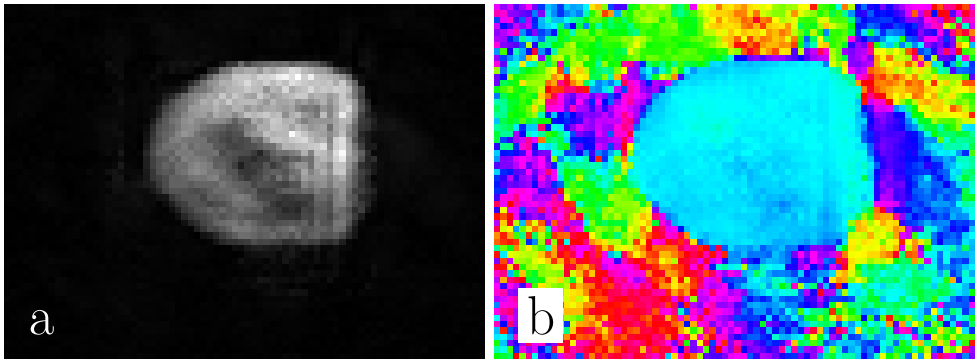

Figure 4.20: Central slice from 3D real space reconstruction from fit 1 of Pb1003-296. a) shows the density, b) shows the phase mapped on to a color wheel, where cyan, green, yellow, red, violet, blue, and cyan are separated by $\pi/3$.

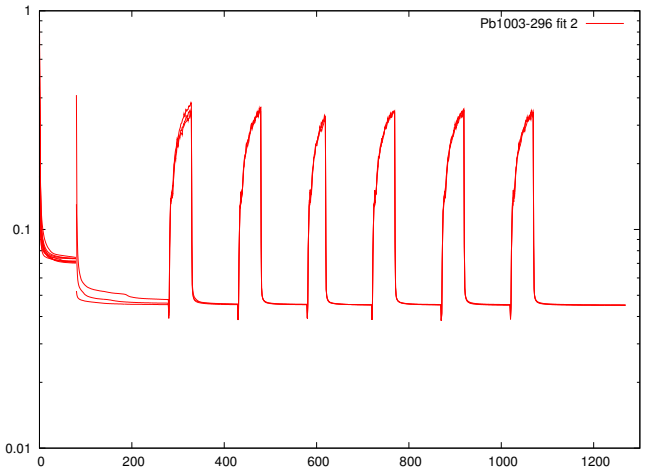

Figure 4.21: χ^2 error metric from second fit to Pb1003-296.

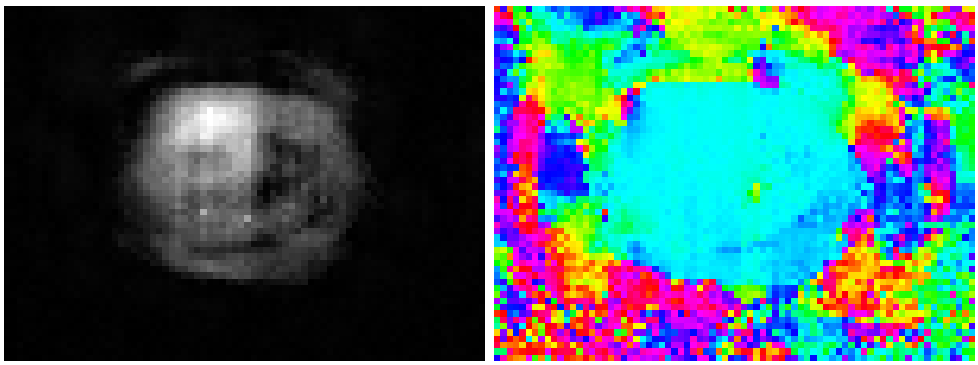

Figure 4.22: Real space reconstruction from fit 2 of Pb1003-296.

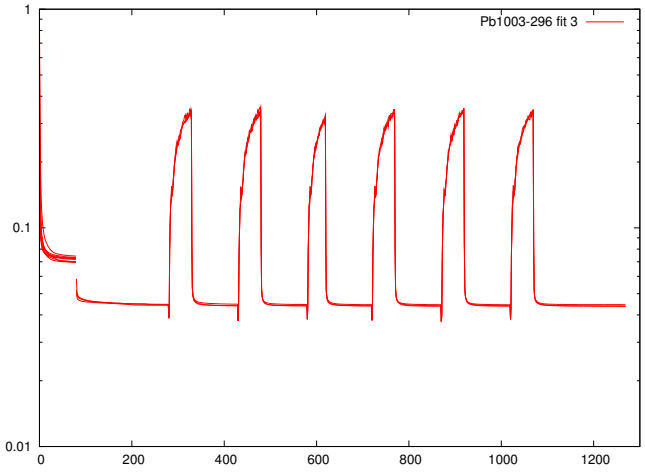

Figure 4.23: χ^2 error metric from third fit to Pb1003-296.

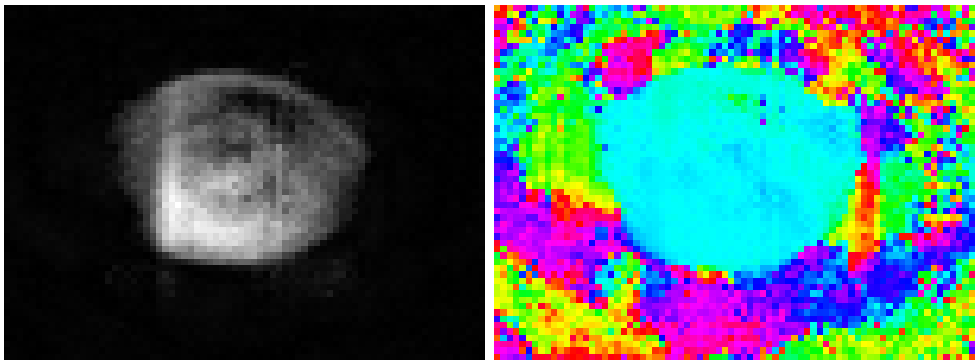

Figure 4.24: Real space reconstruction from fit 3 of Pb1003-296. The image appears to be the dual of Fig. 4.20 and is partially mixed with its own dual.

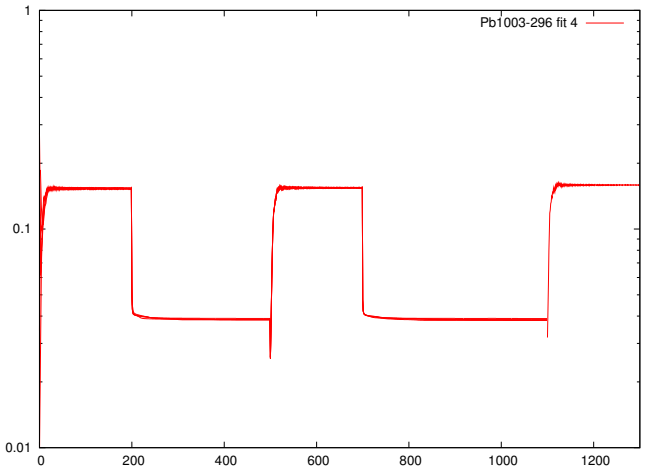

Figure 4.25: χ^2 error metric from fourth fit to Pb1003-296.

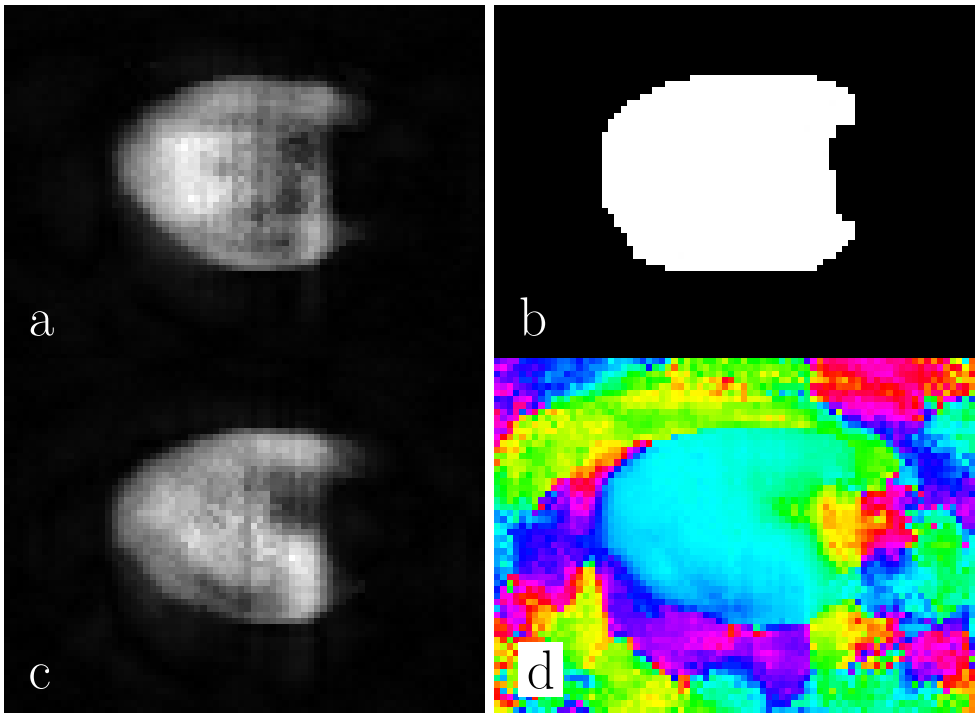

Figure 4.26: Real space reconstruction from fit 4 of Pb1003-296. a) is the prefit used to obtain the tight support shown in b). The resultant density c) from the fit still has abnormally low areas which correspond to areas of a different phase in d).

greatly, corresponding to regions in which the phase was nonzero. It should be explained that during each cycle of ER the phase in real space is forced to be zero, but the real space image written out at the termination of the program is the Fourier transform of the measured amplitude with the recovered phases. More precisely, it is the real space iterate before the the before the real-space constraints are applied. This output was chosen so that the user could see how well the fit was meeting the constraints applied to it. The presence of phase structure inside the real space reconstruction after many iterations suggests that at each iteration the routine is suppressing the density in certain areas, effectively multiplying it by the cosine of the phase if the phase is between $-\pi/2$ and $\pi/2$, otherwise setting the density to zero at those points.

Fit 5 was carried out using binned data and a new mode of **3dmultifit2**, error reduction with support only, or ERso, in conjunction with fHIO. The naming of this algorithm is chosen to emphasize its similarity to the Error Reduction Algorithm. It is not proven to be an error reduction algorithm itself. By allowing the phase to vary a considerably lower error metric was recovered, χ^2=0.021, as shown in in Fig. 4.27. More significantly, the recovered shape is much more physically meaningful, without internal gaps of a missing region at the substrate interface. The irreproducibility, ξ_1^2=0.024, where ξ_1^2 of two complex data sets $A1$ and $A2$ with N elements is defined as,

$$\xi_1^2 = \frac{\sum_{i=1} N(|A1(i)| - A2(i)|)^2}{\sum_{i=1}^{N} |A1(i)|^2} \tag{4.2}$$

The Section 5.3 describes the fitting of this recovered density to a thermodynamic model of an equilibrium crystal shape.

4.3.7 Phasing Pb1003-307

Pb1003-307 was initially composed of 40 frames, each 411×187. A background was prepared by passing the first two and last two frames to **makeback** and then subtracted from each slice. The individual slices were cropped to 400×160 to center the diffraction pattern and then binned 4×2 to improve statistics and to speed fitting. Fig. 4.29 shows that the binned data is still oversampled with over three pixels per fringe in x and four and a half pixels per fringe in y. After the slices are passed to **dofft** and **realtocomplex**, 32

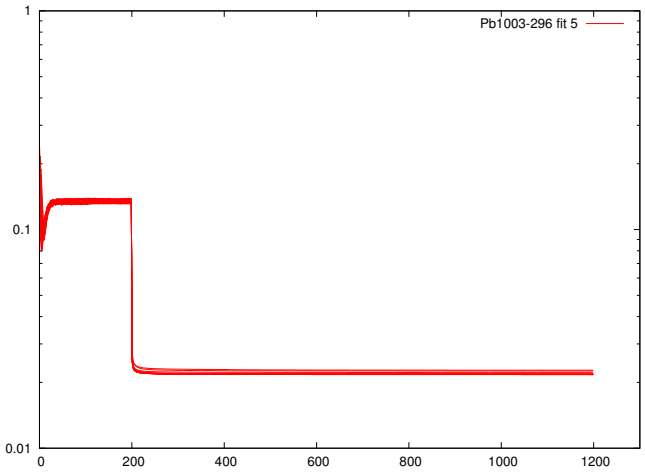

Figure 4.27: χ^2 error metric from fifth fit to Pb1003-296.

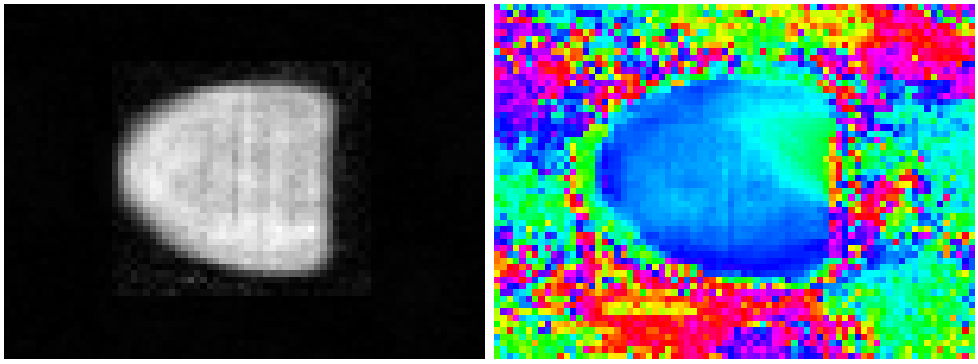

Figure 4.28: Real space reconstruction from fit 5 of Pb1003-296.

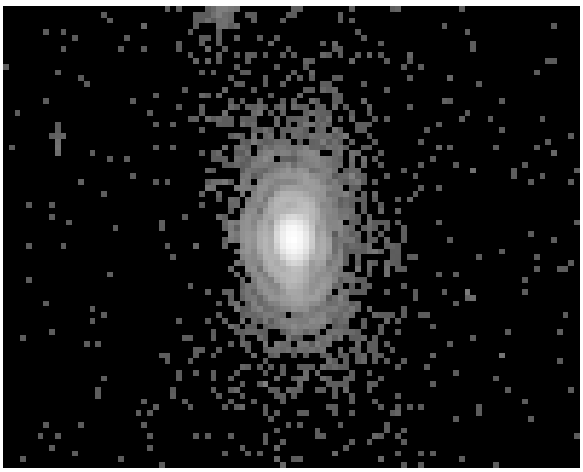

Figure 4.29: Pb1003-307 data, binned 4×2.

of the frames are then stacked using **2dto3d** to form a $100 \times 80 \times 32$ pixel array. The array is then inverted (without phase wrapping) using **3dinvert**.

The data was initially fit using a large support, $50 \times 26 \times 16$, as shown in Fig. 4.30a. The result of this fit was used to generate a new support, shown in Fig 4.30b, using **makenewcon**. A new set of fits were carried out with **3dmultifit2**, using 300 iterations of mode 5, 100 iterations of mode 17, and 500 iterations of mode 18, as defined in Table 3.1. The central slice from the best resultant real space fit is show in Figs. 4.30a&b. The final error metric was χ^2=0.016, as shown in Fig. 4.31. Despite the low error metric the density is much less constant inside, appearing to exhibit artifacts from the phasing algorithm. The irreproducibility is considerably worse, ξ_1^2=0.16. This indicates the the algorithm has not found a unique solution.Analysis of the shape recovered from the phasing of Pb1003-307 is performed in Section 5.4.

4.3.8 Phasing Pb1003-310

Pb1003-310 was initially $410 \times 186 \times 40$. Individual slices were cropped to 360×180. A background background was composed by adding frames 1,2,4 and 5 of a Pb1003-311, a background acquired immediately after Pb1003-311. Frame 3 was not used because of a long streak in the data from a cosmic ray hitting the detector. The sum of the frames was used because **makeback** was not yet written. Background subtraction was carried out by **flatten2**.

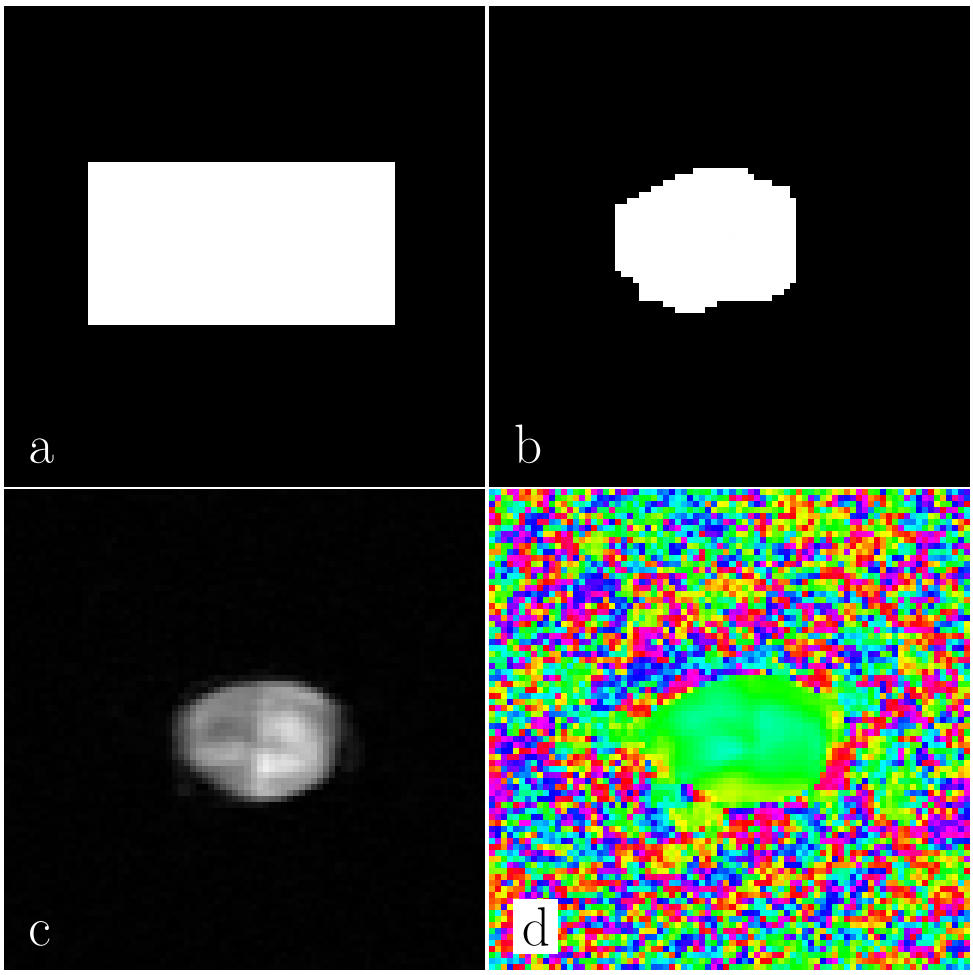

Figure 4.30: Initial (a) and tighter (b) constraints used to fit Pb1003-307. The density (c) shows more variation than the fit to Pb1003-296, Fig. 4.28. Phase is shown in d.

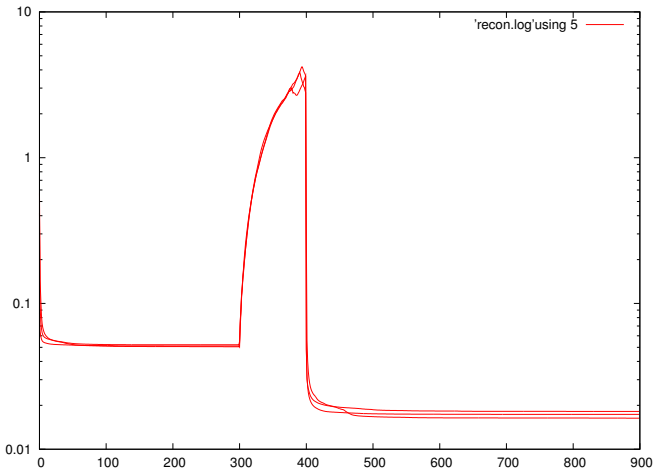

Figure 4.31: χ^2 error metric from fit to Pb1003-307.

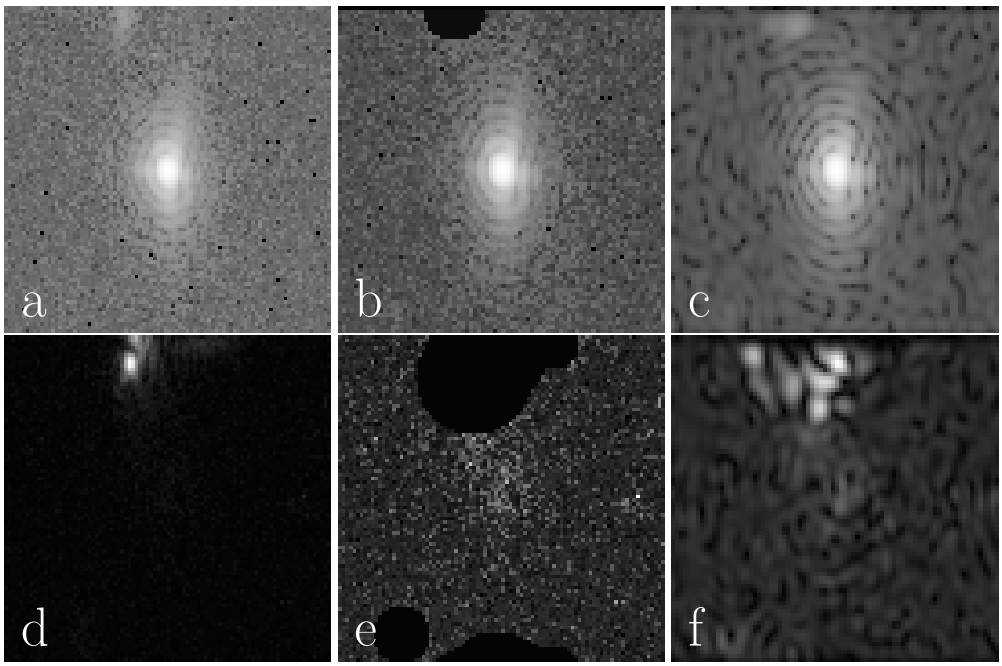

Figure 4.32: Flagging of Pb1003-310. a-c show the middle frame (21), d-f show a frame near the end (37), displayed on a logarithmic scale. a and d show the data after it has been cropped, had its background removed, and had its square root taken. b and e show the data after flagging, and c and f show the amplitudes fit to those slices in the phasing routine.

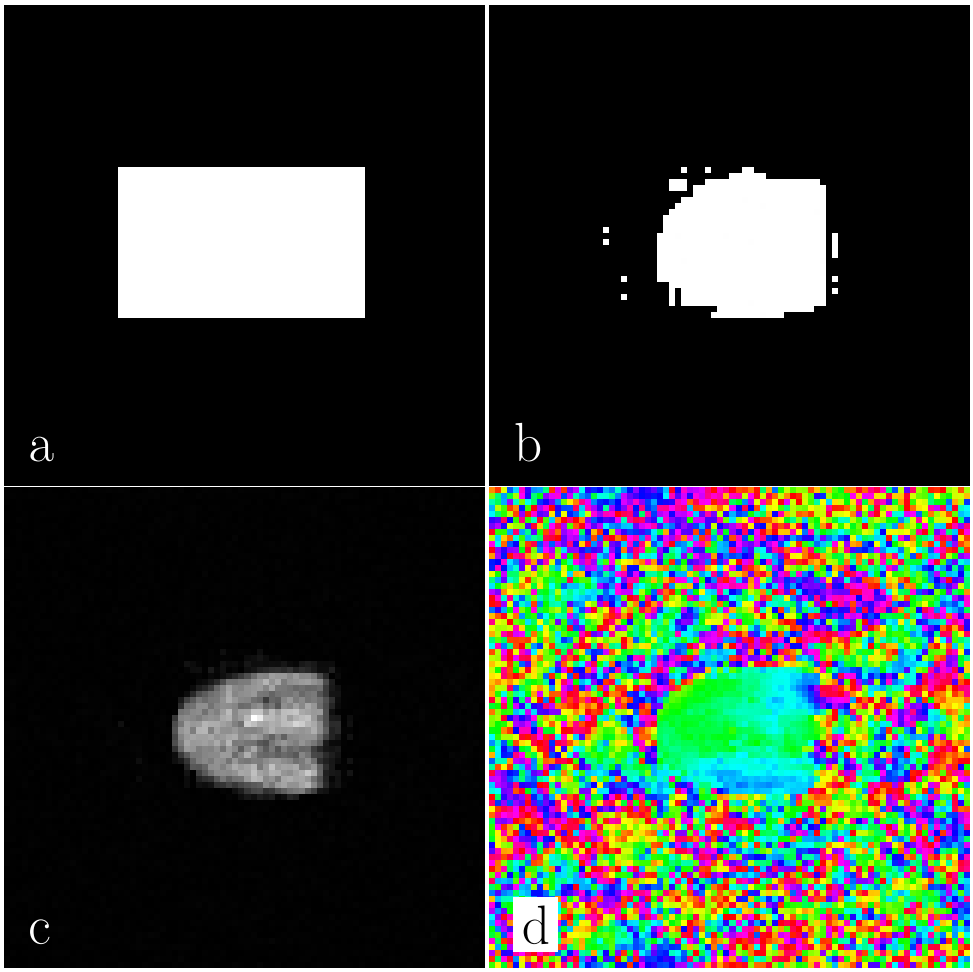

Figure 4.33: Initial (a) and tighter (b) constraints used to fit Pb1003-310. The density (c) shows more variation than the fit to Pb1003-296, Fig. 4.28. Phase is shown in d.

After background subtraction the frames were plotted using **2dplot** and viewed in the GIMP. All of the frames had to be flagged using **2dflagsp4**. Slices of the data before and after flagging, as well as the amplitude fit to those slices, is shown in Fig.4.32.

A nearly identical procedure was used for Pb1003-310 and Pb1003-307. The initial support for Pb1003-307 was $40 \times 24 \times 16$. The initial support and new support made using the result of the initial fit as and input to **makenewcon** are shown in Fig. 4.33a&b. The real space amplitude and phase recovered using this new support are shown in Fig. 4.33c&d. The error metric and irreproducibility for this fit were χ^2=0.012 and ξ_1^2=0.064, as shown in Fig. 4.34.

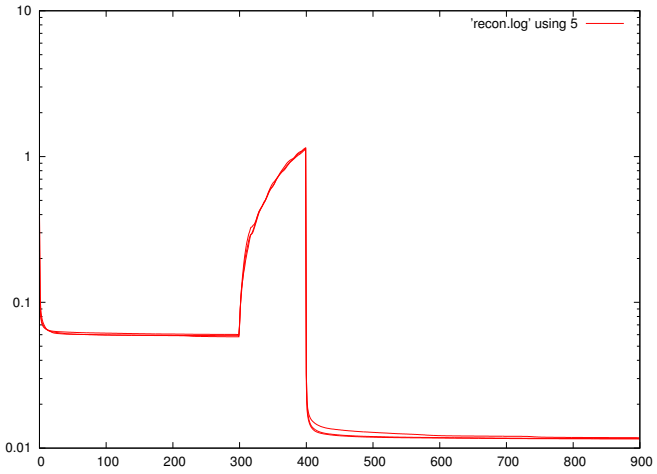

Figure 4.34: χ^2 error metric from fit to Pb1003-310.

Chapter 5

Analysis of Crystal Shapes

5.1 Geometric Considerations

The CXD patterns are measured in coordinates of p_x, p_y, and $\Delta\theta$, which do not compose an orthonormal basis. The real space reconstruction will therefore not be in an orthonormal basis, which means that it must undergo a geometric transformation before its shape can be analyzed. This involves examining the changes in $\mathbf{Q}$ with changes in measurement parameters in a fixed, orthonormal basis, and then transforming those basis vectors to find the real space vectors in which the reconstruction is embedded. Once these are known, the real space image can be transformed from one living on its original basis to one on an orthonormal basis.

The momentum transfer $\mathbf{Q}_{lab}$ relative to the laboratory frame can be expressed in terms of the magnitude of the momentum of the incoming X-rays k, the angular displacement from the center of the chip for a given pixel on the chip p_x and p_y, and the position of the detector in 2θ and Γ. The laboratory reference frame is a follows: z is the direction of the incident beam, y is vertical, and x is outboard (away from the synchrotron ring), as shown in Fig. 5.1. In order to relate the momentum transfer in the laboratory from to the momentum transfer in the frame of the sample, it is also necessary to know θ. The momentum transfer of the scattered X-rays can be written as $\mathbf{k}_f = \overleftrightarrow{R}_{2\theta}\overleftrightarrow{R}_{\Gamma}\overleftrightarrow{R}_{p_x}\overleftrightarrow{R}_{p_y}\mathbf{k}_i$. The rotations corresponding to positions on the detector are interchangeable since they involve very small angles, usually up to a few milliradians. The rotation $\overleftrightarrow{R}_{\Gamma}$ is about the x axis when 2θ=0, so it must be carried out before $\overleftrightarrow{R}_{2\theta}$, which is a rotation about the y axis.

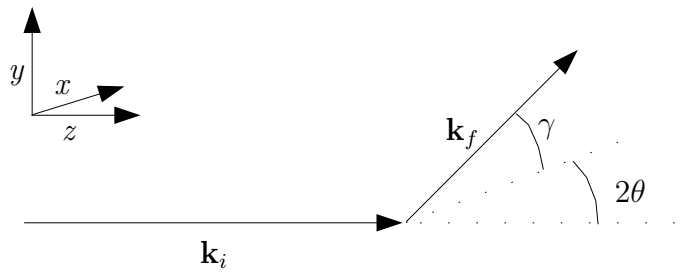

Figure 5.1: Laboratory reference frame. $\mathbf{k}_i$ is in the z direction, while $\mathbf{k}_f$ is rotate by 2θ in the horizontal plane and γ out of plane.

$$
\begin{aligned}
\overleftrightarrow{R_{p_y}} &= \begin{pmatrix} 1 & 0 & 0 \\ 0 & \cos p_y & -\sin p_y \\ 0 & \sin p_y & \cos p_y \end{pmatrix}, \overleftrightarrow{R_{p_x}} = \begin{pmatrix} \cos p_x & 0 & -\sin p_x \\ 0 & 1 & 0 \\ \sin p_x & 0 & \cos p_x \end{pmatrix}, \\
\overleftrightarrow{R_\Gamma} &= \begin{pmatrix} 1 & 0 & 0 \\ 0 & \cos\Gamma & \sin\Gamma \\ 0 & -\sin\Gamma & \cos\Gamma \end{pmatrix}, \overleftrightarrow{R_{2\theta}} = \begin{pmatrix} \cos 2\theta & 0 & \sin 2\theta \\ 0 & 1 & 0 \\ -\sin 2\theta & 0 & \cos 2\theta \end{pmatrix}, \\
\overleftrightarrow{R_\theta} &= \begin{pmatrix} \cos\theta & 0 & -\sin\theta \\ 0 & 1 & 0 \\ \sin\theta & 0 & \cos\theta \end{pmatrix}, \mathbf{k}_i = \begin{pmatrix} 0 \\ 0 \\ 1 \end{pmatrix} \\
\overleftrightarrow{R_{p_y}}\mathbf{k}_i &= \begin{pmatrix} 1 & 0 & 0 \\ 0 & \cos p_y & -\sin p_y \\ 0 & \sin p_y & \cos p_y \end{pmatrix} \begin{pmatrix} 0 \\ 0 \\ 1 \end{pmatrix} = \begin{pmatrix} 0 \\ -\sin p_y \\ \cos p_y \end{pmatrix} \\
\overleftrightarrow{R_{p_x}}\overleftrightarrow{R_{p_y}}\mathbf{k}_i &= \begin{pmatrix} \cos p_x & 0 & -\sin p_x \\ 0 & 1 & 0 \\ \sin p_x & 0 & \cos p_x \end{pmatrix} \begin{pmatrix} 0 \\ -\sin p_y \\ \cos p_y \end{pmatrix} = \begin{pmatrix} -\sin p_x \cos p_y \\ -\sin p_y \\ \cos p_x \cos p_y \end{pmatrix} \\
\overleftrightarrow{R_\Gamma}\overleftrightarrow{R_{p_x}}\overleftrightarrow{R_{p_y}}\mathbf{k}_i &= \begin{pmatrix} 1 & 0 & 0 \\ 0 & \cos\Gamma & \sin\Gamma \\ 0 & -\sin\Gamma & \cos\Gamma \end{pmatrix} \begin{pmatrix} -\sin p_x \cos p_y \\ -\sin p_y \\ \cos p_x \cos p_y \end{pmatrix} \\
&= \begin{pmatrix} -\sin p_x \cos p_y \\ -\cos\Gamma \sin p_y + \sin\Gamma \cos p_x \cos p_y \\ \sin\Gamma \sin p_y + \cos\Gamma \cos p_x \cos p_y \end{pmatrix}
\end{aligned}
\tag{5.1}
$$

$$\overleftrightarrow{R_{2\theta}}\overleftrightarrow{R_{\Gamma}}\overleftrightarrow{R_{p_x}}\overleftrightarrow{R_{p_y}}\mathbf{k}_i =$$
$$\begin{pmatrix} -\cos 2\theta \sin p_x \cos p_y + \sin 2\theta(\sin\Gamma \sin p_y + \cos\Gamma \cos p_x \cos p_y) \\ -\cos\Gamma \sin p_y + \sin\Gamma \cos p_x \cos p_y \\ \sin 2\theta \sin p_x \cos p_y + \cos 2\theta(\sin\Gamma \sin p_y + \cos\Gamma \cos p_x \cos p_y) \end{pmatrix} \quad (5.2)$$

$$\mathbf{Q}_{lab} = \mathbf{k}_f - \mathbf{k}_i =$$
$$\begin{pmatrix} -\cos 2\theta \sin p_x \cos p_y + \sin 2\theta(\sin\Gamma \sin p_y + \cos\Gamma \cos p_x \cos p_y) \\ \cos\Gamma \sin p_y + \sin\Gamma \cos p_x \cos p_y \\ -\sin 2\theta \sin p_x \cos p_y + \cos 2\theta(\sin\Gamma \sin p_y + \cos\Gamma \cos p_x \cos p_y) - 1 \end{pmatrix} \quad (5.3)$$

Slices through a 3D pattern were recorded by rotating the sample (and sample reference frame) about the vertical axis through an angle θ. Because we are interested in the momentum transfer in the frame of an individual crystal, $\mathbf{Q}$, we must rotate $\mathbf{Q}_{lab}$ by negative θ.

$$\mathbf{Q} = \begin{pmatrix} \cos\theta & 0 & -\sin\theta \\ 0 & 1 & 0 \\ \sin\theta & 0 & \cos\theta \end{pmatrix} \times$$
$$\begin{pmatrix} -\cos 2\theta \sin p_x \cos p_y + \sin 2\theta(\sin\Gamma \sin p_y + \cos\Gamma \cos p_x \cos p_y) \\ -\cos\Gamma \sin p_y + \sin\Gamma \cos p_x \cos p_y \\ \sin 2\theta \sin p_x \cos p_y + \cos 2\theta(\sin\Gamma \sin p_y + \cos\Gamma \cos p_x \cos p_y) - 1 \end{pmatrix} =$$
$$\begin{pmatrix} \cos\theta(-\cos 2\theta \sin p_x \cos p_y + \sin 2\theta(\sin\Gamma \sin p_y + \cos\Gamma \cos p_x \cos p_y)) \\ -\sin\theta(\sin 2\theta \sin p_x \cos p_y + \cos 2\theta(\sin\Gamma \sin p_y + \cos\Gamma \cos p_x \cos p_y) - 1) \\ -\cos\Gamma \sin p_y + \sin\Gamma \cos p_x \cos p_y \\ \sin\theta(-\cos 2\theta \sin p_x \cos p_y + \sin 2\theta(\sin\Gamma \sin p_y + \cos\Gamma \cos p_x \cos p_y)) \\ +\cos\theta(\sin 2\theta \sin p_x \cos p_y + \cos 2\theta(\sin\Gamma \sin p_y + \cos\Gamma \cos p_x \cos p_y) - 1) \end{pmatrix} \quad (5.4)$$

The implementation of the discrete Fourier transform assumes that the steps in one variable are uniform. We therefore take the derivative of $\mathbf{Q}$ with respect to each of the variables changed during measuring a single diffraction

pattern.

$$\frac{\partial \mathbf{Q}}{\partial p_x} = \begin{pmatrix} -\cos\theta(\cos 2\theta \cos p_x \cos p_y + \sin 2\theta \cos\Gamma \sin p_x \cos p_y) \\ -\sin\theta(\sin 2\theta \cos p_x \cos p_y - \cos 2\theta \cos\Gamma \sin p_x \cos p_y) \\ -\cos\Gamma \sin p_x \cos p_y \\ \sin\theta(-\cos 2\theta \cos p_x \cos p_y - \sin 2\theta \cos\Gamma \sin p_x \cos p_y) \\ +\cos\theta(\sin 2\theta \cos p_x \cos p_y + \cos 2\theta \cos\Gamma \sin p_x \cos p_y) \end{pmatrix} \tag{5.5}$$

$$\frac{\partial \mathbf{Q}}{\partial p_y} = \begin{pmatrix} \cos\theta(\cos 2\theta \sin p_x \sin p_y + \sin 2\theta(\sin\Gamma \cos p_y - \cos\Gamma \cos p_x \sin p_y)) \\ +\sin\theta(\sin 2\theta \sin p_x \sin p_y + \cos 2\theta(-\sin\Gamma \cos p_y + \cos\Gamma \cos p_x \sin p_y)) \\ -\cos\Gamma \cos p_y - \sin\Gamma \cos p_x \sin p_y \\ \sin\theta(\cos 2\theta \sin p_x \sin p_y + \sin 2\theta(\sin\Gamma \cos p_y - \cos\Gamma \cos p_x \sin p_y)) \\ -\cos\theta(\sin 2\theta \sin p_x \sin p_y + \cos 2\theta(-\sin\Gamma \cos p_y + \cos\Gamma \cos p_x \sin p_y)) \end{pmatrix} \tag{5.6}$$

$$\frac{\partial \mathbf{Q}}{\partial \theta} = \begin{pmatrix} -\sin\theta(-\cos 2\theta \sin p_x \cos p_y + \sin 2\theta(\sin\Gamma \sin p_y + \cos\Gamma \cos p_x \cos p_y)) \\ -\cos\theta(\sin 2\theta \sin p_x \cos p_y + \cos 2\theta(\sin\Gamma \sin p_y + \cos\Gamma \cos p_x \cos p_y) - 1) \\ 0 \\ +\cos\theta(-\cos 2\theta \sin p_x \cos p_y + \sin 2\theta(\sin\Gamma \sin p_y + \cos\Gamma \cos p_x \cos p_y)) \\ -\sin\theta(\sin 2\theta \sin p_x \cos p_y + \cos 2\theta(\sin\Gamma \sin p_y + \cos\Gamma \cos p_x \cos p_y) - 1) \end{pmatrix} \tag{5.7}$$

In order to treat the spacing in the Fourier space as uniform, we must now take the zeroth order approximations for p_x, p_y, and θ. The full range of p_x and p_y is $\pm 0.7°$, while the extent of a pattern is typically $\pm 0.14°$. The typical range for θ is $\pm 0.16°$. This simplifies the derivatives further, to

$$\frac{\partial \mathbf{Q}}{\partial p_x} = \begin{pmatrix} -\cos 2\theta \\ 0 \\ \sin 2\theta \end{pmatrix} \tag{5.8}$$

$$\frac{\partial \mathbf{Q}}{\partial p_y} = \begin{pmatrix} \sin 2\theta \sin \Gamma \\ -\cos \Gamma \\ \cos 2\theta \sin \Gamma \end{pmatrix} \tag{5.9}$$

$$\frac{\partial \mathbf{Q}}{\partial \theta} = \begin{pmatrix} 1 - \cos 2\theta \cos \Gamma \\ 0 \\ \sin 2\theta \cos \Gamma \end{pmatrix}. \tag{5.10}$$

If we define the span of the experimental data as

$$\begin{aligned} A^* &= N_x \delta p_x \frac{\partial \mathbf{Q}}{\partial p_x} \\ B^* &= N_y \delta p_y \frac{\partial \mathbf{Q}}{\partial p_y} \\ C^* &= N_\theta \delta \theta \frac{\partial \mathbf{Q}}{\partial \theta}, \end{aligned} \tag{5.11}$$

where N_x, N_y, and N_θ are the number of steps taken in each measurement parameter and δp_x, δp_y, and $\delta \theta$ are the step sizes for each variable, then the basis vectors of the reconstruction are

$$\begin{aligned} A &= \frac{B^* \times C^*}{A^* \cdot (B^* \times C^*)} \\ B &= \frac{C^* \times A^*}{A^* \cdot (B^* \times C^*)} \\ C &= \frac{A^* \times B^*}{A^* \cdot (B^* \times C^*)}. \end{aligned} \tag{5.12}$$

$$\frac{A^* \times B^*}{N_x N_y \delta p_x \delta p_y} = \begin{pmatrix} -\cos 2\theta \\ 0 \\ \sin 2\theta \end{pmatrix} \times \begin{pmatrix} \sin 2\theta \sin \Gamma \\ -\cos \Gamma \\ \cos 2\theta \sin \Gamma \end{pmatrix}$$

$$= \begin{pmatrix} \sin 2\theta \cos \Gamma \\ \sin \Gamma \\ \cos 2\theta \cos \Gamma \end{pmatrix} \tag{5.13}$$

$$\frac{B^* \times C^*}{N_y N_\theta \delta p_y \delta \theta} = \begin{pmatrix} \sin 2\theta \sin \Gamma \\ -\cos \Gamma \\ \cos 2\theta \sin \Gamma \end{pmatrix} \times \begin{pmatrix} 1 - \cos 2\theta \cos \Gamma \\ 0 \\ \sin 2\theta \cos \Gamma \end{pmatrix}$$

$$= \begin{pmatrix} -\sin 2\theta \cos^2 \Gamma \\ \cos 2\theta \sin \Gamma - \sin \Gamma \cos \Gamma \\ \cos \Gamma - \cos 2\theta \cos^2 \Gamma \end{pmatrix} \tag{5.14}$$

$$\frac{C^* \times A^*}{N_x N_\theta \delta p_x \delta \theta} = \begin{pmatrix} 1 - \cos 2\theta \cos \Gamma \\ 0 \\ \sin 2\theta \cos \Gamma \end{pmatrix} \times \begin{pmatrix} -\cos 2\theta \\ 0 \\ \sin 2\theta \end{pmatrix}$$

$$= \begin{pmatrix} 0 \\ -\sin 2\theta \\ 0 \end{pmatrix} \tag{5.15}$$

$$B^* \cdot (C^* \times A^*) = N_x N_y N_\theta \delta p_x \delta p_y \delta \theta \begin{pmatrix} \sin 2\theta \sin \Gamma \\ -\cos \Gamma \\ \cos 2\theta \sin \Gamma \end{pmatrix} \cdot \begin{pmatrix} 0 \\ -\sin 2\theta \\ 0 \end{pmatrix}$$

$$= N_x N_y N_\theta \delta p_x \delta p_y \delta \theta \sin 2\theta \cos \Gamma \tag{5.16}$$

$$A = \frac{B^* \times C^*}{B^* \cdot (C^* \times A^*)} = \frac{1}{N_x \delta p_x \sin 2\theta \cos \Gamma} \begin{pmatrix} -\sin 2\theta \cos^2 \Gamma \\ \cos 2\theta \sin \Gamma - \sin \Gamma \cos \Gamma \\ \cos \Gamma - \cos 2\theta \cos^2 \Gamma \end{pmatrix} \tag{5.17}$$

$$B = \frac{C^* \times A^*}{B^* \cdot (C^* \times A^*)} = \frac{1}{N_y \delta p_y \sin 2\theta \cos \Gamma} \begin{pmatrix} 0 \\ -\sin 2\theta \\ 0 \end{pmatrix} \tag{5.18}$$

$$C = \frac{A^* \times B^*}{B^* \cdot (C^* \times A^*)} = \frac{1}{N_\theta \delta \theta \sin 2\theta \cos \Gamma} \begin{pmatrix} \sin 2\theta \cos \Gamma \\ \sin \Gamma \\ \cos 2\theta \cos \Gamma \end{pmatrix} \tag{5.19}$$

If we combine the three basis vectors horizontally into a single matrix $\overleftrightarrow{T}$, then a position of a point $\vec{P'}$ in the space of the reconstruction corresponds to a point in an orthonormal space $\vec{P} = \vec{P'} \overleftrightarrow{T}$.

$$\overleftrightarrow{T} = \frac{1}{\sin 2\theta \cos \Gamma} \times \begin{pmatrix} -\sin 2\theta \cos^2 \Gamma / N_x \delta p_x & 0 & \sin 2\theta \cos \Gamma / N_\theta \delta \theta \\ (\cos 2\theta \sin \Gamma - \sin \Gamma \cos \Gamma) / N_x \delta p_x & -\sin 2\theta / N_y \delta p_y & \sin \Gamma / N_\theta \delta \theta \\ (\cos \Gamma - \cos 2\theta \cos^2 \Gamma) / N_x \delta p_x & 0 & \cos 2\theta \cos \Gamma / N_\theta \delta \theta \end{pmatrix} \tag{5.20}$$

5.2 Density Variations

In order to analyze the facet energetics and surface melting or "softening" behavior a set of analysis programs were written. The first of these, **findsurface** reads in a 3D sp4array with density values and writes out a real sp4array with the same dimensions which contains data values of 1 for points on the surface of an object in the input array, and zero everywhere else. **findsurface** first scans through the input array to find the maximum value in the array and the maximum nearest-neighbor changes in density in the x, y and z directions. The program considers a point to be a surface point if it meets the following three criteria: *i*) the change in density from a point to one of its six nearest neighbors is greater than ϵ times the maximum slope in that direction, *ii*) the density in the point is greater than τ times the maximum density, and *iii*) the density at the neighboring point is less than μ times the

maximum intensity. Criterion *i*) is based on the fact that at the interface of a crystal the density is changing rapidly. Criterion *ii*) eliminates stray points outside the crystal which may have a change between neighbors of ϵ times the maximum slope. Criterion *iii*) eliminates internal points with large changes. In an ideal reconstruction with a constant intensity inside and no intensity outside the crystal only *i*) would be necessary. Unfortunately sizable changes in density inside the crystal are sometimes recovered, forcing the parameter ϵ being low enough for the boundary points to be found that external points are included if *iii*) were not enforced. To get rid of any remaining outliers the program checks to see how many of the 26 nearest neighbors meet conditions *i*-*iii* and discards any points for which that number is less than five.

Once a set of points describing the surface are known they can be fit to the model of a nonequilibrium shape; a spherical shell truncated by planes. This fitting is done in multiple stages by a program called **modelecs**. A first guess for the shape is a sphere centered at the center of mass of the array of surface points with a radius of half the x dimension of the array. The sphere's center and radius are allowed to vary by fixed step sizes to minimize the error metric, after which the step size is reduced and the position a radius are refined further. This process is carried out eight times each time a new bounding object is added. The error metric is defined as the sum over all points of the distance from the point to the bounding object which is closest to the center of the sphere in that direction. It is simpler thinking of this in geometric terms– a line is drawn from the center of a circle through the point being considered. The first bounding object intersected by the line is the one used for determining the error metric consideration for that point. The absolute value of the shortest distance between the point and the bounding object is used as that point's contribution to the error.

After the sphere is fit, then planes are fit one at a time, with all parameters fit so far allowed to relax between the addition of each plane. The planes, identified as P0 through P'N-1', where N is the number of planes to be fit, are defined by vector connecting the center of the sphere to the nearest point on the plane. This completely defines a plane because one point on it is known, the end of the vector, and its orientation is known, since it must be perpendicular to the vector. The initial estimation for each plane is found by considering the vectors from the center to each surface point in the data file as defining a possible value for the new bounding plane, then assessing

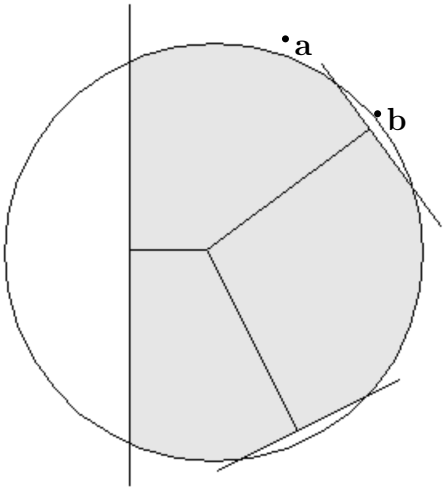

Figure 5.2: Modeling of the equilibrium shape. The error metric associated with point **a** is its distance to the surface of the sphere. Because the vector from the sphere's center to point **b** crosses a plane before the sphere, the distance between the plane and the point is used for the error metric of that point.

the error metric for a model with the current values for the sphere and any planes fit previously plus the new plane. The value for the new plane with the lowest error metric is used as a starting point for a refinement of all variables currently being fit.

The refinement is a simple exploration of the error metric among the nearest neighbors in all fit parameters, varying simultaneously. This means that for n free parameters the error metric must be evaluated at 3^n sets of values. This refinement can involve a large number of variables; 3 for the position of the sphere's center, 1 for the radius, and 3 for each plane currently being fit, meaning that for 5 planes, $3^{19} \approx 1.2 \times 10^9$ steps. Additionally, the evaluation of the error metric is linear with the number of planes being fit. This program typically takes between 10 and 30 minutes to fit a surface with 7 planes.

After fitting the surface points, the program writes out the error metric of the fit, the locate of the Wulff point which is the same as the center of the sphere, the radius of the sphere, the positions of all planes relative to the center, and the angles between the planes. If the continuous density data

file used to create the surface file is provided to the program, additional files are written out with the density as a function of radius for points closer to the spherical surface than any bounding plane, and density as a function of distance from a plane for all points closer to that plane than any other bounding surface. These show how sharp the interface is for the curved surface and for specific facets.

5.3 Pb1003-296

The approximate parameters for the geometric correction of Pb1003-296 were known from the experiment, but the exact parameters had to be fit along with the shape. The sample-detector distance was measured to be 52", or 1.32m, but was not known precisely because the position of the CCD chip inside the camera was not known. During the next experiment the detector distance was calculated by examining fine features in a diffraction pattern and observing their movement on the detector when either γ of 2θ is changed. The magnitude of the change in scattering vector associated with a 0.01° step in θ about a $\{111\}$ reflection of Pb is

$$\left|\frac{\partial \mathbf{Q}}{\partial \theta}\right| = |\mathbf{Q}| \times \delta\theta = \frac{2\pi\sqrt{3}}{4.95\text{Å}} \times \frac{0.01^\circ \pi}{180^\circ} = 3.84 \times 10^{-4}\text{Å}^{-1}. \tag{5.21}$$

At a distance of 1.32m and a wavelength of 1.38Å, the magnitude of the change in the scattering vector with respect to a change of position of one pixel on the detector is

$$\left|\frac{\partial \mathbf{Q}}{\partial p_x}\right| = \frac{2\pi}{1.38\text{Å}} \times \frac{20\mu m}{1.32m} = 6.90 \times 10^{-5}\text{Å}^{-1}. \tag{5.22}$$

A value of $1.37 \times 10^{-4}\text{Å}^{-1}$ was used because of the 2×2 binning of the pixels before fitting.

Because the need for a geometric correction was not considered until analyzing data after the experiment, the 2θ and γ angles were not carefully calibrated.

Using our initial estimates, the reconstructed image was clearly elongated in the z direction, causing the substrate interface to appear ellipsoidal. This 3% elongation is removed if the sample-detector distance is taken to be 1.36m,

within the error of our measurement.

Finding the precise values for γ and 2θ to use as inputs to **3dtransform** was slightly more challenging. Since the precision of γ and 2θ required to correctly model the shape was not known beforehand the angles were not zeroed before the measurement. This would have entailed placing the detector in the direct beam (with attenuators) to determine the exact spot hit when γ=2θ=0. For a range of values near those reported by the diffractometer, **3dtransform** was used to apply the geometric correction to the reciprocal space fit (with the center of the pattern in the center of the array, opposite that used while fitting), **3dinvert2** is used to place the result in the corners and apply the correct phase gradient so that Fourier transform, taken with **dofft** produces a real space image in the center of the array. The array is then cropped to $80 \times 80 \times 80$ using **3dcrop** to speed handling, and then the surface is found with **findsurface**, using $\epsilon = 0.2$, $\mu = 0.4$, and $\tau = 0.3$, as defined in Section 5.2. This surface is then fit using **modelecs**, with the number of planes to be fit chosen to be 7 or 8. A good fit was achieved using 2θ=25° and γ=12.61°. These are within reasonable error of the recorded values of 2θ=25.49° and γ=12.61°. Using the correct values for the distance spanned in reciprocal-space by a single pixel in the input array, $1.33 \times 1.33 \times 3.85(\times 10^{-4})^3 \text{Å}^{-3}$ in **3dtransform**, the program returns that the span of the geometrically corrected reciprocal-space array is $228(\times 10^{-4})^3 \text{Å}^{-3}$. Each pixel in the real space array is then simply

$$\delta x = \frac{2\pi}{\Delta Q} = \frac{2\pi}{228 \times 10^{-4} \text{Å}^{-1}} = 276\text{Å} = 27.6nm \tag{5.23}$$

Slices through the 3D density recovered by this method are shown in Fig. 5.3. This is a much more reasonable shape for an equilibrium crystal shape on a foreign substrate, which should be an truncated droplet, as derived in Section 2.1, than the bullet shape seen in Fig. 4.28.

The effect of the geometric correction can be seen in a surface plot of the uncorrected and corrected reconstructions, shown in Fig. 5.5. These images were created using **sp4tov5d** to put the data in the format for the free 3D imaging software **vis5d**[5]. The wetting angle in the uncorrected data appears to have completely different values at parts of the substrate interface. After correction, it is clear that the particle can be described by a sphere truncated by a set of planes, one fairly close to the center of the sphere and the others

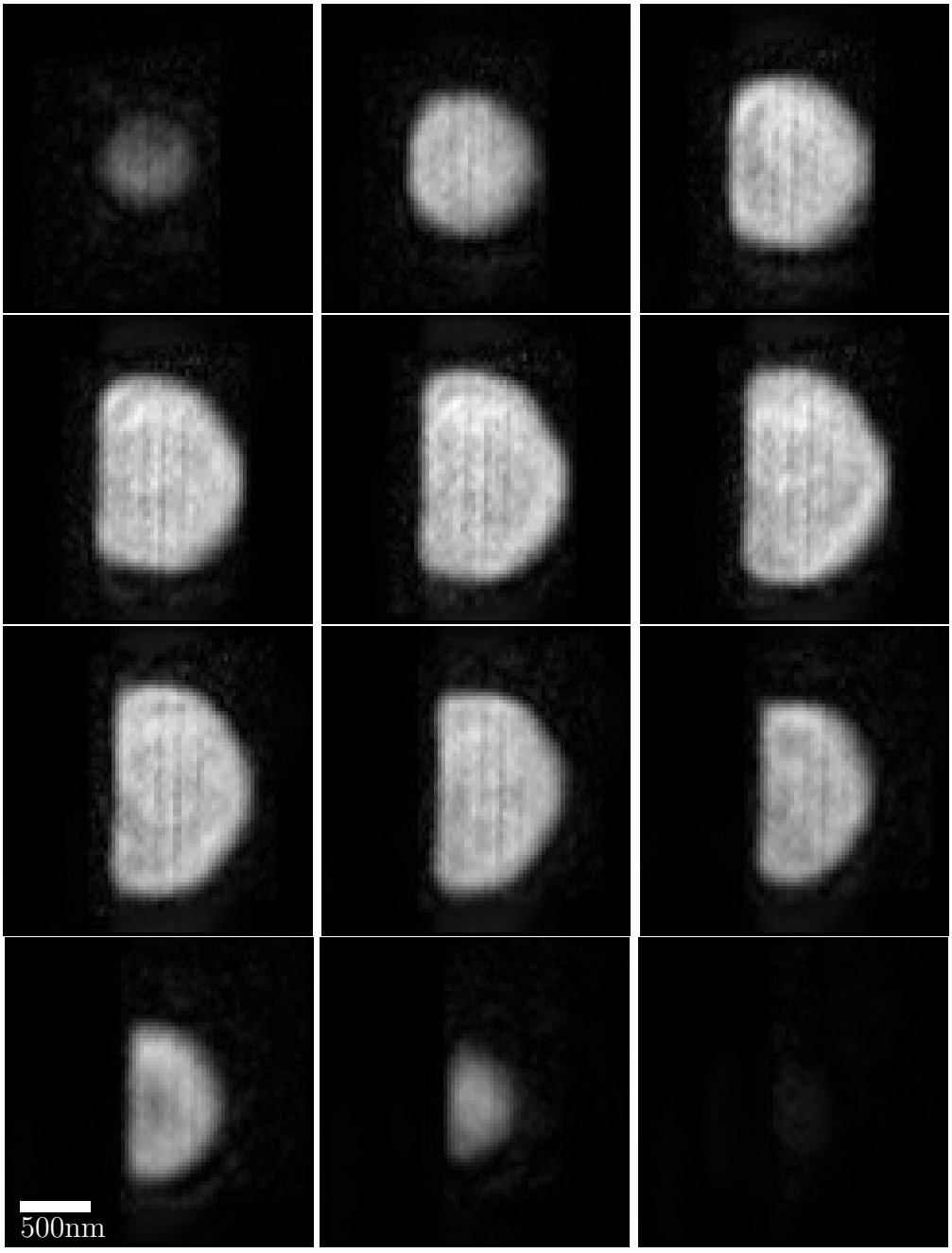

Figure 5.3: Real space density recovered from best fit phasing Pb1003-296, every fifth slice (138nm spacing).

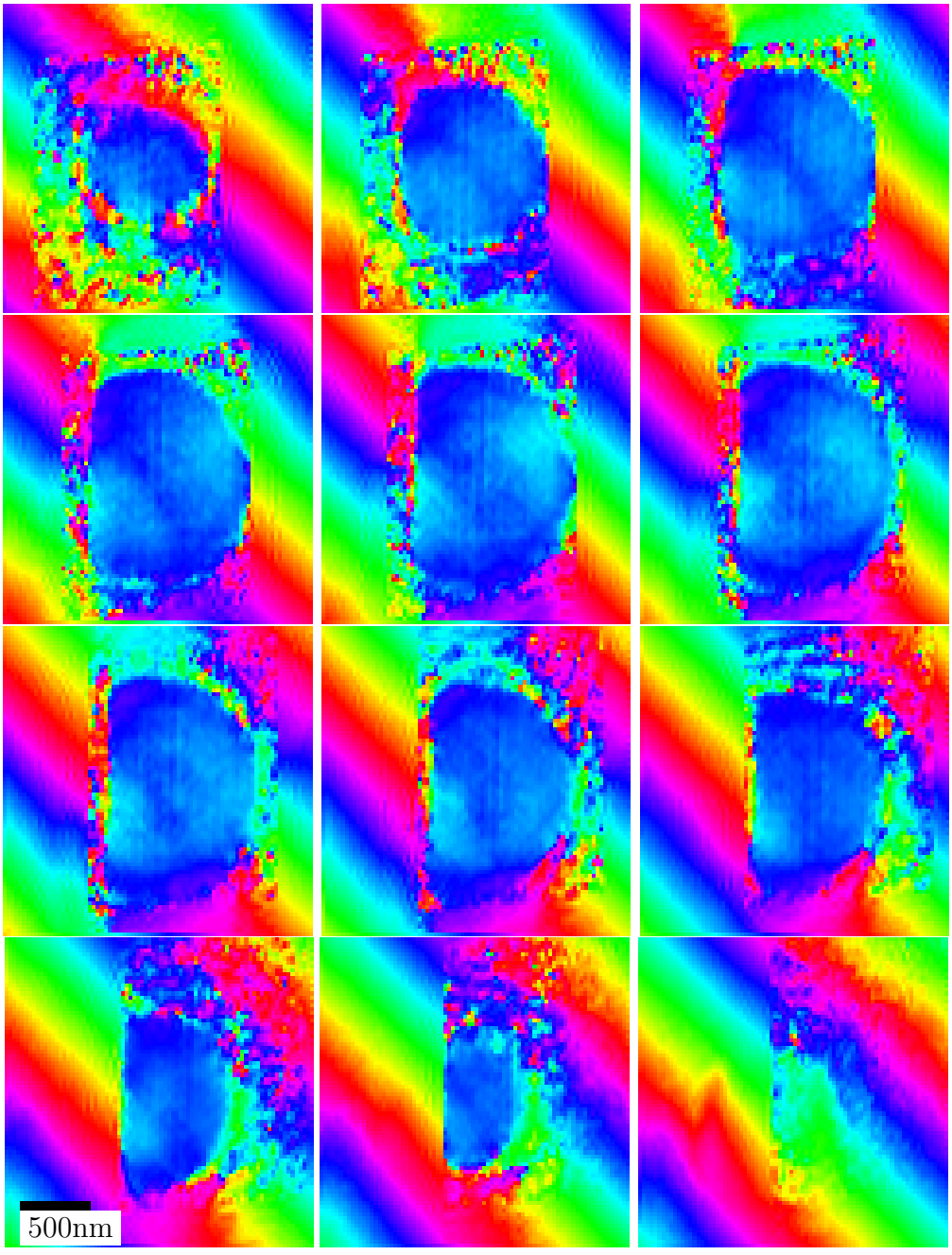

Figure 5.4: Real space phase recovered from phasing Pb1003-296, every fifth slice (138nm spacing).

nearly at the radial distance. Because of rounding in the graphics program these planes do not appear very sharp in the image.

After the general shape of the crystal, the most notable features are the vertical stripes parallel to the substrate interface. It is important to investigate whether these are real structures within the crystal or artifacts of the fitting algorithms, which have been seen to reproduce similar features parallel to strong interfaces in simulations. Line scans across the crystal in the x direction passing through the center of the crystal, Fig. 5.6, show much sharper variations than similar scans in the y and z directions, Figs. 5.7 and 5.8. These features are not reproduced between the density recovered from the best and second best fits to the data set.

The phase has been plotted on the same graph as the density. Phase offsets and density scaling have been applied so that the two types of data can be shown together and so that the phase from two fits lines up. The phase is fairly constant inside the crystal, but the features that are present are similar between fits. The greatest variation in the phase appears to be along the substrate interface. The density and phase along the y direction at the interface (x=25 in fit 1, x=20 in fit 2) and three pixels further into the crystal for the same slice (z=36 for fit 1, z=29 for fit 2) are shown in Fig. 5.9. The phase varies by as much as 1.47 radians over 30 pixels, a distance of 828nm. A comparison of the phase of the two best fits gives an estimate of the error of the phase, which is approximately 0.05 radians. As derived in Fig. 3.39 this phase gradient is the projection of a shift of the lattice onto the scattering vector $\mathbf{u}(\mathbf{r}) \cdot \mathbf{Q}$. The projection of the strain in the crystal on to the direction of the scattering is then $\mathbf{u}(\mathbf{r})_{(111)} = (1.47 \pm 0.05)/2.20\text{Å}^{-1} = (0.67 \pm 0.02)\text{Å}$.

The results of fitting the shape of the best fit to Pb1003-296 are given in Fig. 5.10 and in Table 5.1. The fit has been color coded to show the bounding objects of the shape, as well as any points in the surface file (white) which are not covered by the boundary objects. The spherical, roughened portions of the crystal are shown in red, all others are color coded as show in Table 5.1.

The {111} plane off which we are diffracting is located angularly half-way between the $-z$ direction, upstream, and the detector position, which is z

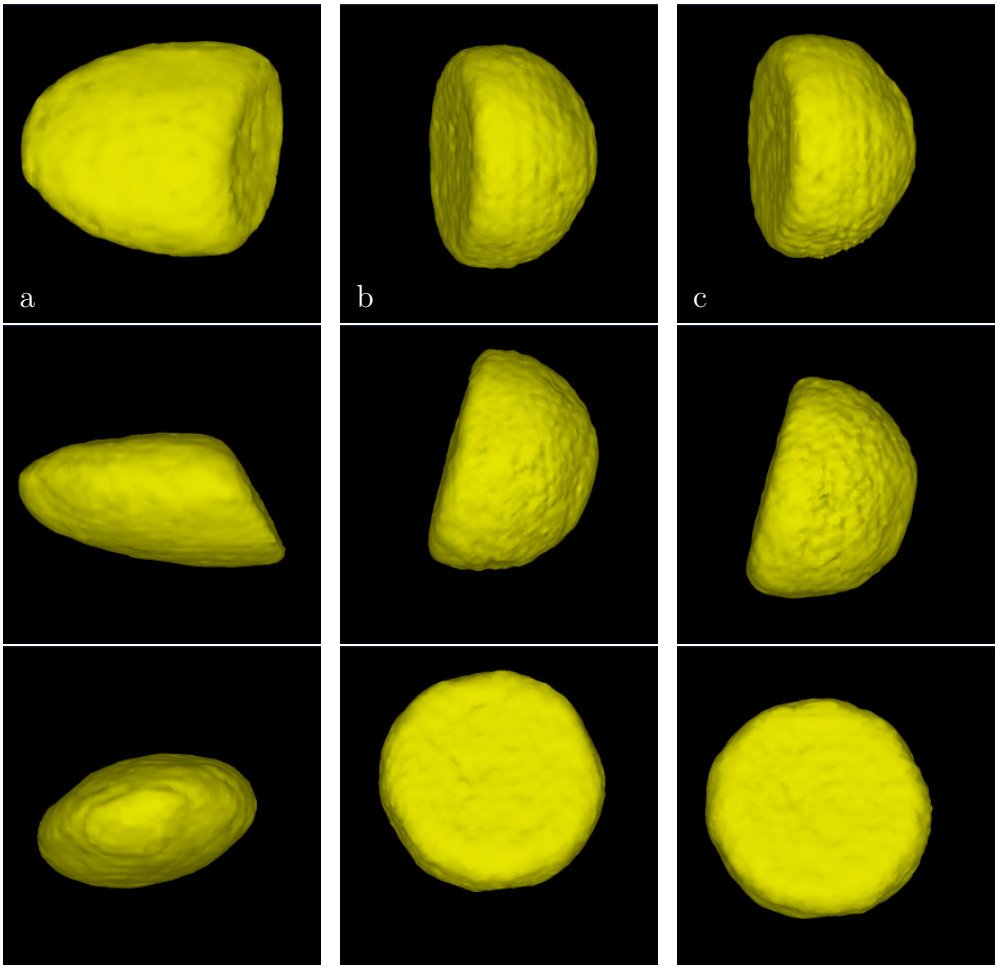

Figure 5.5: Surface plots of uncorrected best fit (a), geometrically corrected best fit (b), and second best fit (c). The top row is from the perspective looking upstream ($-z$ direction), the middle row is the view from below the crystal, and the bottom row is the view from inboard (looking in the $+x$ direction).

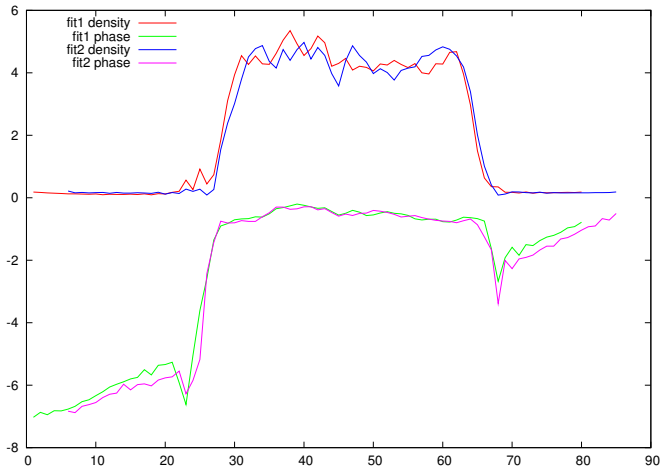

Figure 5.6: Density and phase along line in x direction across middle of best and second best fits to Pb1002-296.

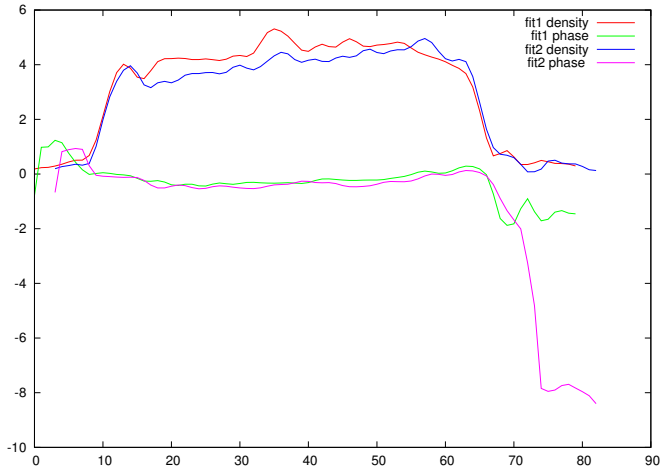

Figure 5.7: Density and phase along line in y direction across middle of best and second best fits to Pb1002-296.

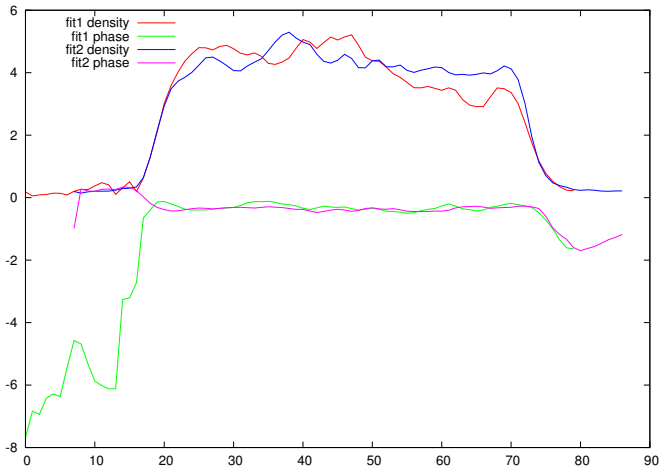

Figure 5.8: Density and phase along line in z direction across middle of best and second best fits to Pb1002-296.

	d		P0	P1	P2	P3	P4	P5	P6
	9.4	P0	0°	85°	149°	79°	134°	106°	71°
	25.7	P1		0°	123°	164°	83°	76°	102°
	25.1	P2			0°	72°	67°	74°	110°
	25.9	P3				0°	111°	106°	76°
	25.4	P4					0°	113°	68°
	25.4	P5						0°	176°
	26.0	P6							0°

Table 5.1: Distances from the Wulff point to bounding planes and angles between those bounding planes of the density recovered from the best fit phasing Pb1003-296.

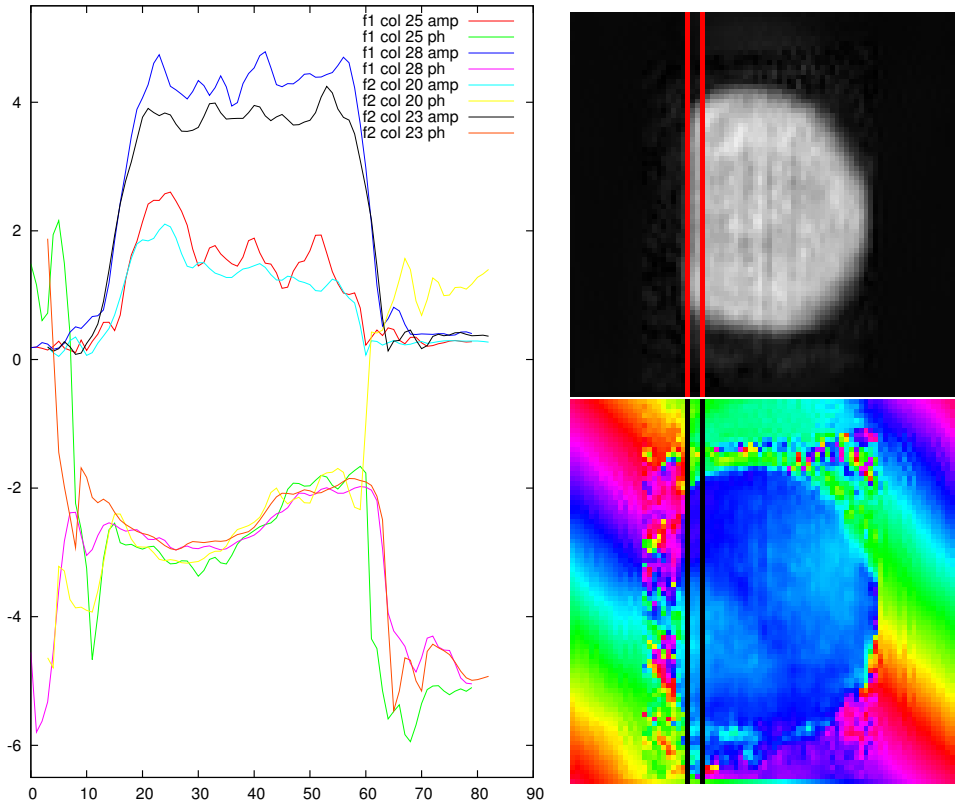

Figure 5.9: Contours of the amplitude and phase at the border of the crystal (f1 c25 and f2 c20) and three columns further into the crystal. The amplitude has been scaled to fit on the same axis as the phase, which is in units of radians. Offsets have been applied to positions and phases to make them line up. Shown on the right are the amplitude and phase maps which were sampled along the lines indicated in the images.

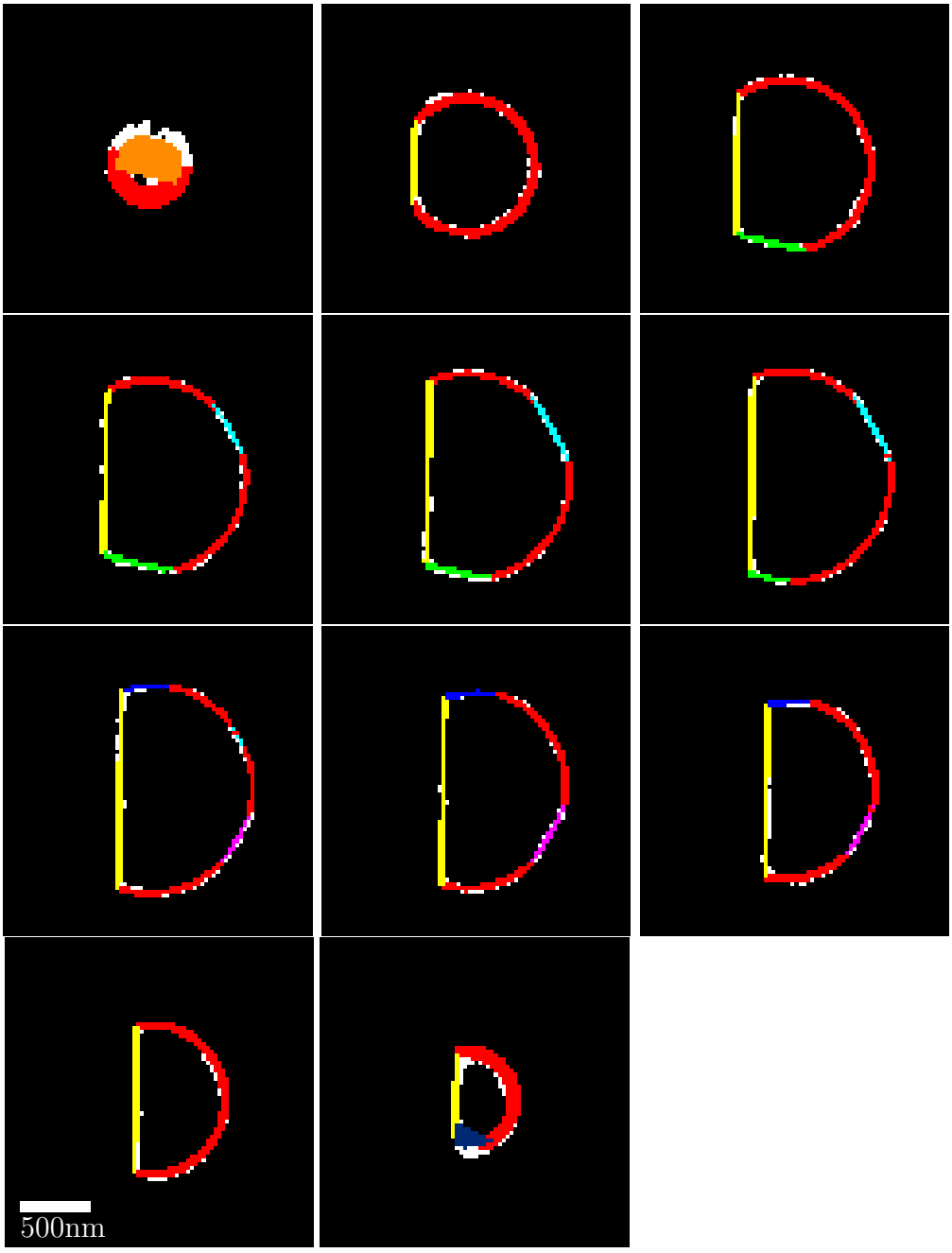

Figure 5.10: Shape fit to outline of density recovered from Pb1003-296, as shown in Fig. 5.3, every fifth slice (138nm spacing).

rotated by γ and 2θ,

$$\hat{\mathbf{h}} \propto \hat{\mathbf{Q}} = k \begin{pmatrix} \sin(25^\circ)\cos(12.61^\circ) \\ \sin(12.61^\circ) \\ \cos(25^\circ)\cos(12.61^\circ) \end{pmatrix} - k \begin{pmatrix} 0 \\ 0 \\ 1 \end{pmatrix} \tag{5.24}$$

$$= k \begin{pmatrix} 0.21 \\ 0.11 \\ -0.6 \end{pmatrix} \propto \begin{pmatrix} 22 \\ 12 \\ -6 \end{pmatrix} \cong \begin{pmatrix} 22.0 \\ 12.8 \\ -4.6 \end{pmatrix}, \tag{5.25}$$

where (22.0, 12.8, -4.6) is the position of P2. The values fit for P0, the substrate interface, are (-8.1, 0.1, 2.0). This corresponds to the plane of the substrate making an angle of atan(2.0/8.1)=13.86°, where the measured angle for θ was 13.82°.

Because of the Pb particle in this data set was approximately 1° below melting, it is expected that all facets other than {111} will have roughened. Because diffraction peaks were found everywhere on the powder ring, it is not expected for this to be true of the substrate interface. All other planes bounding the crystal are expected to be at angles of 71°, 109°, or 180°. To within ±4° this is true of P2 through P4, as shown in Table 5.1. P1 is the one plane that does not fall into a sensible crystallographic direction, but it appears very clearly in the reconstruction. It is possible that this plane is associated with a complex defect structure. Fig. 5.4 shows a strong phase structure at the substrate interface near the top left of the crystal in the vicinity of P1. It is possible that something on the substrate is pinning the crystal to that location and causing a strain which effects the shape in that immediate region. There is unfortunately no other evidence that this is happening and no other way to study this same crystal.

One measure of the reliability of the recovered shape is to compare it to the shape recovered from the second best fit phasing Pb1003-296. Table 5.2 shows a result which is comparable to 5.1. Planes 1 and 2 and planes 4 and 5 are switched between the fits, and P6 in the second fit appears to be spurious.

A closer fit to the first result can be achieved by using the surface file generated from the second fit along with the output of the first fit as starting point for **inputmodelecs**, which functions like **modelecs** with the exception that it reads in a log file to get the initial positions of the planes and sphere

	d		P0	P1	P2	P3	P4	P5	P6
	9.3	P0	0°	151°	91°	82°	104°	134°	72°
	24.7	P1		0°	112°	73°	755°	71°	97°
	26.5	P2			0°	171°	60°	77°	143°
	25.9	P3				0°	116°	112°	39°
	26.2	P4					0°	108°	154°
	25.5	P5						0°	92°
	26.4	P6							0°

Table 5.2: Planes from second best fit to phasing Pb1003-296. The plane distances are corrected in the manner described in Fig. 5.11 and Table 5.4

which it then refines. Using this method the result, in Table 5.3, agreed more closely to the first fit in Table 5.1, and had an error metric only 4% higher than the same data fit with no imput to influence the fit.

Now that the shape of the crystal is known the density can be studied as a function of direction and distance from the crystal's boundary to explore disorder in the crystal close to melting. If an SP4 containing density data is passed to **modelecs** or **inputmodelecs** in addition to the standard inputs of surface file name, output filename stem and number of planes to fit, the programs write out the density of each data point from the density file in an output file corresponding to which bounding object (spherical shell or P1-N) is the boundary of the crystal in the direction of that data point. The points are written out with a position given by their distance from the boundary, with negative numbers for inside the crystal and positive number outside.

	$\|R\|$		P0	P1	P2	P3	P4	P5	P6
	9.3	P0	0°	84°	150°	80°	134°	106°	72°
	26.0	P1		0°	124°	165°	83°	77°	102°
	24.8	P2			0°	71°	67°	74°	108°
	26.1	P3				0°	109°	105°	7°5
	25.5	P4					0°	113°	68°
	26.1	P5						0°	178°
	27.1	P6							0°

Table 5.3: Planes from second best fit to phasing Pb1003-296 using the plane locations from fit 1 (Table 5.1). The plane distances are corrected in the manner described in Fig. 5.11 and Table 5.4

	h_0	dx	h_0	m	1/m
R	27.2	-0.1	27.1	0.33	3.0
P0	8.3	1.0	9.3	0.39	2.0
P1	24.8	0.7	25.5	0.33	3.0
P2	25.9	-0.8	25.1	0.38	2.6
P3	26.0	0.11	26.0	0.42	2.4
P4	26.1	-0.6	25.5	0.32	3.1
P5	25.9	0.3	26.2	0.29	3.4
P6	25.7	0.5	26.1	0.24	4.2

Table 5.4: Parameters from fits in Fig. 5.11. h_o+dx gives the most accurate measure of the distance from the center of the sphere to a surface, where 1/m is a measure of how fast the density falls off, losing half of its value in 1/m.

Results for the best fit to Pb1003-296 are shown in Fig. 5.11.

Fig. 5.11a shows the density across the rounded regions of the crystal, with only one out of every 20 points plotted for clarity. On the same graph is a fit to the density profile. This fit, carried out in **gnuplot**[6], looks at the data in the window [-5,+5] and fits it to an error function of the equation f(x)=A*erf(-(x-dx)*m)+A. The other data sets were were fit to the same equation with A fixed at the value fit to the radial data, Fig. 5.11a). The parameters from these fits are found in Table 5.4. The best measure of the resolution is the value of 1/m, which is typically between 2 and 3 pixels, or 50nm to 83nm. It can be immediately seen that the density appears to drop of similarly for the the roughened portions of the crystal as for the bounding planes, with two exceptions. P0 and P6 have sharper and smoother boundaries, respectively, than the other bounding objects. These two facets have much larger and smaller areas than the other facets, corresponding to much higher and lower scattering intensities far from the central peak than the other facets. Because of the limited number of photons on the detector ($\sim 10^7$) this results in a resolution which can be affected by the area of a scattering surface.

According to Eqn. (2.36) our sample at $T_m - 1.2^\circ$ should only have a 3nm thick of quasi-liquid layer. Our temperature resolution was closer to 0.1°. A temperature of $T_m - 0.1^\circ$ should produce 20nm of surface melting. While this experiment did not detect surface melting, this is certainly feasible with this

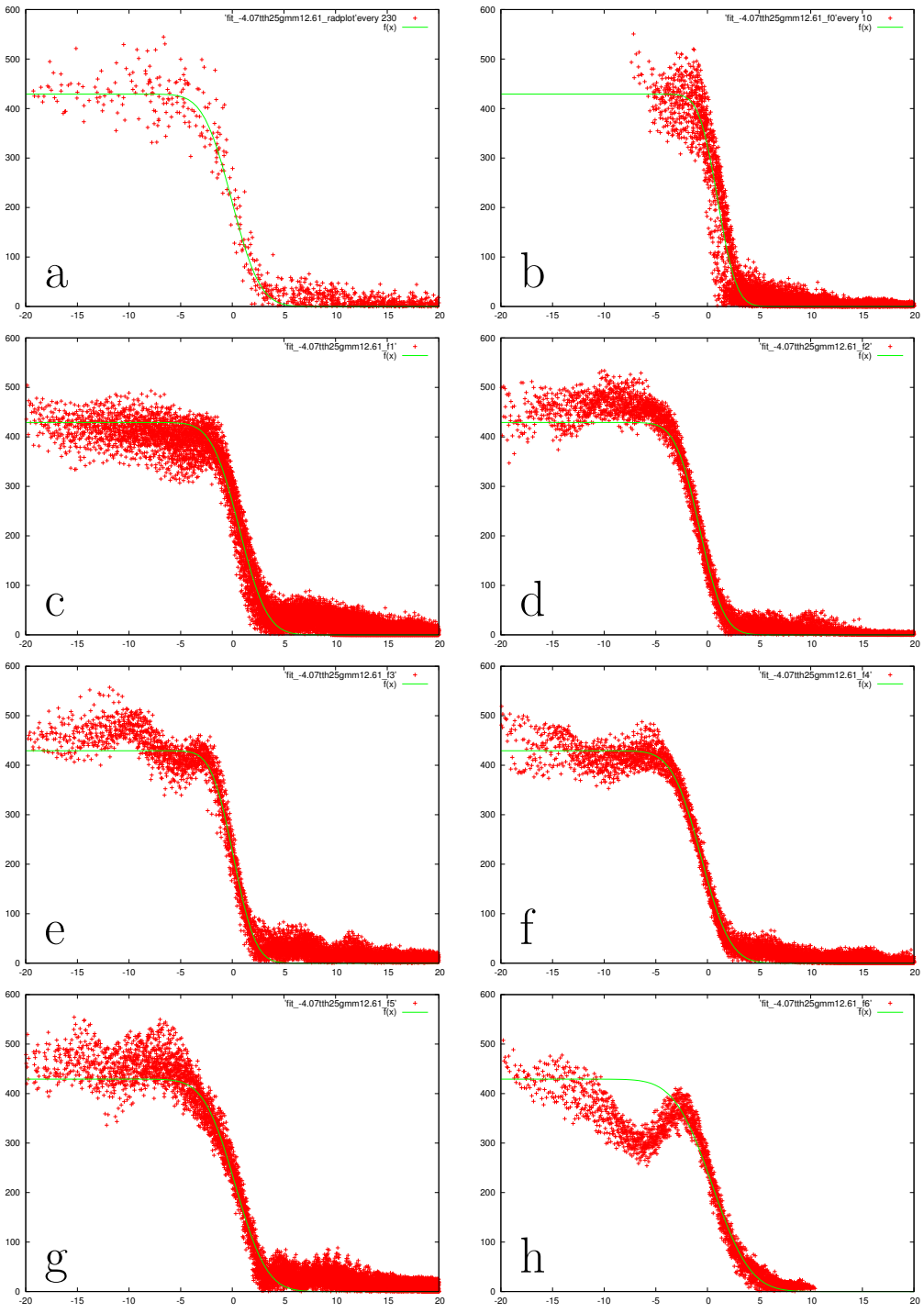

Figure 5.11: Plots of density across rounded portions of the crystal (a), and across planar boundaries of the crystal (b-h). The density plots are fit to error functions with a height fit in (a) and a slope and horizontal offset fit independently for each data set.

technique. More precise temperature, which could be accomplished by heating against active cooling, could allow us to approach closer to the melting temperature. A sample with a lower number density of grains would permit gathering diffraction patterns over a larger span of reciprocal space, which translates directly to improved real space resolution. We expect this would show a drastic decrease in apparent density near the roughened surface with no corresponding change in the (111) surface, corresponding to previous measurements of surface melting[47]. The potential advantage of this technique is that the direction of the disorder in the quasi-liquid layer could be probed. If the instantaneous displacement of atoms in the quasi-liquid layer from ideal lattice sites is written as $\mathbf{u}(\mathbf{r})$, Eqn. (3.40) dictates that the diffraction pattern about a Bragg peak $\mathbf{Q} = \mathbf{G}_m$ will only be sensitive to $\mathbf{G}_m \cdot \mathbf{u}(\mathbf{r})$. If for example, the quasi-liquid layer has greater order perpendicular to the substrate underneath it, that should be visible in a greater apparent density near the border on the roughened surface closest to the plane corresponding to the Bragg peak being measured.

5.4 Pb1003-307 and Pb1003-310

The geometric corrections for Pb1003-307 and Pb1003-310 were carried out in similar manner to Pb1003-296. Both data sets were binned 4×2 for fitting. Pb1003-307 was measured using 0.01° steps in θ, while Pb1003-310 was measured with 0.008° steps. Because the patterns were measured on a different region of the the detector, slightly different values were used for 2θ and γ. The parameters passed to **3dtransform** to apply the geometric correction to Pb1003-307 and Pb1003-310 are listed in Table 5.5. The spans of both geometrically corrected reciprocal space arrays was $\Delta Q = 288 \times 10^{-4}\text{Å}^{-1}$ giving a pixel size of $\delta x = 288\text{Å}$=28.8nm.

The shapes recovered from Pb1003-307 and Pb1003-310 were much more difficult to fit to equilibrium shapes using **modelecs** than Pb1003-296. When Pb1003-307 was fit to a five plane or higher model the fifth plane fit was in the correct location for the (111) plane contributing to the measured reflection. Using just this plane and the substrate interface as inputs to **inputmodelecs** the results in Table 5.6. A fit to the shape of Pb1003-310 yielded only the radius of the sphere and the position of the substrate interface. This is

	307	310
$\left\|\frac{\partial \mathbf{Q}}{\partial p_x}\right\|$	2.68	2.68
$\left\|\frac{\partial \mathbf{Q}}{\partial p_y}\right\|$	-1.34	-1.34
$\left\|\frac{\partial \mathbf{Q}}{\partial \theta}\right\|$	3.85	-3.08
2θ	25.51°	25.51°
γ	12.41°	12.41°

Table 5.5: Parameters used in geometric correction of Pb1003-307 and Pb1003-310. Wave vectors are in units of 10^{-4}Å^{-1}.

sufficient to compare the ratio of the free energy of the roughened surface to the substrate interface at two temperatures: $\gamma_r/\gamma_s(T_m - 1.0°) = 2.5$, and $\gamma_r/\gamma_s(T_m - 3.6°) = 4.2$. These values bracket the value recovered from Pb1003-296 which was a different particle at the same temperature as Pb1003-307: $\gamma_r/\gamma_s(T_m - 1.0°) = 2.9$. It is reasonable that energy of the substrate interface could depend on orientation for orientations which are roughened on the vacuum interface. Unfortunately, due to the quality of the real space fits to the diffraction data, comparisons with $\gamma_{(111)}$ were not possible.

Figs. 5.12 through 5.23 show the results of fitting the shapes of Pb1003-307 and Pb1003-310. Both fits show much greater internal variation in the internal density, over 24%. There is also less consistency between the results from phasing the data. The lower quality of these fits is almost certainly due to the contamination of the diffraction patterns by alien scatterers, visible in Figs. 4.12 and 4.13.

	307	310
R	19.1	19.7
P0	7.5	4.7
P1	17.1	
T	$T_m - 1.0°$	$T_m - 3.6°$

Table 5.6: Radius and planes fit to Pb1003-307 and Pb1003-310. The numbers are in pixels, which are 29nm across.

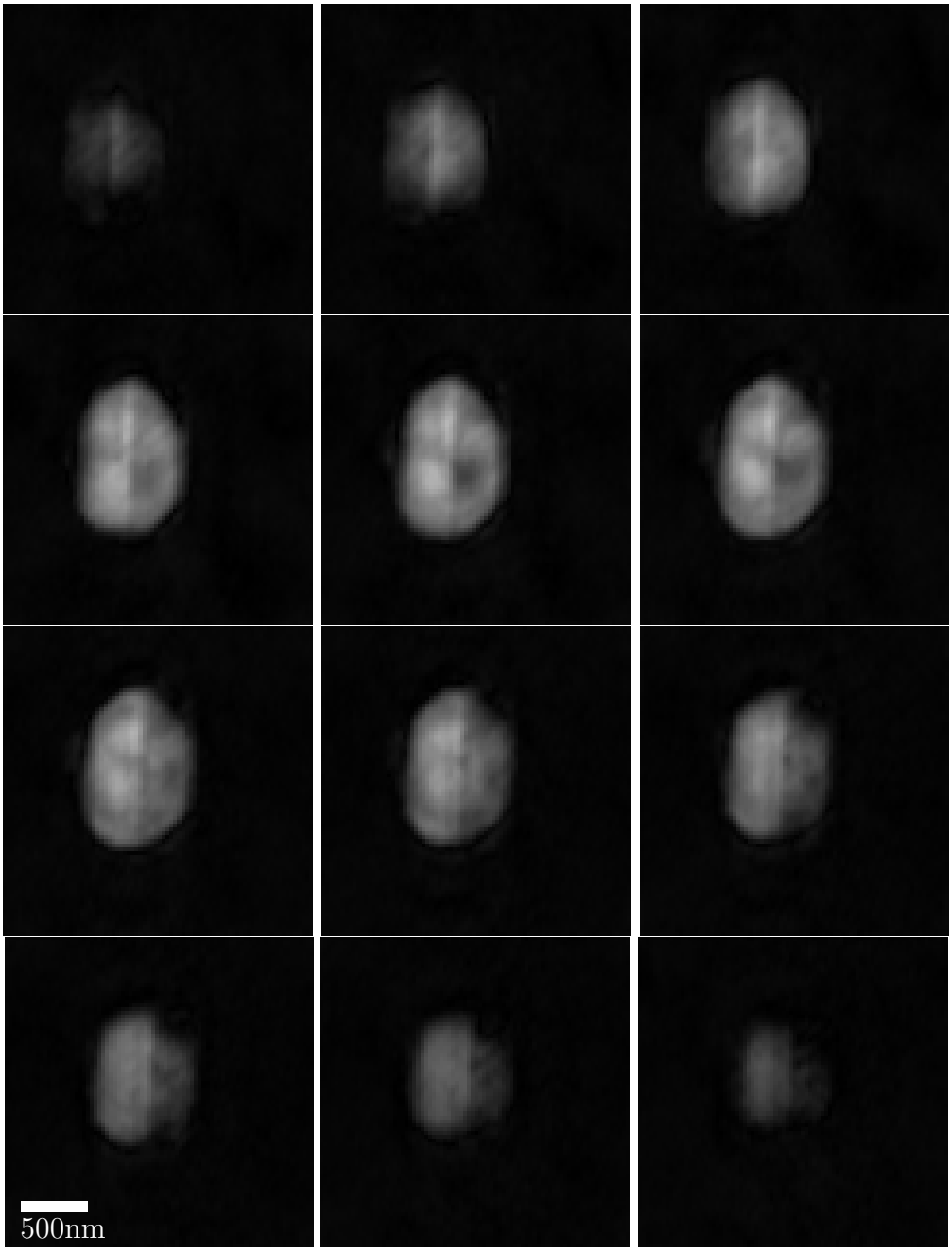

Figure 5.12: Density recovered from Pb1003-307, every third slice (86nm).

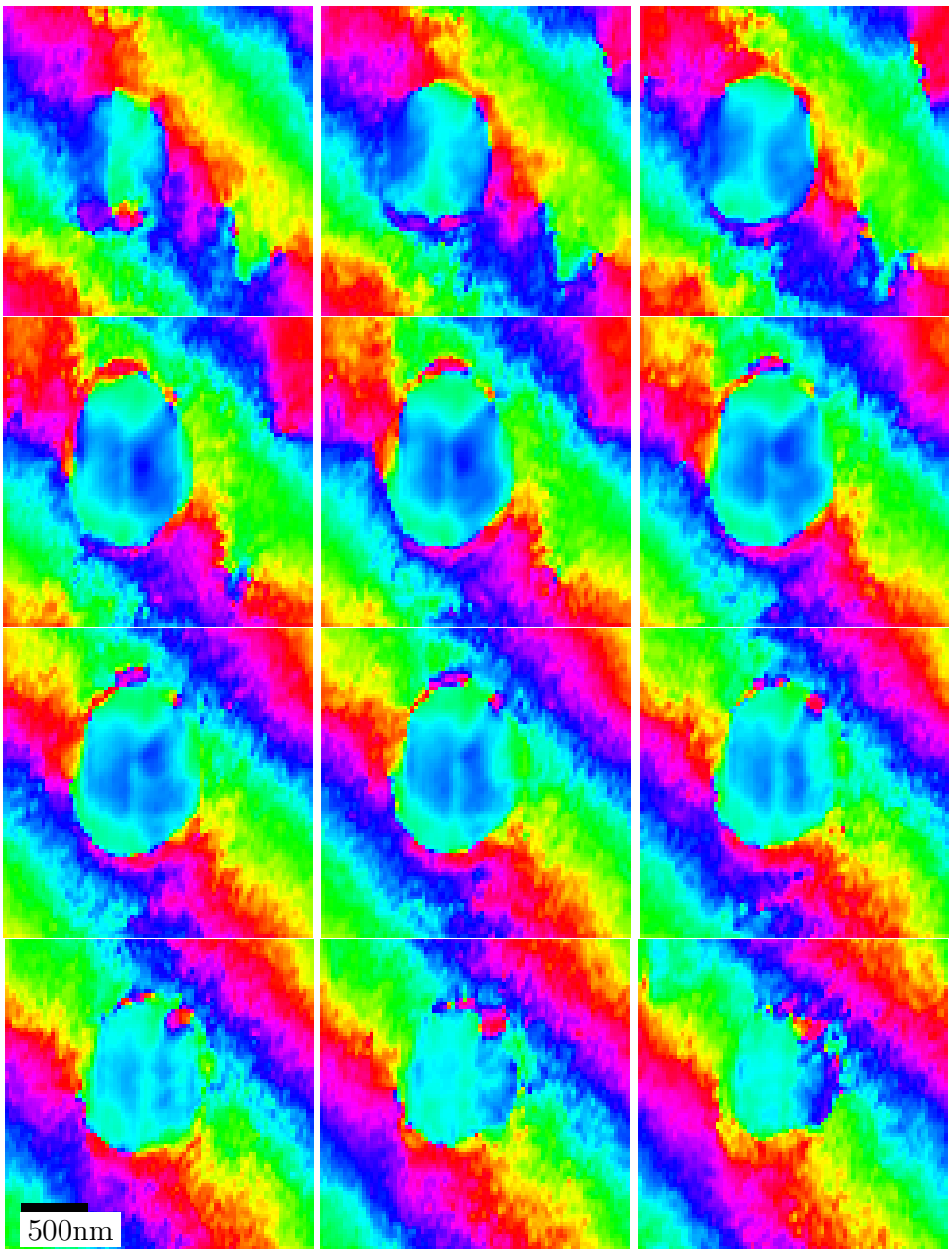

Figure 5.13: Phase recovered from Pb1003-307, every third slice (86nm).

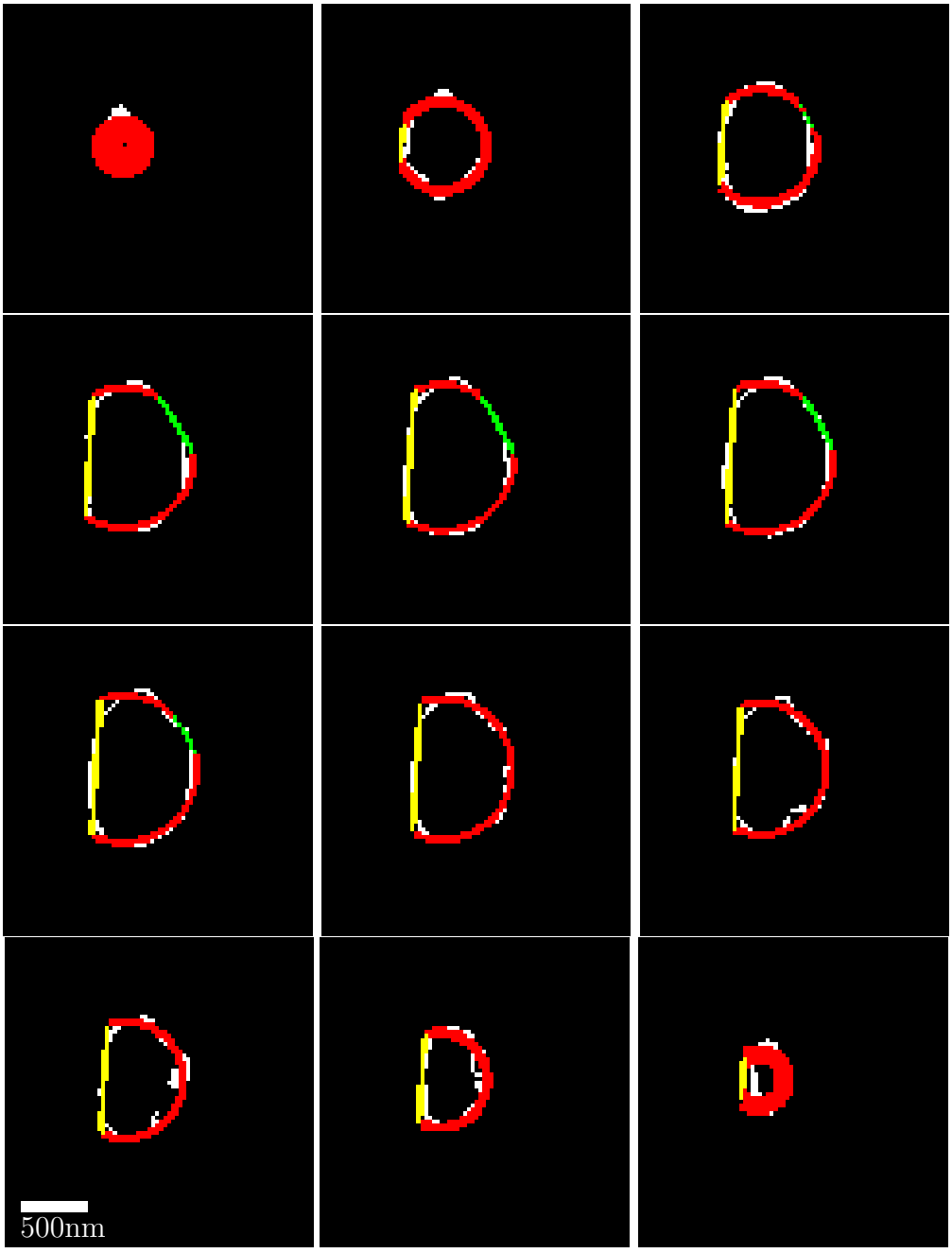

Figure 5.14: Shape fit to outline of density recovered from Pb1003-307, every third slice (86nm).

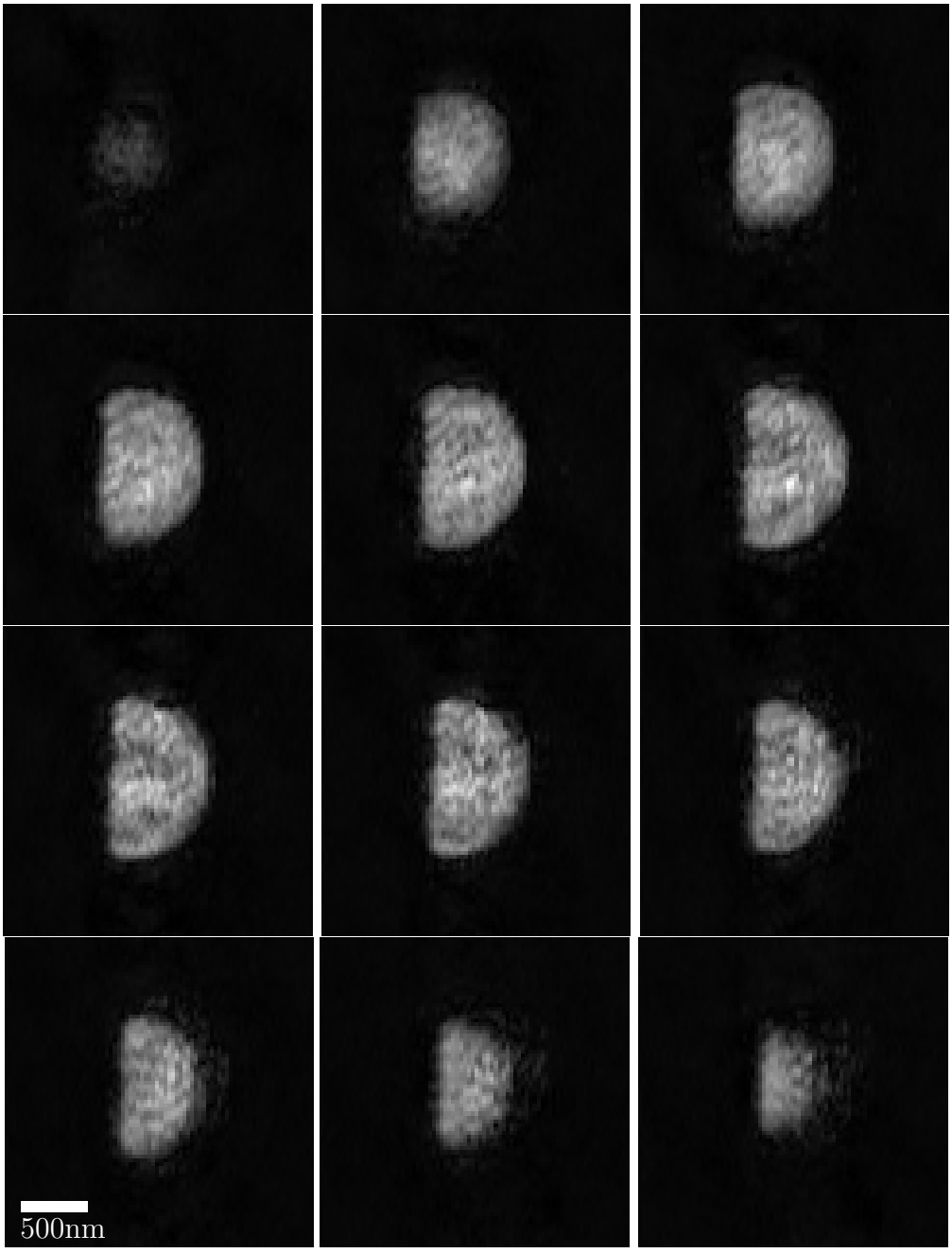

Figure 5.15: Density recovered from Pb1003-310, every third slice (86nm).

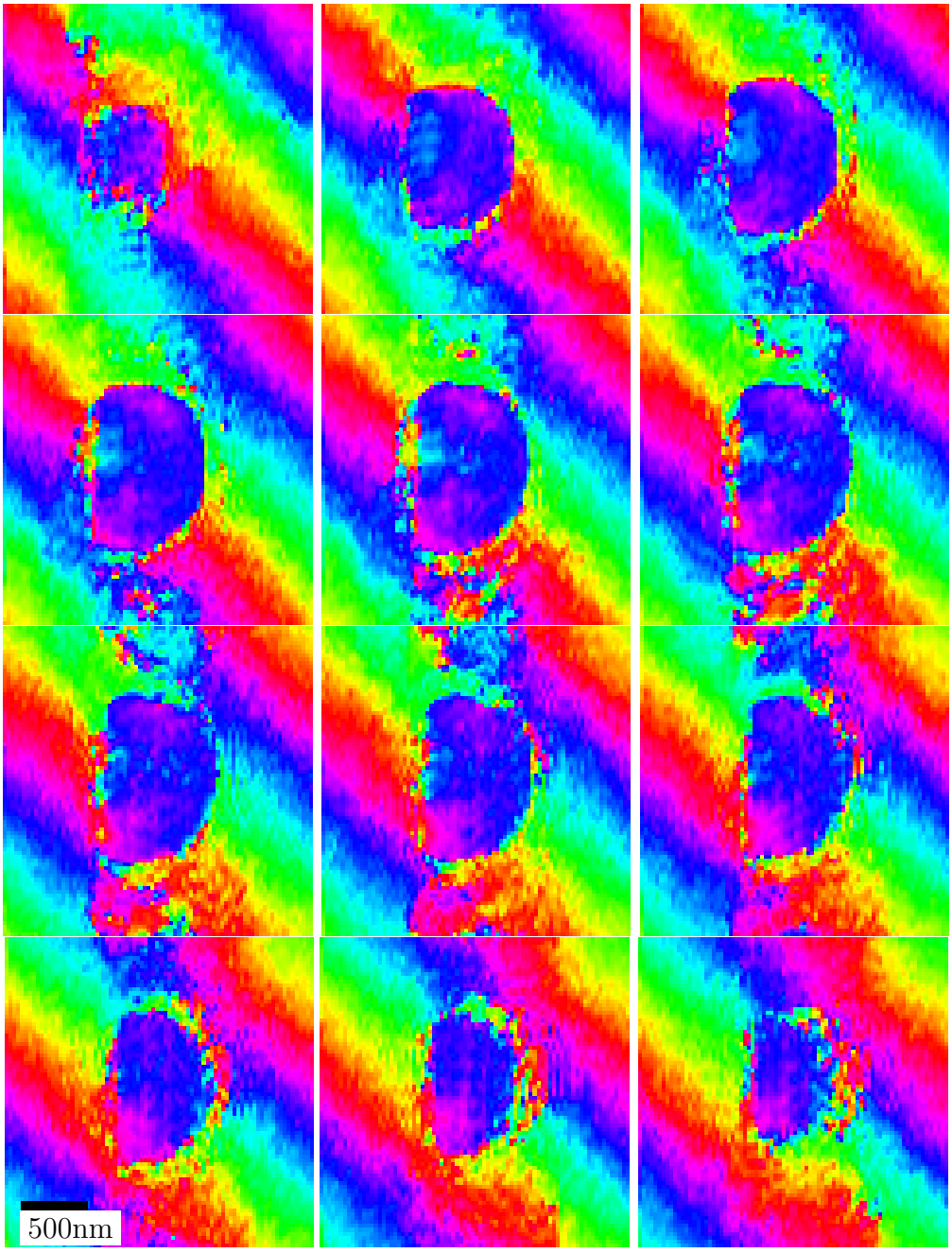

Figure 5.16: Phase recovered from Pb1003-310, every third slice (86nm).

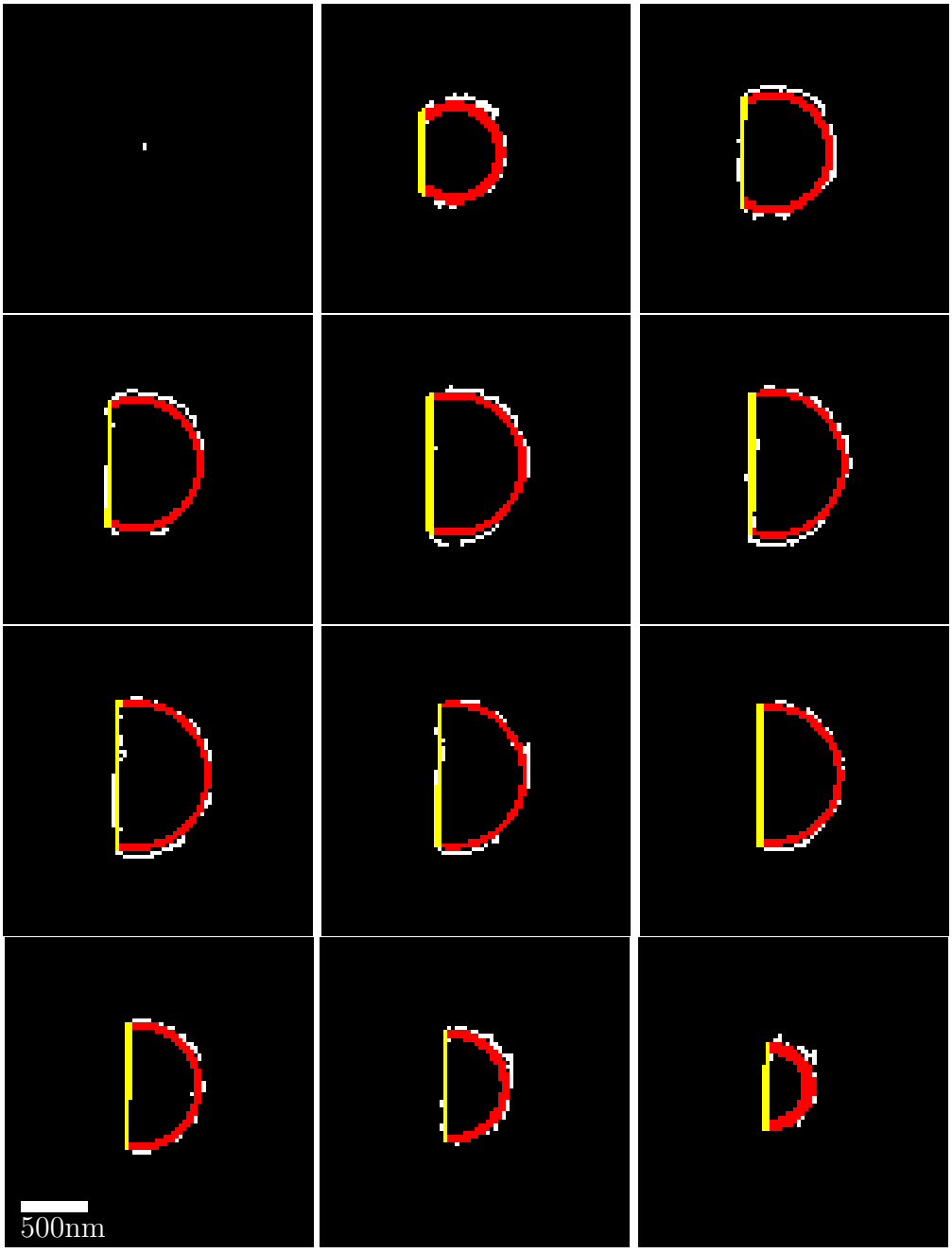

Figure 5.17: Shape fit to outline of density recovered from Pb1003-310, every third slice (86nm).

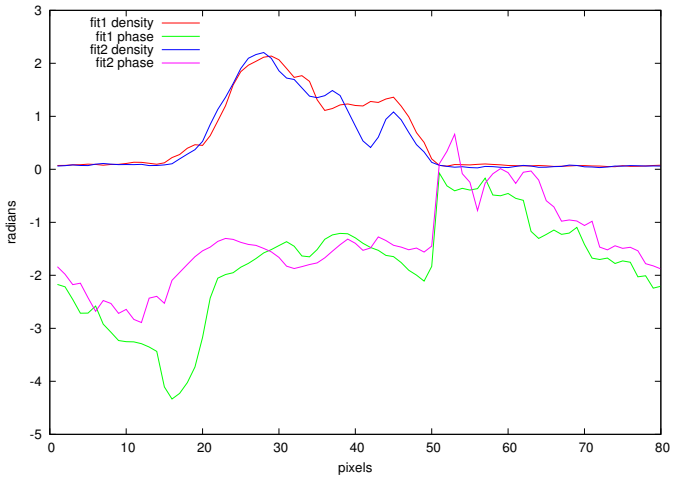

Figure 5.18: Density and phase along line in x direction across middle of best and second best fits to Pb1002-307.

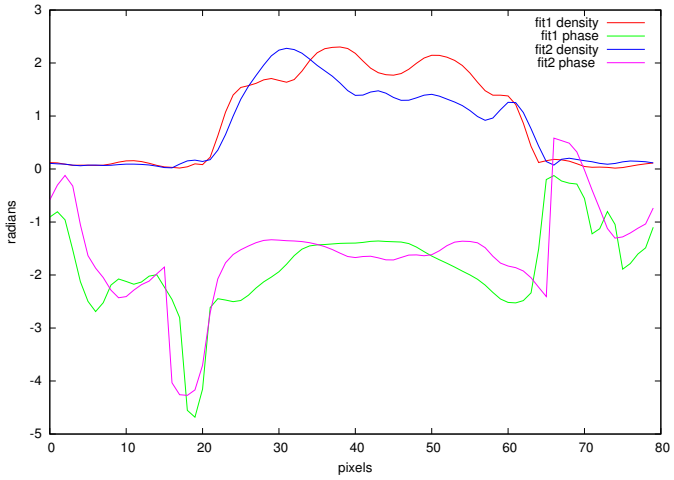

Figure 5.19: Density and phase along line in y direction across middle of best and second best fits to Pb1002-307.

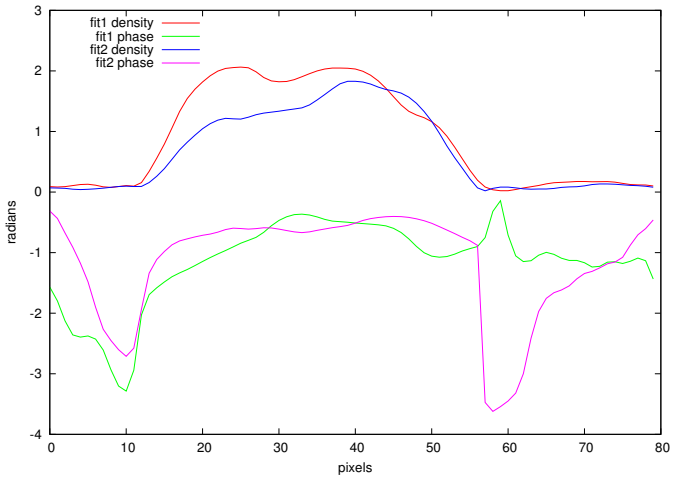

Figure 5.20: Density and phase along line in z direction across middle of best and second best fits to Pb1002-307.

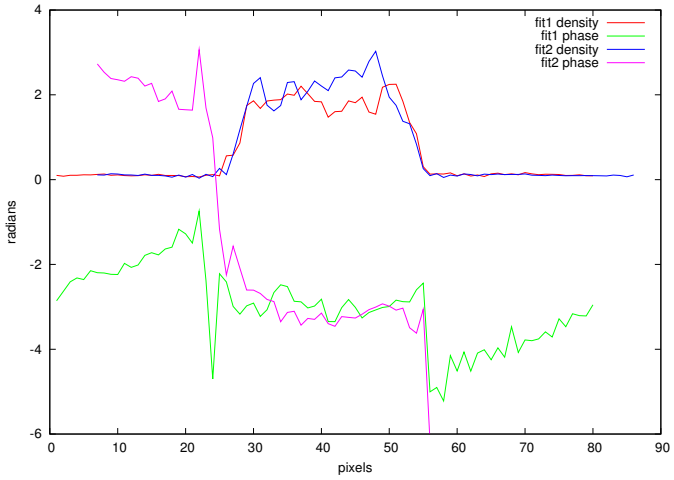

Figure 5.21: Density and phase along line in x direction across middle of best and second best fits to Pb1002-310.

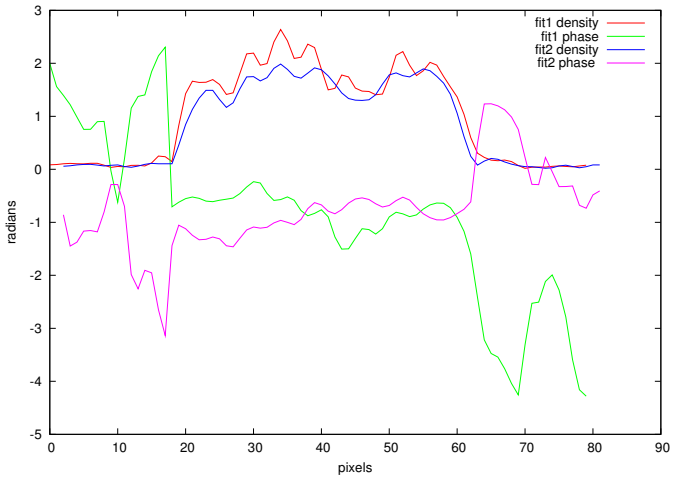

Figure 5.22: Density and phase along line in y direction across middle of best and second best fits to Pb1002-310.

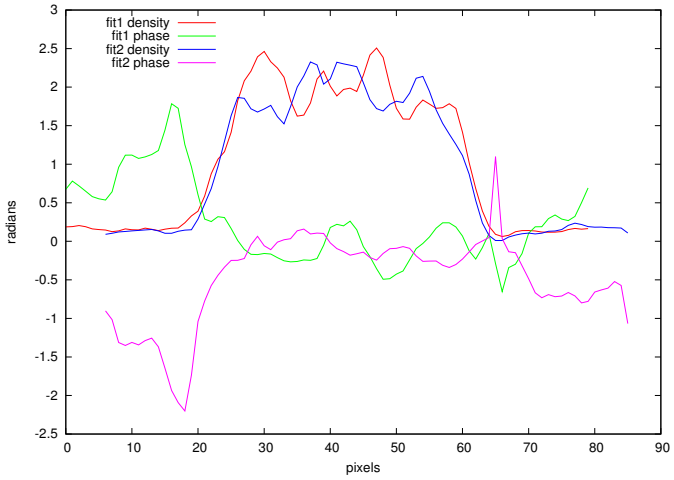

Figure 5.23: Density and phase along line in z direction across middle of best and second best fits to Pb1002-310.

Chapter 6

Conclusions

6.1 Summary

The diffraction from a finite crystal illuminated by a coherent beam of X-rays produces a diffraction pattern about each Bragg peak which includes information about the shape and stain of the diffracting crystal. I have successfully measured 3D coherent X-ray patterns for individual Pb particles within a few degrees of melting. By implementing the Fienup Hybrid Input-Output algorithm and a modified Error Reduction algorithm, I have recovered the phases of these oversampled diffraction patterns, simultaneously recovering the diffracting density of the crystal which produced the pattern. This diffracting density is a combination of the electron density and a phase factor which is the dot product of the strain and the scattering vector of the Bragg peak at which the pattern was measured.

After applying a geometric correction to account for the skewed coordinate system in which the peaks were measured, the densities all showed a spherical shape truncated by the substrate on which they were sitting. One especially high quality data set showed the substrate interface and five of eight possible {111} planes, plus one additional plane which may be related to a defect in the crystal. This additional plane is in the vicinity of a strong phase structure.

Two diffraction patterns from a single crystal were measured at different temperatures near the melting point. They showed a sizable change in the relative surface free energy of the vacuum and substrate interfaces of the crystal as the temperature was changed. Although temperature and spatial resolution were not great enough to measure surface melting, it was shown

how the technique of coherent X-ray diffraction is applicable to that problem.

Despite the failure to measure surface melting, this thesis presents the first density reconstructions from coherent X-ray diffraction patterns which are suitable for thermodynamic analysis. The reconstructions were achieved without any *a priori* knowledge of the crystal shape, yet yielded shapes consistent with a thermodynamic model.

6.2 Outlook

It is possible to calculate what improvements to the experiment would be necessary to allow surface melting to be measured. Consider the total intensity scattered from a series of samples of atomic number Z placed in an X-ray beam in an ideal experiment where the only source of noise is from counting statistics. In this ideal experiment the samples have identical shapes with large facets but different sizes. We assume a constant incident flux which may then be focused to concentrate the incident flux by a factor f. The number of atoms in the sample scales with the volume or radius cubed. Recalling the fact that the scattered intensity from a pair of parallel facets a unit distance apart will have the form $|\sin(q)/q|^2$, the total intensity measured in the n'th fringe over a time t in the diffraction pattern can be written as

$$I(n) \propto \frac{ftZ^2}{n^2 r^3}. \tag{6.1}$$

Synchrotron based measurements are often limited by the stability of the components to a finite measurement time, so t will be considered to be constant. This is especially true of organic or biological samples which are destroyed by the X-ray beam. For a series of samples of the same material Z is also constant.

The spacing in q between fringes scales with $1/r$, so the momentum transfer at fringe n can be written as $q(n) \propto n/r$. If fringe n_1 in the diffraction pattern from sample 1 contains the same intensity as fringe n_2 in the pattern

from sample 2,

$$\frac{f_1}{n_1^2 r_1^3} = \frac{f_2}{n_2^2 r_2^3} \tag{6.2}$$

$$\frac{n_2}{n_1} = \sqrt{\frac{f_2 r_1^3}{f_1 r_2^3}} \tag{6.3}$$

The resolution is therefore proportional to $1/q(n)$, or

$$\frac{\delta x_2}{\delta x_1} = \frac{q_1}{q_2} = \frac{r_1}{n_1} \times \frac{n_2}{r_1} = \frac{r_1}{r_2}\sqrt{\frac{f_2 r_1^3}{f_1 r_2^3}} = \sqrt{\frac{f_2 r_1^5}{f_1 r_2^5}}. \tag{6.4}$$

This calculation assumes that the intensity of an entire fringe can be measured simultaneously, or in the same number of measurements independent of the size of the object. The pattern exists is three dimensions, yet is typically measured with a two dimensional detector, with pixels in the $q_x - q_y$ plane. If measurements are made with the same resolution in q_z for particles of differing sizes, the intensity in Eqn. 6.1 is a less favorable

$$I(n) \propto \frac{ftZ^2}{n^2 r^4} \tag{6.5}$$

yielding a resolution

$$\frac{\delta x_2}{\delta x_1} = \frac{r_1^3}{r_2^3}\sqrt{\frac{f_2}{f_1}}. \tag{6.6}$$

This discrepancy can be removed if the monochromator could be continually varied to pass more flux with a shorter coherence length when smaller samples are being studied. Irregardless, smaller samples will produce weaker diffraction patterns yielding worse real space resolution. This problem is significantly magnified if sources of noise other than counting statistics are present. Since the diffraction pattern from a smaller crystal is more diffuse, more noise will be measured during measurement of the diffraction pattern.

Focusing appears to be the best method for improving resolution for particles significantly smaller than the coherence length of the beam. In 10 hours the diffraction pattern from a 748nm Pb particle can be measured at Sector 34 of the APS without focusing with sufficient statistics that its shape can be recovered with 27nm resolution. K-B mirrors can currently focus an X-ray beam by up to 300 times in each direction. At present mirrors can not

be used in vacuum at Sector 34, but this capability could be added. Using 100 times vertical focusing and 6 times horizontal focusing, the diffraction pattern from the same particle should be measured with sufficient statistics at high enough q to yield a resolution of $27\text{nm}/\sqrt{600}=1.1\text{nm}$, sufficient to image surface melting of a Pb particle within a degree of melting.

Coherent X-ray diffraction has the potential to be of use in a wide variety of systems which are of practical importance. Because of the penetrating power of X-rays, it can be used to image buried structures. One such example would be looking at individual grains in the a polycrystalline bulk material. Coherent X-ray diffraction could be used to map out the localized strain in individual grains microns below the surface of a structural material, lending new insight into how the strain within nanometers of grain boundaries affects bulk properties. Coherent X-ray diffraction could be even more useful in new composite materials, such as Cu reinforced with alumina filaments. If the illumination on the sample can be held stationary while moving from a Cu diffraction peak to an alumina peak, both the strain within an individual fiber and in the surrounding copper could be imaged. Coherent X-ray diffraction could also be used to image the strain in caused by electromigration, a major cause of failure in sub-micron circuits, even in complex layered circuits.

The future of coherent X-ray diffraction may be in the combination of phasing algorithms with other techniques, such as use of holography to find a low resolution image of the diffracting object to be used as either the starting point for phasing or as a very tight support for the fit, or maximum entropy methods, combining knowledge about the probability of specific real space density occurring with intensity measurements in an iterative algorithm.

References

[1] http://www.aps.anl.gov/techbulletins/TB26/TB26.html.

[2] http://www.roperscientific.de.

[3] http://www.aps.anl.gov/epics.

[4] http://www.gimp.org.

[5] http://vis5d.sourceforge.net.

[6] http://www.gnuplot.info.

[7] Jens Als-Nielsen and Des McMorrow. *Elements of Modern X-ray Physics*. John Wiley & Sons, Ltd., 2001.

[8] Altman. Evidence of a Pb (100) (2×2) reconstruction. *Surface Science*, 314:65–69, 1995.

[9] N.W. Ashcroft and N.D. Mermin. *Solid State Physics*. Saunders Colloge Publishing, 1976.

[10] R. Barakat and G. Newsam. Necessary conditions fro a unique solution to two-dimensional phase recovery. *Journal of Mathematical Physics*, 25(11):3190–3193, 1984.

[11] R.H.T. Bates. Fourier phase problems are uniquely solvable in more than one dimension. *Optik*, 61(3):247–262, 1981.

[12] H.P. Bonzel and A. Edmunds. Absolute values of surface and step free energies from equilibrium crystal shapes. *Physical Review Letters*, 84(25):5804–5807, 2000.

[13] S. Chen, K. Huang, and J.A. Stearns. Alkanethiolate-protected palladium nanoparticles. *Chemistry of Materials*, 12(2):54, 2000.

[14] P.R. Couchman. The Lindmann hypothesis and the size-dependence of melting temperature. *Philosophical Magazine A*, 40(5):634–643, 1979.

[15] P. Curie. *Bull. Soc. min de France*, 8:145, 1885.

[16] Francesco D. Di Tolla, Furio Ercolessi, and Erio Tosatti. Maximum overheating and partial wetting of nonmelting solid surfaces. *Physical Review Letters*, 74(16):3201–3204, 1995.

[17] J.W. Edington. *Practical Electron Microscopy in Materials Science*. Van Nostrand Reinhold Company, 1976.

[18] S. Eisebitt, M. Lörgen, W. Eberhardt, J. Lüning, S. Andrews, and J. Stöhr. Scalable approach for lensless imaging at x-ray wavelengths. *Applied Physics Letters*, 84(17):3373–3375, 2004.

[19] Veit Elser. Phase retrieval by iterative projections. *Journal of the Optical Society of America*, 20:40–55, 2003.

[20] Thomas Engel. Experimental aspects of surface roughening. In R. Vanselow and R. Howe, editors, *Chemistry and Physics of Solid Surfaces VII*. Springer Verlag, 1988.

[21] J.R. Fienup. Phase retrieval algorithms, a comparison. *Applied Optics*, 21(15):2758–2769, 1982.

[22] R.M. Flemming, 1995. copyright AT &T Bell Laboratories, now maintained independently.

[23] Joost W.M. Frenken and J.F. van der Veen. Observation of surface melting. *Physical Review Letters*, 54(2):134–174, 1985.

[24] R.W. Gerchberg and W.O. Saxton. Phase determination from image and diffraction plan pictures in the electron microscope. *Optik*, 34:277–286, 1971.

[25] R.W. Gerchberg and W.O. Saxton. A practical algorithm for the determination of phase from image and diffraction plan pictures. *Optik*, 35:237–246, 1972.

[26] H. He, S. Marchesini, M. Howells, U. Weierstall, H. Chapman, S. Hau-Riege, A. Noy, and J.C.H. Spence. Inversion of x-ray diffuse scattering to images using prepared objects. *Physical Review B*, 67:174114–1/3, 2003.

[27] C. Herring. Some theorems on the free energies of crystal surfaces. *Physical Review*, 82(1):87–93, 1951.

[28] C. Herring. In R. Gomer and CS. Smith, editors, *Structure and Properties of Solid Surfaces*. University of Chicago Press, 1953.

[29] J.C. Heyraud and J.J. Métois. Equilibrium shape of gold crystallites on a graphite cleaved surface: surface energies and interfacial energy. *Acta Metallurgica*, 28:1789–1797, 1980.

[30] J.C. Heyraud and J.J. Métois. Establishment of the equilibrium shape of metal crystallites on a foreign substrate: gold on graphite. *Journal of Crystal Growth*, 50:571–574, 1980.

[31] J.C. Heyraud and J.J. Métois. Equilibrium shape and temperature: lead on graphite. *Surface Science*, 128:334–342, 1983.

[32] J.C. Heyraud, J.J. Métois, and J.M. Bermond. Surface melting and equilibrium shapes. *Journal of Crystal Growth*, 98(3):355–362, 1998.

[33] H. Hilton. *Mathematical Crystallography*. Oxford University Press, 1903.

[34] C. Jayaprakash and W.F. Saam. Thermal evolution of crystal shapes: the fcc crystal. *Physical Review B*, 30(7):3916–3928, 1984.

[35] M. Kawasaki, T. Toshioka, and M. Shiojiri. New specimen preparation methods for materials transmission electron microscopy using ion-milling. *Electron Technology*, 31(2):183–188, 1998.

[36] Charles Kittel and Herbert Kroemer. *Thermal Physics*. W.H. Freeman and Company, 1980.

[37] E. Kovalyov, E. Resnyanskii, V. Elokhin, B. Bal'zhinimaev, and A. Myshlyavtsev. Novel statistical lattice model for the supported nanoparticle. *Physical Chemistry and Chemical Physics*, 5(4):784–790, 2003.

[38] K. Kuchařová, S.J. Zhu, and J. Čadek. Creep in ODS copper reinforced with alumina short fibres-DRS copper. *Materials Science and Engineering*, A355:267–276, 2003.

[39] H. Liebman. *Zeitschrif für Kristallographie*, 53:171, 1914.

[40] F. Livet, F. Bley, J. Mainville, R. Caudron, S.G.J. Mochrie, E. Geissler, G. Dolino, D. Abernathy, G. Grübel, and M. Sutton. Using direct illumination CCDs as high-resolution area detectors for X-ray scattering. *Nuclear Instruments and Methods in Physics Research A*, 451:596–609, 2000.

[41] J. Margrave, editor. *The Characterization of High Temperature Vapors*. John Wiley & Sons, 1967.

[42] J. Miao, T. Ishikawa, B. Johnson, E. Anderson, B. Lai, and K. Hodgson. High resolution 3D X-ray diffraction microscopy. *Physical Review Letters*, 89(8):088303–1–4, 2002.

[43] R.P. Millane and W.D. Stroud. Reconstructing symmetric images from their undersampled fourier intensities. *Journal of the Optical Society of America*, 4(14):568–579, 1997.

[44] P. Noziéres. Surface melting and crystal shape. *Journal de Physique*, 50:2541–2550, 1989.

[45] A. Pavlovska, D. Dobrev, and E. Bauer. Orientation dependence of the quasi-liquid layer on tin. *surface Science*, 314(3):341–352, 1994.

[46] R.M. Pilliar and J. Nutting. Solid-solid interfacial energy determination in metal-ceramic systems. *Philosophical Magazine*, 16:181, 1967.

[47] B. Pluis, A.W. Denier van der Gon, J.W. M. Frenken, and J.F. van der Veen. Crystal-face dependence of surface melting. *Physical Review Letters*, 59(23):2678–2681, 1987.

[48] I.K. Robinson, J.L. Libbert, I.A. Vartanyants, J.A. Pitney, D.M. Smilgies, D.L. Abernathy, and G. Grübel. Coherent x-ray diffraction imaging of silicon oxide growth. *Physical Review B*, 60(14):9965–9972, 1999.

[49] I.K. Robinson, I.A. Vartanyants, G.J. Williams, M.A. Pfeifer, and J.A. Pitney. Reconstruction of gold nanocrystals using coherent x-ray diffraction. *Physical Review Letters*, 87(19):195505–1/4, 2001.

[50] Andreas Rosenauer. *Transmission Electron Microscopy of Semiconductor Nanostructures*. Springer-Verlag, 2003.

[51] Craig Rottman and Michael Wortis. Exact equilibrium crystal shapes at nonzero temperature in two dimensions. *Physical Review B*, 24(11):6274, 1981.

[52] D. K. Saldin, R. Harder, H. Vogler, W. Moritz, and I.K. Robinson. Solving the structure completion problem in surface crystallography. *Computer Physics Communications*, 137:12–34, 2001.

[53] D. Sayre. Some implications of a theorem due to Shannon. *Acta Crystallographica*, 5:843, 1952.

[54] John Stewart. Step melting and the equilibrium crystal shape of Pb. *Physical Review Letters*, 71(6):887–890, 1993.

[55] John Stewart. Step melting on the Pb (111) surface. *Physical Review B*, 49(19):13826–13837, 1994.

[56] B.E. Sundquist. A direct determination of the anisotropy of the surface free energy of solid gold, silver, copper, nickel and alpha and gamma iron. *Acta Metallurgica*, 12(1):67–86, 1964.

[57] M.M. Telkar, C.V. Rode, R.V. Chaudhari, S.S. Joshi, and A.M. Nalawade. Shape controlled preparation and catalytic activity of metal nanoparticles for hydrogenation of 2-butyne-1,4-diol and styrene oxide. *Applied Catalysis A: General*, 273(1-2):11–19, 2004.

[58] J.F. van der Veen, B. Pluis, and A.W. Denier van der Gon. Surface melting. In R. Vanselow and R. Howe, editors, *Chemistry and Physics of Solid Surfaces VII*. Springer Verlag, 1988.

[59] I.A. Vartanyants, J.A. Pitney, J.L. Libbert, and I.K. Robinson. Reconstruction of surface morphology from coherent x-ray reflectivity. *Physical Review B*, 55(19):13193–13202, 1997.

[60] M. von Laue. *Zeitschrif für Kristallographie*, 105:124, 1923.

[61] S.C. Wang and Gert Ehrlich. Adatom motion to lattice steps: a direct view. *Physical Review Letters*, 70(1):41–44, 1993.

[62] B.E. Warren. *X-ray Diffraction*. Dover Publications, Inc., 1990.

[63] Garth J. Williams. *Microscopy of Gold Microcrystals by Coherent X-ray Diffractive Imaging*. PhD thesis, University of Illinois at Urbana-Champaign, 2004.

[64] G.J. Williams, M.A. Pfeifer, I.A. Vartanyants, and I.K. Robinson. Three-dimensional imaging of microstructure in Au nanoparticles. *Physical Review Letters*, 90(17):175505–1/4, 2003.

[65] W.L. Winterbottom. Equilibrium shape of small particles in contact with a foreign substrate. *Acta Metallurgica*, 15(2):303–310, 1967.

[66] Michael Wortis. Equilibrium crystal shapes and interfacial phase transitions. In R. Vanselow and R. Howe, editors, *Chemistry and Physics of Solid Surfaces VII*. Springer Verlag, 1988.

[67] G. Wulff. *Zeitschrif für Kristallographie*, 34:449, 1901.

[68] X. Yu and P.M. Duxbury. Kinetics of nonequilibrium shape change in gold clusters. *Physical Review B*, 52(3):2102–2106, 1995.

Author's Biography

Mark Pfeifer was born on December 3, 1975 in Camp Hill, Pennsylvania to August and Carolyn Pfeifer. His interests in science, music, and the outdoors were shared by his brothers and sister. He attended Good Shepherd Grade School and Trinity High School in Camp Hill, during which time he was active in Boy Scouts and in various choirs, in addition to playing the piano. He attended the University of Notre Dame, graduating with a Bachelor of Science degree in 1998. When he wasn't studying, Mark was singing or traipsing about the world with the Notre Dame Glee Club. He also had the opportunity to conduct research under the guidance of Peter Schiffer. Between receipt of his bachelors degree and starting graduate school at the University of Illinois at Urbana-Champaign Mark married Alexandra Norris in South Bend, Indiana. They have a two year old son, Patrick, who acts like he might want to be scientist too. At the University of Illinois, Mark has taught introductory physics as a teaching assistant and has conducted research under the guidance of Ian Robinson. Mark received his Master of Science degree from the University of Illinois in 2000.